



**HAL**  
open science

# Properties of graphene by chemical recognition on Surface Acoustic Wave (SAW) sensors: Application to the detection of chemical compounds in the gaseous state

Ioannis Nikolaou

► **To cite this version:**

Ioannis Nikolaou. Properties of graphene by chemical recognition on Surface Acoustic Wave (SAW) sensors: Application to the detection of chemical compounds in the gaseous state. Electronics. Université de Bordeaux, 2019. English. NNT : 2019BORD0379 . tel-02930977

**HAL Id: tel-02930977**

**<https://theses.hal.science/tel-02930977>**

Submitted on 4 Sep 2020

**HAL** is a multi-disciplinary open access archive for the deposit and dissemination of scientific research documents, whether they are published or not. The documents may come from teaching and research institutions in France or abroad, or from public or private research centers.

L'archive ouverte pluridisciplinaire **HAL**, est destinée au dépôt et à la diffusion de documents scientifiques de niveau recherche, publiés ou non, émanant des établissements d'enseignement et de recherche français ou étrangers, des laboratoires publics ou privés.

# THÈSE

présentée à

**L'UNIVERSITÉ BORDEAUX**

ÉCOLE DOCTORALE DES SCIENCES PHYSIQUES ET DE L'INGÉNIEUR

par

**Ioannis Nikolaou**

POUR OBTENIR LE GRADE DE

**DOCTEUR**

SPÉCIALITÉ : ÉLECTRONIQUE

---

*Étude des propriétés de reconnaissance chimique du graphène par ondes acoustiques de surface : Application à la détection de composés chimiques à l'état gazeux*

---

Soutenue le 17 décembre 2019

Devant la commission d'examen formée de:

**Dr. Anne-Claire SALAÜN**, Maître de conférences HDR, Université de Rennes, France

Rapporteur

**Prof. Philippe MENINI**, Professeur des universités, Université de Toulouse, France

Rapporteur

**Dr. Maria Carmen HORRILLO GÜEMES**, Investigador Científico, CSIC, Madrid, Espagne

Examinatrice

**Prof. Corinne DEJOURS**, Professeur des universités, Bordeaux INP, France

Présidente

**Dr. Ollivier TAMARIN**, Maître de conférences, Université de Guyane, France

Invité

**Dr. Hamida HALLIL**, Maître de conférences, Université de Bordeaux, France

Co-directrice de thèse

**Prof. Dominique REBIÈRE**, Professeur des universités, Université de Bordeaux, France

Directeur de thèse



# THESIS

submitted to the

**UNIVERSITY OF BORDEAUX**

DOCTORAL SCHOOL OF PHYSICAL SCIENCES AND ENGINEERING

by

**Ioannis Nikolaou**

in partial fulfillment for the Degree of

**DOCTOR OF PHILOSOPHY**

in ELECTRONICS

---

*Properties of graphene by chemical recognition on Surface  
Acoustic Wave (SAW) sensors: Application to the detection of  
chemical compounds in the gaseous state*

---

Defense date: 17 December 2019

Review committee:

**Prof. Anne-Claire SALAÜN**, Assoc. Prof., University of Rennes, France

Reviewer

**Prof. Philippe MENINI**, Full Professor, University of Toulouse – Paul Sabatier, France

Reviewer

**Dr. Maria Carmen HORRILLO GÜEMES**, Full Researcher, CSIC, Madrid, Spain

Examiner

**Prof. Corinne DEJOUS**, Full Professor, Bordeaux INP, France

President

**Dr. Ollivier TAMARIN**, Assoc. Prof., University of French Guiana, France

Invited

**Dr. Hamida HALLIL**, Assoc. Prof., University of Bordeaux, France

Thesis Co-Director

**Prof. Dominique REBIÈRE**, Full Professor, University of Bordeaux, France

Thesis Director



*In the name of the best within you, do not sacrifice this world to those who are its worst. In the name of the values that keep you alive, do not let your vision of man be distorted by the ugly, the cowardly, the mindless in those who have never achieved his title. Do not lose your knowledge that man's proper estate is an upright posture, an intransigent mind and a step that travels unlimited roads. Do not let your fire go out, spark by irreplaceable spark, in the hopeless swamps of the approximate, the not-quite, the not-yet, the not-at-all. Do not let the hero in your soul perish, in lonely frustration for the life you deserved, but have never been able to reach. Check your road and the nature of your battle. The world you desired can be won, it exists, it is real, it is possible, it's yours.*

*Ayn Rand*



*To my family*





## Acknowledgments

« Once, I was asked, how do I see myself in the future and how do I want other people to look at me. My answer to that was that I want to actually inspire the change in people; motivate them towards their best self. Following a career in academia it might not be an easy task but it would end up putting me in a position that I could actually set and realize severe goal orientations. To my perspective, in order to be able to inspire other people you have to be able to feel inspired within yourself, which usually comes by thinking of the long-term outcomes. Generally, task orientations are regarded as more adaptive than ego orientations. Task orientation is a value that every scientific goal can be related to, especially when it comes to selection of challenging tasks, effective study strategies, positive attitudes toward learning, and positive emotions, whereas quite often ego orientation is associated with selection of easier tasks, trivial learning strategies, concern for social status and thoughts of escape and behavioral withdrawal when difficulties are encountered. My ‘unquenchable fire’ for knowledge is inextricably linked with an insatiable curiosity about science and actually helps viewing an academic/research achievement, such as a Ph.D. with more fun. Thus, following my only true passion for Physics and Engineering, I started a Ph.D. in Bordeaux at October of 2013. I would like to acknowledge Prof. Dominique Rebière and Associate Prof. Hamida Hallil at IMS laboratory (CNRS UMR 5218) for giving me the opportunity to work with such an interesting and promising subject; that of graphene-based novel microsystems. Throughout the thesis I had the rare chance to approach the field of surface acoustic wave sensors from various different aspects, which was extremely fruitful for acquiring a more solid understanding, especially from the theoretical and experimental perspectives. Furthermore, I would like to thank Prof. Corinne Dejous, for the countless scientific discussions that we had over time, especially on the properties of the Love wave devices. Without her detail-oriented advices and solid scientific expertise, this thesis would not come to exist. Our discussions didn’t only help me evolve as a scientist, but also as an individual, and I am grateful for that. I was truly honored to work with her. Of course, at this point it would be a crime if I wouldn’t acknowledge Dr. George Deligeorgis. The discussions that we had during my thesis were crucial to solidify the results presented herein. Thanks to him, I also had the rare opportunity to prove several concepts regarding the carbon-based materials between different laboratories (France, Spain and Greece), since he initiated the collaboration with a famous and well-known laboratory in Spain (Instituto Universitario de Tecnología Química, Universidad Politécnica de Valencia (CSIC-UPV). During his staying in France (Toulouse / LAAS - CNRS), he managed to provide guidance on my research, thus highlighting how important is the repeatability in the research community, especially after our first-year results. Furthermore, he initiated a novel collaboration with FORTH–IESL, Microelectronics Research Group in Greece, due to his establishment as a researcher. His rigorous corrections on the material-based premises (graphene) and his enormous experience on the process development concepts (deposition aspects of carbon-based materials) were important lessons for me and my future as a researcher. Additionally, I would like to thank also Prof. Hermenegildo Garcia with whom Dr. George Deligeorgis and Acoustic wave based and innovative Detection Microsystems (Microsystèmes de Détection à ondes Acoustiques et alternatives - MDA) group had collaborated for the initial graphene coated Love wave devices. With his knowledge and expertise on chemical based composites, this research couldn’t go further, since he provided enough evidence to understand the preparation, characterization and morphology of the graphene based solutions under different oxidation levels. Evidently, he has opened the horizon to further control of material parameters

to tailor the properties of the second generation of graphene-based Love wave devices. Furthermore, I would like to acknowledge Ms. Veronique Conédéra from Laboratory for Analysis and Architecture of Systems (LAAS - CNRS) for providing high quality Love wave devices. We were working together since day 1 of my thesis and she was the one that firstly introduced me to the world of Drop on demand (DoD) inkjet-printing process electronics; a fact that I am grateful of. For the realization of this thesis I had the chance to collaborate with other laboratories too, within the University of Bordeaux. I would like to acknowledge Associate Prof. Sebastien Bonhommeau and Mr. David Talaga, from the University of Bordeaux – Institute of Molecular Sciences (Institut des Sciences Moléculaires - ISM) for the numerous Raman and Atomic Force Microscopy (AFM) experiments, especially on the highly oxidized graphene Love wave devices. The research conducted on ISM laboratory, was crucial, since it shed light on the electro-mechanical properties of the graphene oxide nano-sheets. Associate Prof. Sebastien Bonhommeau and Mr. David Talaga have provided exceptional experimental premises in a very short amount of time, that is to say, without their scientific contribution and responsiveness, the Physica Status Solidi (PSS) publication would not have been realized. From the University of Bordeaux, I would like to thank the theoretician from the MDA group, Dr. Ollivier Tamarin, for the countless discussions on the acoustic wave theory and mechanisms, analyzing and understanding deeply some crucial elasto-viscosity effects, especially when those are mixed with carbon allotropes / porous materials. It is worth noting, that Dr. Ollivier Tamarin has equally contributed on any scientific research that we published together, besides the fact that we had a limited amount of time to produce, understand and validate the theoretical aspects regarding the analytical modelling of the graphene - coated Love wave devices. Our collaboration has been established during my 3rd year of the Ph.D. and without his rigorous corrections on the manuscript, this thesis would not be fully realized. I was truly honored to work with such a talented scientist. Finally, I would like to thank Jean-Luc Lachaud for assisting in setting up the Vector Network Analyzer (VNA) and installing the permeation tubes in the gas-line characterization room. Further, due to his novel and efficient calibration design kits, as well as his counter-intuitive problem-solving mindset, we were able to collaborate and solve any cell-engineering difficulties and electrical characterization problems. I was happy to work with a person that acquires a MacGyver's skillset. Last but not least, it would be unfair to forget the significance of Dr. Damien Thuau due to his excellent scientific assistant on the optical interference profiling measurements regarding the thickness of the coated graphene films on the Love wave devices. The presentation of the aforementioned results was realized on IEEE sensors conference in Korea (November of 2015). At that chronological point, his contribution was really essential, since I was attending a five-day conference with a highly research impact within the scientific community of sensory devices. I would like to acknowledge also Dr. Vincent Raimbault, a National Center for Scientific Research (CNRS) fellow, for his numerous scientific discussions and experimental contributions, as well as for his philosophical oriented approaches about science and research life. It would be a shame to forget his impact on this Ph.D., since through his discussions, knowledge and experience, it was later implemented (at the end of my 1st year) a commercial humidity sensor on the gas-line characterization room in order to compare our devices and their efficiency. It might not seem trivial but under his guidance I was able to program the Arduino devices for the humidity sensing, as well as to acquire efficient and fast coding skills regarding the electrical characterization of the Love wave devices. Further, I was truly lucky to have the chance to work with such a distinguished and well-oriented research scientist, since his contributions are highly observable through the outcome of my early published research based on useful measurements regarding the humidity detections. I would like to acknowledge also Ms. Valérie Abel and all the secretaries of the group MDA and IMS,

respectively. Especially, I am really grateful to all of them for all their assistance in administrative stuff during all these years that I spent working in the lab.

During my time in Bordeaux, I took invaluable life lessons - both on a scientific and a personal level. By observing my bosses, not only I learnt how to manage several situations inside a work environment, but I also observed how to actually guide, lead and motivate people; a lesson that would be important in the future of my career. However, those weren't the most important things that I was taught. Through my various experiences inside the lab-life I learnt a really essential lesson; as long as you know where you stand, not only it doesn't matter what people think or say about you, but also that there is nothing and no-one to be afraid of. Associate Prof. Hamida Hallil taught me this lesson personally, and I am grateful to her for that, as true self-confidence is a crucial trait both for a scientist or a leader, in a laboratory or a company, respectively. And usually, this kind of 'self-knowledge' doesn't come easy.

Finally, I would like to thank all my friends, multinational and Greek, inside and outside IMS-laboratory. If I had to name each and every one of you, I would have to write another thesis. I would like to thank all of you, personally, for sharing and having precious time together. Being in a university that gathers people from various nationalities, I was lucky to forge friendships with people from all the edges of the world. And with this, I realized that it is important to draw wisdom from many places. If we take it from only one place, it becomes rigid and stale. But, interacting and understanding the other cultures can help you become whole as a person.

I would like to thank one more time everyone within the faculty for their understanding and for providing me this opportunity.

And, last but not least, according to Niels Bohr 'an expert is a man who has made all the mistakes which can be made, in a narrow field'; overcoming plenty of difficulties during my Ph.D. in a French educational system forged my personal development for the benefit of all. Also, the presence and support of my friends and family made this experience extremely and truly wonderful. During the period of my thesis I had faced family and personal issues, so it wasn't an easy time, neither for me in Bordeaux, nor for my family in Greece. Thus, I dedicate this thesis to my family. And of course, I would like to thank them for their non-stop support all these years.

Stay hungry, stay foolish  
Merci beaucoup pour tout,

Ioannis »

# Table of Contents

## Contents

<b>Contents</b> .....	xii
Chapter 1 Introduction and Organization of the dissertation .....	xiv
I. Introduction .....	1
I.1 Foreword .....	1
I.1.1 Motivation - Thesis work summary .....	1
I.1.2 Significance of this work .....	2
I.1.3 Organization of the dissertation .....	3
I.2 Literature review – Materials and SAW devices for gas sensing applications .....	5
I.2.1 Introduction - Gas/Vapor sensing applications .....	5
I.2.2 SAW chemical sensors .....	6
I.2.3 Acoustic wave families .....	7
I.2.4 Sensing materials for SAW devices and vapor detections .....	14
I.3 Conclusion .....	23
References or Bibliography (if any) .....	25
Chapter 2 Sensors and Materials Integration .....	34
II. Graphene Oxide sensing material integration in the acoustical platform .....	35
II.1 Introduction .....	35
II.2 Love wave platform fabrication .....	35
II.3 Preparation of graphene oxide solution and its Drop-Casting deposition .....	37
II.3.1 Graphene Oxide solution preparation and its characterization .....	37
II.3.2 Drop - Casting technique for GO deposition .....	39
II.4 Preparation of GO based materials and Inkjet-Printing deposition technique .....	45
II.4.1 Graphene Oxide solution preparation and its characterization .....	45
II.4.2 Inkjet-Printing integration of Graphene Oxide thin films .....	47
II.4.3 Inkjet-Printing characterization of Graphene Oxide thin films .....	49
II.4.4 Electrical characterization of the Inkjet-Printed G-O thin films .....	52
References or Bibliography (if any) .....	56
Chapter 3 Sensor simulation .....	59
III. Theoretical studies .....	60
III.1 Introduction .....	60
III.2 Modeling of the Love wave sensor .....	60
III.3 Analytical simulation modeling .....	63
III.4 Numerical (FEM) modeling .....	65
III.5 Results and discussion: Application to the numerical and analytical simulations .....	71
References or Bibliography (if any) .....	77
Chapter 4 Vapor detection tests .....	79
IV. Characterization of the GO - Love wave devices under different vapor .....	80
IV.1 Introduction .....	80
IV.2 Gas line experimental setup .....	81
IV.3 Drop – Casted GO sensor performances .....	82
IV.3.1 Detection of humidity .....	82
IV.3.2 Detection of chemical compounds in a gaseous state .....	86
IV.4 Inkjet – Printed GO sensor performances .....	89
IV.4.1 Detection of Ethanol and Toluene Vapors in real time .....	89
IV.4.2 Specificity to NH <sub>3</sub> and NO <sub>2</sub> detections .....	94

IV.4.3	Detection of humidity .....	97
	References or Bibliography (if any) .....	101
	Chapter 5 Conclusions and Prospects .....	104
V.	The Good, the Bad and the Missing .....	105
V.1	Introduction.....	105
V.2	The Good .....	105
V.3	The Bad and the Missing .....	107
V.4	Finally... ..	108
VI.	Appendices (if any).....	109
VI.1	Author's contributions .....	109
VI.2	Appendix A - Chapter I: Classification of acoustic wave devices and gas sensing mechanisms.....	110
VI.2.1	A.1 – Classification of acoustic wave devices.....	110
VI.3	Appendix B - Chapter II: .....	112
VI.3.1	B.1 Post-fabrication procedures.....	112
VI.3.2	B.2 – Electrical measurement procedures & Calculations.....	113
VI.4	Appendix C - Chapter III: .....	119
VI.4.1	C.1 Maple analytical equations & calculations: .....	119
VI.4.2	C.2 Numerical calculations – Comsol formulas: .....	122
VI.5	Appendix D - Chapter IV: Gas line experimental conditions and further investigation of the graphene based sensitive material.....	123
VI.5.1	D.1 Vaporizer PUL110 (ppm) and PUL010 (ppb) conditions.....	123
VI.5.2	D.2 Further investigation of the graphene based sensitive material .....	127
	References or Bibliography (if any) .....	131

# Chapter 1

## Introduction and Organization of the dissertation

# I. Introduction

## I.1 Foreword

The past several decades have witnessed a tremendous development of chemical sensors in many fields. Detecting gases and toxic vapors with early warning feature are playing increasingly important roles in many fields, including environmental protection, industrial manufacture, medical diagnosis, and national defense. Meanwhile, sensing materials are of intense significance in promoting the combination properties of gas/vapor sensors, such as sensitivity, selectivity, and stability. Thus, various materials, covering from inorganic semiconductors, metal oxides, and solid electrolytes, to conducting polymers, have been exploited to assemble sensing devices with small sizes, low power consumption, high sensitivity, and long reliability. Among them, nanostructured materials, such as graphene, carbon nanotubes (CNTs), and metal-oxide nanoparticles, are widely used in gas sensing for their excellent responsive characteristics, mature preparation technology, and low cost of mass production, since the traditional metal-oxide technologies are running into enormous challenges as they reach the physical limits of existing silicon-based semiconducting technology. As one of the fascinating materials, graphene has aroused scientists' great enthusiasms in its synthesis, modification, and applications in many fields since 2004, due to its remarkable overall properties, for instance, single-atom-thick two-dimensional conjugated structures, room-temperature stability, ballistic transport, and large available specific surface areas.

### I.1.1 Motivation - Thesis work summary

Consequently, the aim of this Ph.D. is to introduce first the overall interest of Surface Acoustic Wave (SAW) devices based on carbon allotropes, such as CNTs and graphene, especially used for environmental or bio-sensing applications i.e. Volatile Organic Compounds (VOCs) as biomarkers in breath. Further, this work is illustrated with a versatile acoustic wave transducer, functionalized with Graphene Oxide (GO), synthesized for ethanol, toluene, ammonia, carbon dioxide, nitrogen dioxide and humidity detections. The devices were designed, simulated, fabricated and characterized according to the target selection and the aspects of the SAW devices. For example, particular ratios between the length and volume of the deposited graphene on SAW devices were selected in order to detect sub-ppm concentration levels of  $\text{NH}_3$  and  $\text{NO}_2$ , respectively. Further, the novel properties of the graphene-based acoustic wave devices were studied and modified according to their optimal detection levels and validated over any further electrical and vapor characterization measurements.

Moreover, the devices were characterized by a Vector Network Analyzer (VNA), Raman spectroscopy, Scanning Electron Microscopy (SEM) and Atomic Force Microscopy (AFM), performed after each step of the fabrication, attesting that our method has a significant impact to the quality performance of the graphene-based surface acoustic wave devices. We have subsequently employed particular analytical modeling to investigate the electro-mechanical



properties of the GO, as well as to extract the elastoviscosity parameters of several GO layers and their impact on the acoustic devices, theoretically and experimentally. While that, we observed a strong correlation of the results with the number of coatings of the GO solution on the supported SiO<sub>2</sub>, since the properties of the GO fabricated materials were highly dependent on the specifically designated thicknesses, themselves intrinsically influenced by the material viscosity and Young's modulus. It has been previously reported in the literature that Young's modulus generally decreases with increasing of the GO thickness. Instead, we conclude that the number of the GO layer samples display a compressive internal strain, which does not fully relax after the fabrication process. We attribute this behavior to the uncontrollable large number of the graphene-based oxide sites during the fabrication process, as it has been observed later on the Raman spectra, respectively.

Finally, we have studied the gas sensing characteristics of our devices at room temperature as well as at higher temperatures up to 60 °C. The main reason that the temperature was kept at low levels was to test our devices in a very competitive way based on the current industrial demands, minimizing energy consumption, and/or to overcome some of the latest literature detection levels. The measurements confirmed that some of the detections were efficient based on the graphene devices, and as a result, it is possible to open a new discussion regarding the geometry and the morphology of the very specific GO materials. Some of the device measurements were attributed to a better understanding of the detection mechanisms such as physical or chemical adsorption and further in many cases by distinguishing the adsorption and absorption phenomena. At very low concentration levels of the VOCs, we have observed signatures of few Hz variations for a 100 MHz resonant frequency, but high enough, which implies that further investigation is needed to identify selectivity or specificity levels of certain target analytes. Based on the different geometry and thickness levels, the dominant mechanisms may vary in our samples. At higher concentration levels, the sensitivity showed frequency/temperature-robust results according to the very stable oscillation levels which could be identified as the baseline or initial detection levels of each target analyte, subsequently.

### 1.1.2 Significance of this work

The significance of this thesis is related to a high-yield fabrication method to obtain functionalized GO-based acoustic wave devices. Importantly, we focus on the scalability of the inkjet-printed fabrication process, as well as its compatibility with the existing SiO<sub>2</sub> technologies. To address several issues and to provide reproducibility and stable sub-ppm detections of the targeted Volatile Organic Compounds (VOCs), we have developed a fabrication scheme based on GO grown by inkjet-printing / Drop on Demand (DoD) deposition method. Different methods were used in a similar way on the acoustic wave devices, thus providing efficient results but not in the scalable route of the industrial demands. One of the most crucial steps of the fabrication process was related to the efficient preparation of GO solutions on the SiO<sub>2</sub> substrate to suspend the functionalized GO layers on the acoustic wave devices properly. It is often reported in the

literature that at this stage, it is very difficult to distinguish the atomic layers by a simple method without collapsing the GO layers together. We have found that apart from this effect, the quality of the oxidation process of GO and the pre-treatment preparation processes on the SiO<sub>2</sub> substrates were essential key parameters to successfully functionalize several graphene-based acoustic wave devices. Only when the quality of the GO solution was highly improved, were we able to achieve remarkable results regarding the VOCs and the water vapor detections, as well as to provide useful information about the vapor adsorption kinetics phenomena.

During this research, several exposure vapors such as NH<sub>3</sub>, NO<sub>2</sub>, C<sub>2</sub>H<sub>6</sub>O, C<sub>7</sub>H<sub>8</sub> and H<sub>2</sub>O, were investigated. The aforementioned compounds are known to affect the environment and human health if an over-exposure occurs. By employing the novel graphene-based materials on the proposed acoustic wave devices, the gas sensing performance was explored for different concentration levels (ppm / sub-ppm monitoring conditions). In each specific application, stringent requirements are demanded from the sensing system, especially for the acoustic sensor itself.

### 1.1.3 Organization of the dissertation

The objective of this thesis is to investigate the nanostructured materials (e.g. graphenes) in the form of thin films for gas sensing applications. The thesis is primarily devoted to this topic, and is divided as follows:

Chapter I presents the motivation and the author's contributions based on the current literature and introduces a literature review regarding the SAW devices based on alternative sensing materials and further, highlights the gas sensing properties of the Love wave devices based on carbon allotropes.

Chapter II presents premises of the aforementioned GO nanostructured material and its tailoring properties from the material's perspective. Further analysis describes material synthesis with particular emphasis on graphene's oxide characterization methods (SEM, FEM, Raman, AFM, etc.), as well as its electro-mechanical properties based on relative deposition techniques (Drop - Casting, Inkjet - Printing).

Chapter III presents the theoretical and experimental methods used for the graphene oxide sensing layers. Moreover, it analyzes the aspects of FEM and analytical techniques to explore the fabrication of multi-sensory devices.

Chapter IV focuses on the vapor sensing performance of the GO-based acoustic wave sensors regarding the C<sub>2</sub>H<sub>6</sub>O, C<sub>7</sub>H<sub>8</sub>, NH<sub>3</sub> and NO<sub>2</sub> detection mechanisms at sub-ppm levels. Notably, RH mechanisms were proposed on a basis of multi-layer adsorption kinetics. The vapor experimental conditions and calibration systems are also described in this chapter.

General conclusion and prospects conclude the thesis, and suggest the possible future works.



## I.2 Literature review – Materials and SAW devices for gas sensing applications

### I.2.1 Introduction - Gas/Vapor sensing applications

Nowadays, energy and environmental issues brought about by agriculture, transport and industry [1] have become major challenges strongly influencing the public health and social behavior all over the world. VOCs represent major public concerns due to their widespread use in commercial products (aerosol and adhesives) and in industrial processes [1]. In high concentrations, they are associated with cancer and damage to the central nervous system and are also known to affect developing embryos [2]. For these reasons, gas-vapor sensing applications have earned an excellent deal to answer societal challenges. Gas sensing technologies have emerged due to the common applications within the areas of the high interest like industrial production (e.g., alkane series detection) [1],[3]; automotive applications (e.g., VOC generated emissions from vehicles) [4]-[5]; medical applications (e.g., human modality representatives in a virtue of electronic olfactory systems) [6]-[7]; air quality management (e.g., detection of in-house pollutants based on natural sources) [2]-[8]; environmental studies (e.g., greenhouse emission monitoring) [9]-[10].

Thus, gas emerging applications have been engaged into numerous activities in environmental control and manufacturing, as well as domestic and foreign public health policies. These applications require precise real-time measurements for controlling and monitoring plenty of harmful analytes to increase industrial productivity and safety by narrowing the environmental pollution within limits to maintain World Health Organization (WHO) regulations in agreement with the public health and safety guidelines, annually [11]-[12].

Along similar lines, humidity also causes serious side effects from respiratory problems to exhibiting symptoms of various molds and harmful bacteria [13]. Furthermore, detection and control of environmental humidity has direct consequences in industrial processes [14] and environmental contamination [15].

The lack of embedded detection systems and device selection in the aforementioned purposes can greatly cause difficulties on the evaluation of the effectiveness of environmental policies and also generate similar problems in industry. There are several examples that environmental concerns have been grown exponentially, such as the greenhouse effect, since carbon monoxide emissions have to be monitored annually. It strongly influences the public health and the social behavior all over the world, as reported by WHO and NASA [16]-[17], respectively. Since air pollution affects significantly the life expectancies in a yearly basis evidence [18], there is a high necessity for embedded- advanced and monitoring detection systems for awareness to prevent this environmental threat to reoccur and to ensure that pollution is not beyond the safety limits, thus highlighting the importance of gas sensors. Moreover, the use of flammable gas species such as  $\text{CH}_4$  and  $\text{H}_2$  in domestic houses [19], the toxic or irritating-smell gases such as  $\text{H}_2\text{S}$  and  $\text{NH}_3$  used

in industrial processes [20] and the sensing demands for VOCs in food industry [21] reveal that multi-sensory devices are vitally important in everyday life.

Since, gas sensors are important for controlling industrial health and safety, domestic and environmental monitoring, each application places various requirements on the sensor systems, however the aims remain the same: to achieve accurate and stable monitoring of the target analyte in the range of % to parts per trillion (ppt) concentrations [22] depending on the target analyte and the equivalent exposure limits.

## 1.2.2 SAW chemical sensors

Chemical sensors have been used widely for gas discrimination and quantification in several emerging gas sensing technologies [23]-[24]. Today one of the major outstanding challenges we face on the interaction of the gas species with sensing layer materials [25] is the specified-functionalized materials in terms of structural [26], chemical [27], and morphological attributes [28] that require sophisticated engineer solutions in order to enhance their gas sensing properties [25]-[29]. Many studies [30]-[31] have been realized for various gas sensing technologies, especially based on SAW sensor devices, [32]-[33]. Between them, the fundamental research areas that receive the highest attention have been narrowed to the investigation of different types of SAW designs, novel sensing layers or over-layer functionalization [34]-[35] / immobilization [36] along with industrialization-based techniques. Since the particular demands for gas sensing devices have been analyzed above, a brief classification of SAW device technologies is now given, accompanied by the acoustic wave family, since it is commonly used as a stand-point detection device for environmental applications. Moreover, current research status and recent developments in the field of SAW sensory devices are reported, to provide any sufficient discussions or conclusion regarding the aforementioned problems and solutions.

The main application of SAW devices is as sensors as part of a chemical sensing system [37]. It consists of a target analyte interrogation unit (e.g. sensing layer), the emitter and receiver of the generated and propagated acoustic waves, respectively, and the acoustic path or commonly named as SAW delay line [37]-[38].

In that sense, the type of the acoustic wave devices [37]-[38] is frequently diversified according to the acoustic wave propagation characteristics. The general SAW delay-line principle is based on the emitting and receiving electrodes to generate acoustic waves, as represented in Figure 1-1. Thus, when an alternative electric field is applied to an InterDigital Transducer (IDT), patterned on a piezoelectric surface, it generates acoustic waves (commonly named reverse - piezoelectric effect) [37]. The properties of the piezoelectric material, such as the crystallographic orientation, thickness and material selection determine the family of the acoustic wave sensor and affect the acoustic wave propagation velocity [38]. The piezoelectric substrates that are widely used in the field of acousto-sensors are Quartz ( $\text{SiO}_2$ ), Lithium Tantalite ( $\text{LiTaO}_3$ ), Lithium Niobate ( $\text{LiNbO}_3$ ), Zinc Oxide ( $\text{ZnO}$ ) and Aluminium Nitride ( $\text{AlN}$ ). A key parameter that plays a

significant role in the material selection of the piezoelectric substrates is the electro-mechanical coupling coefficient ( $K^2$ ) [39]. This is a measure of how effectively a given piezoelectric substrate can convert an applied electric signal into a mechanical displacement and vice versa [40].

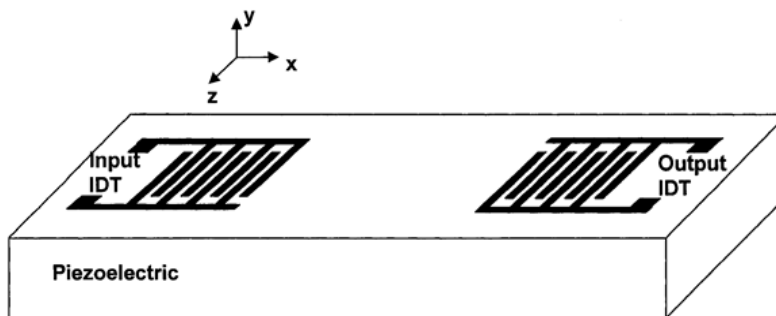


Figure 1-1 Example of a SAW delay-line with IDTs defined on a piezoelectric substrate [37].

In the case of a SAW delay line based on the most renowned Rayleigh wave polarization, the acoustic wave propagation is maintained along the x-axis, which is also the X-crystallographic axis, and the particle displacements occur in the sagittal plane (x-and y- axes on the Figure 1-1), thus offering ascend to an ellipsoidal movement. During the propagation of the generated waves (along the surface), most of the ‘acoustic’ wave energy is focused within a particular depth of the substrate, at the surface.

By principle, the traveling path of the acoustic waves, as appeared in Figure 1-1, is used to maintain the wave propagation characteristics. The traveling acoustic waves are converted finally into an electrical signal by the output-IDTs. The delay-time can be calculated by the following form  $t = L/v_0$ , where L represents the center-to-center distance between the input and output IDTs and  $v_0$  represents the SAW phase velocity.

Furthermore, the IDTs spatial periodicity  $\lambda$  defines a particular wavelength at which the acoustic waves generated by the adjacent pairs of electrodes will be added in phase. Finally, the essential key properties regarding the acoustic wave characteristics could be included in the number of the finger electrodes, the acoustic aperture, the center-to-center IDTs distance and the transducer periodicity.

### 1.2.3 Acoustic wave families

Acoustic wave based sensors incorporate plenty of devices according to their multi-variational properties and material characteristics. These sensory devices are commonly based on the diversity of the acoustic wave polarization and propagation mechanisms, determined by the nature of the substrate, the crystallographic orientation, the direction of particle displacement and the sensing material. As described in a previous section, the aforementioned structure of the IDT-

electrodes is used to manipulate the profile of the acoustic waves and their propagation characteristics, since the acoustic waves a) could travel through the bulk of the substrate material, b) could be guided by an over-layer, or could be guided by reflections from multiple surface areas, with respect to the application environmental demands (gas/liquids) [41].

Regarding the polarization of the acoustic waves, three types can be distinguished such as longitudinal, transverse vertical and transverse horizontal. The particle direction of the longitudinal waves or compressional waves should be regarded as parallel to wave propagation direction, whilst the particle displacement of the transverse waves or shear waves is perpendicular to the propagation direction. Furthermore, the acoustic wave devices can be separated into three different categories, such as Bulk Acoustic Wave (BAW), Surface Acoustic Wave (SAW) and Acoustic Plate Mode (APM) devices [42]. This classification can be divided into various sub-categories that already exist in the literature [37]-[38], [41], depending on the generation of the acoustic waves and their propagation mode. In particular, the BAW devices are divided into Quartz Crystal Microbalance (QCM) [43] and Film Bulk Acoustic Resonators (FBARs) [44], the SAW family is represented by Rayleigh, Shear-Horizontal Surface Acoustic Wave (SH-SAW) [45], Surface Transverse Wave (STW) [46] and Love wave devices [47] while the APM family includes the Shear-Horizontal Acoustic Plate Mode (SH-APM) [48] and the Flexural Plate Wave (FPW) [49] devices. Precisely, in the first group (BAW devices), the polarization can be longitudinal or transverse, thus it is the volume of the material (substrate) that deforms, allowing the acoustic wave to propagate unguided. The SAW devices can be represented by a Rayleigh wave [50] (longitudinal and transverse), or by the waveform of Bleustein-Gulyaev [51], which is polarized in the transverse horizontal plane. Generally, in SAW devices, the acoustic wave propagates guided or unguided, along the surface of the substrate [52]. When the SAW is unguided and shear polarized, the generated acoustic waves can be represented by the SH-SAW device, whilst the guided and shear polarized acoustic waves corresponding to the guided SH-SAW or Love wave mode devices [52]-[53]. In the third group (APM devices), the wave propagates in the volume of the substrate material, either in the form of two Rayleigh waves (one per side) [45], such as a Lamb wave [54] or in the form of a transverse horizontal wave undergoing reflections at both surfaces of the material plate (SH-APM) [52].

Depending on the classification of the acoustic waves (Figure 1-2), they can be utilized in liquid or gaseous environments or both. The primary norms of the subsequent-based detection systems are ordered by the nature of the acoustic wave propagation characteristics.

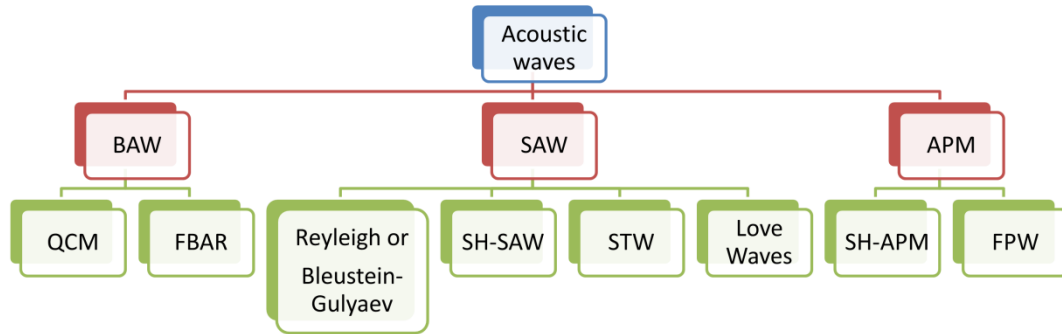


Figure 1-2: Acoustic Wave devices can be classified into three main groups depending on the generation of the acoustic waves. Severe sub-groups can be identified for further analysis based on the wave propagation characteristics, as depicted from [37]-[38], [41], [52].

The impact of high demanding performances in environmental applications necessitates an overview perspective of the acoustic wave family devices, according to their generation and propagation properties.

### 1.2.3.1 QCM

One of the most prototypical devices in the field of acousto-sensors is represented by QCM [52]. Analytically, as illustrated in Figure 1-3, a typical QCM device is based on the oscillation frequency of the vibrating crystal which is sandwiched between two electrodes. The mass sensing mechanism is related to the resonance frequency of the quartz crystal generated by an applied voltage via the electrodes. Therefore, any mass or elasto-viscosity variations of a “sensitive” layer added on the surface of the QCM will report frequency shifts in a coherent manner.

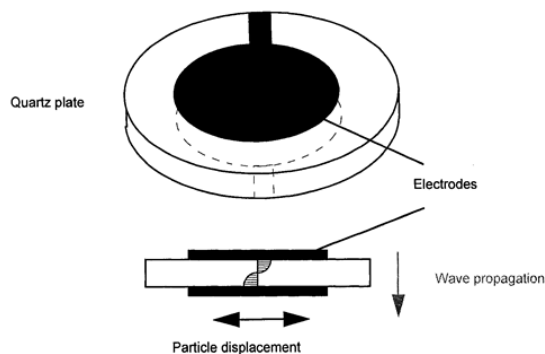


Figure 1-3 Typical representation of the QCM device [55].

### 1.2.3.2 FBAR

FBAR devices have attained a great deal of scientific research, especially in mass [56], pressure [57] and temperature [58] detection applications. FBAR sensors are closely related with QCM devices in regards of device structure or principle characteristics (Figure 1-4). However, the significant differences are based on the selection of the piezoelectric materials, as well as on the



inherent capabilities of FBAR that operate in higher resonance frequencies (high resolution) in comparison with QCM devices, thus FBAR devices report increased sensitivity detections to any mass or elasto-viscosity variations on the top electrode.

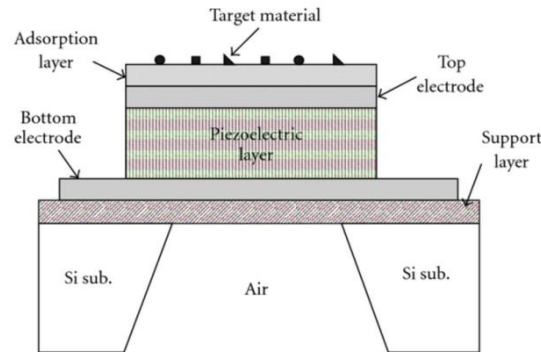


Figure 1-4 Typical representation of the FBAR device[59].

However, a few drawbacks of FBAR devices reported loss in mechanical energy by the presence of liquid environments, as well as high fabrication costs [60]. Hence, by their very nature, these devices do not contribute to current thesis sustainability.

### 1.2.3.3 Rayleigh and Bleustein-Gulyaev

Rayleigh waves are a type of surface elastic waves, which are an honorable member along the acoustic waves family. Often, they are represented by a seismic surface wave that causes shaking of the Earth's surface in an elliptical motion and further used to study earthquake mechanisms [61]. At November's proceedings in 1885 [62], Lord Rayleigh predicted their existence in isotropic solids, where the waves cause particles to maneuver in elliptic displacement in planes normal to the surface and parallel to the wave propagation direction (Figure 1-5). Along similar lines, they have attained a great amount of research interest, since they are responsible for a variety of temperature [63], pressure [64], and vapor [65] sensing applications. Nonetheless, regarding the SAW device performances, especially in liquid environments, Rayleigh devices have reported low sensing performance characteristics, mainly due to generation of compressional waves and high loss in energy confinement [66].

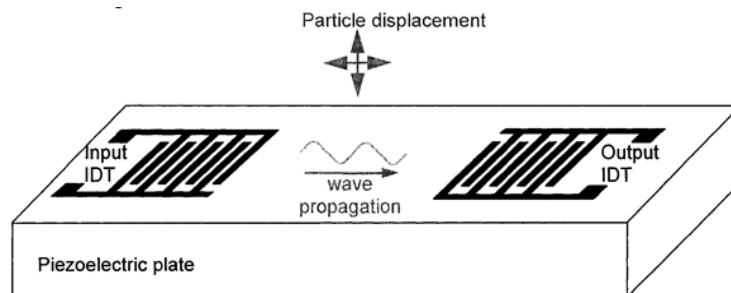


Figure 1-5 Typical representation of the Rayleigh mode SAW device [55].

On the other hand, Bleustein-Gulyaev (BG) waves have shown a particular interest in the scientific literature, since they have been used for several applications in liquid environments. For example, measuring viscosity characteristics in liquids under different pressures could be tedious by applying conventional methods, whereas BG waves have reported great performances [67], since they operate as pure shear horizontal waves. In the presence of viscous liquid, the wave energy is concentrated in the region adjacent to the piezoelectric surface associated with liquids, thus providing to the particles, manoeuvres that are in parallel to its surface and normal to the propagation direction.

#### 1.2.3.4 SH-SAW

In general, the SH-SAW devices have attracted a significant amount of attention within the research community, mainly due to high sensitivity performances in liquid environments [68], as well as in bio-detection applications [41]. The primitive conditions that a pure shear horizontal wave can be generated, usually require the commonly reported interdigitated transducers, an acoustic wave delay-line, and a piezoelectric substrate (Figure 1-6). The main principle of these devices being based on the interactions that cause perturbations in the acoustic wave propagation [69] and translated into an electrical signal that can be measured in a simple manner, various applications can be encapsulated under the SH-SAW devices in order to interact with different gaseous [45] or liquid environments [70]. As for other acoustic wave devices, signal attenuation, phase wave velocity and frequency variations are representatives of the measured disturbances caused in the acoustic wave propagation, and thus specific detections could be identified uniquely according to the analyte selection.

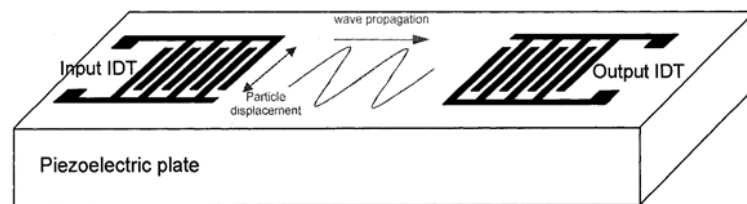


Figure 1-6 Typical representation of the SH-SAW device [55].

#### 1.2.3.5 STW

STW represent an alternative way in the acoustic waves family that provides efficiency in plenty of applications by utilizing materials and technology of the existing micro-fabrication technology. Along similar lines, they have gained an extensive amount of research interest as mass or viscosity sensors [71], because they exhibit great performances. As represented in the Figure 1-7, in sensor applications, the STW devices offer the convenience of launching and receiving waves by conventional electrodes that are shaped as parts of an overall grating structure

on the surface of the substrate [71]. In accordance with the illustrated Figure 1-7, the sensing principle of a STW device can be described by using a sensing layer that could react with preselected target analytes that are to be measured. Finally, STW devices can be easily considered as precursors of the Love wave devices, since by changing the metallic grating strip of electrodes to a thin solid film, the wave can be transformed from STW to Love wave [72].



Figure 1-7 Typical representation of STW device [72].

### 1.2.3.6 Love waves

Guided shear-horizontal waves were firstly described by Augustus Edward Hough Love [53] in his early attempts to explain seismic data that have played a significant role in the scientific literature. His work is represented by numerous contributions in the plurality of the scientific domains, being well-known for its mathematical expeditions in the theory of elasticity. Following his work on the structure of the Earth in *Some Problems of Geodynamics*, he won the Adams prize in 1911, when he developed a mathematical model of surface waves, known as Love waves.

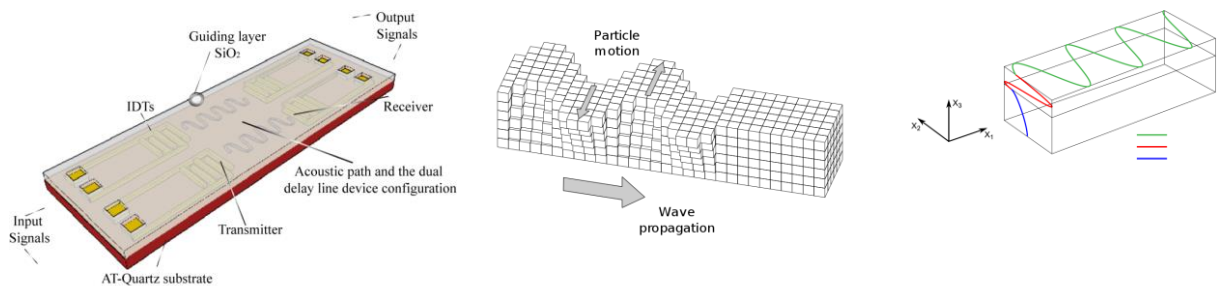


Figure 1-8 Typical representation of Love wave sensor upon dual delay line device configuration; Love wave propagation direction and particle motions [73], [74], [75].

Besides the theoretical premises of Love waves, they have been reported in many applications for academic [76]-[77] or industrial purposes [71], as well as they can be easily incorporated in sensor devices [35], as shown in the left side of Figure 1-8. Love wave technological nodes are in agreement with the semiconductor fabrication processes of Microelectromechanical systems (MEMS), thus allowing Love wave devices to be integrated in a single chip applications [78], such as lab-on-a-chip devices. In that sense, they have repeatedly shown great performances in

bio-sensing [79] and microfluidic [80] applications, and therefore leading the way towards sensor activities [81].

Furthermore, according to the Love wave principle, the particle motion can be represented by a horizontal line along  $[0, x_2)$ , perpendicular to the propagation direction along  $[0, x_1)$  and parallel to the surface, as represented in the right side of the Figure 1-8. From the wave's perspective, the particle motion can be decreased to a particular point of the sagittal plane due to the depth-dependent restrictions that should be followed to permit the Love wave excitation. According to the surface boundary conditions, the shear bulk wave velocity of an over-layer (i.e.  $\text{SiO}_2$ ) must be lower than the substrate's shear bulk wave velocity (i.e. AT-cut quartz), in order to maintain the critical angle so that shear horizontal reverberations can be totally trapped, and therefore allow the generation of Love waves [82]. Moreover, the Love waves decay exponentially with the depth, since their energy confinement is maintained to the over-layer surface. Along similar lines, acoustic wave perturbations can induce variations in the wave propagation characteristics, especially caused by gravimetric [83] or viscoelastic [84] effects, thus a resulting attenuation in the output signal (Figure 1-8, wave's representation [75]).

However, unlike many previous studies [85]–[87] of the Love wave sensors, this research only examined the Love wave device's performances, effects and aspects under vapor environments [88]–[89], especially using graphene-sensitive [90]–[91] layers from the carbon's materials family. The current research of Love wave devices has therefore highlighted the effectiveness of the aforementioned bare and coated sensors, as well as reported results in the literature of the acoustic wave sensors. It shed light on tedious, complex and often controversial [90] concepts regarding the viscoelastic properties of graphene-based Love wave devices, and further studied the variability emerged across humid vapor detections [92] towards multi- and monolayer adsorption kinetics (i.e. modified Brunauer-Emmett-Teller method [92]).

### 1.2.3.7 SH-APM

A different sub-type of the acoustic waves family, similarly well-known for its device's performances, is the commonly reported SH-APM devices. The term APM, is related to the wave excitation in a plate. The plate mode differs according to the propagation direction of the waves, and the particle motion inside the plate. The most attractive category of the acoustic plate modes is demonstrated by the SH-APM, especially due to the sensing performances and the non-coupling effect in liquid environment applications [41], [93]. As commonly reported for the acoustic devices, similar characteristics may apply to the SH-APM devices (wave perturbation, detection method, etc.) regarding the piezoelectric material and the IDTs, in which plenty of sophisticated configurations can prevent any contact of the electrodes with the liquid sensing environments.

### 1.2.3.8 FPW

FPW are sauntered as the ‘medium’ rendition towards SAW devices. The basic premises of acoustic’s theory are related with the advanced fabrication practices of the acoustic wave devices, that employ an excitation of the piezoelectric substrate through the IDTs and confine the acoustic wave energy near to its surface. On these grounds, when the thickness of the piezoelectric substrate is very thin, and precisely lower than the wavelength of the acoustic wave, then Lamb waves can be generated, or commonly reported as Flexural Plate Waves. The significance of the Lamb wave devices occurs mainly in liquid sensing applications [94]; however they have shown a particular interest in recent literature [95], especially used as humidity sensors [96], thus overpassing challenges that are related to complex fabrication techniques.

## 1.2.4 Sensing materials for SAW devices and vapor detections

### 1.2.4.1 Overview of materials for SAW-based gas sensors

Besides the fact that WHO regulations are frequently changed, especially under air quality corrigendum [11],[97] the International Health Regulations (IHR) suggest, prevent and respond to severe chemical, physical or biological health risks. Subsequently, peerless challenges have emerged in the fields of chemical and bio- sensors, commencing from the design of specific material characteristics to the ability to solely detect and identify targeted analytes, selectively.

Aside from all these functional or chemical prerequisites, the sensitive and/or selective materials must be suitable with SAW devices, in terms of material integration and adhesion-related processes, thus providing efficient and low-cost devices towards global production. Many SAW devices are being referred into the spin-coating, spray-coating, inkjet-printing, sputtering, drop-casting and electro-spraying techniques, according to the nature and objectives of the sensing demands.

Nowadays, a step forward into the new era of SAW devices and engineering technology, there is plenty of science-based evidence to conquer the aforementioned challenges, since the scientific and technological wherewithal is supplied constantly by a variety of sophisticated materials, especially for vapor sensing applications. In particular carbons, metals, polymers, hybrid and meta- related materials have been reported for recognizing particular vapors and analytes, especially under functionalization of the sensing layer(s) or surface tailoring compliance. Selectivity is contingent upon a definition of ‘ability of the chemical-SAW sensor to respond solely to a group of analytes or even specifically to a single analyte’. Furthermore, these novel materials are continuously evolved through the ‘Darwinism’ material selection, which is put forward under the guise of its sensing and recognition effectiveness; nonetheless they aren’t followed by the publish or perish norm philosophy, since most of the time they are adopted by industry.

Therefore, as illustrated in Figure 1-9, plenty of materials have been reported for vapor sensing applications. The foregoing discussion implies that selective responses and vapor recognitions can

be categorized (Table 1.1) according to the nature of the sensing material and device integration criteria consistent with the available SAW sensor's performances.

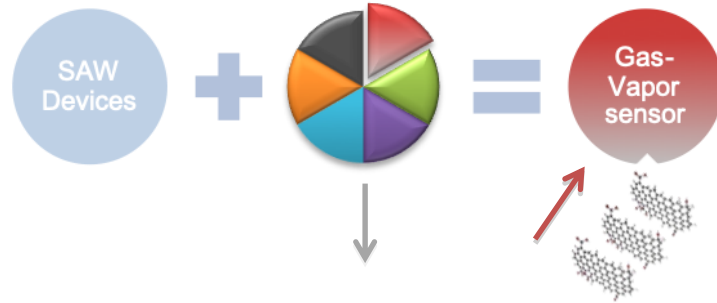


Figure 1-9 An illustrative representation of the material family, recently used as vapor sensing layers on SAW devices. The material classification is descended and inspired by [98] to perceive larger material diversification and a plurality conception, which can be conceived and delivered in an interesting and carbon related manner for SAW devices.

Material family	Sensing (mono)-layers	Target Vapors	Sensitivity (Hz/ppm) or LOD (ppm)	Refs
<b>Metal and Metal oxide structures</b>	WO <sub>3</sub>	C <sub>2</sub> H <sub>6</sub> O / H <sub>2</sub> O	238 Hz/ppm, LOD 10 ppm for C <sub>2</sub> H <sub>6</sub> O at 300 °C;	[99]
	Pd electrodes	H <sub>2</sub>	6-8 Hz/ppm, LOD 100 ppm for H <sub>2</sub> /N <sub>2</sub> at 250 °C;	[100]
	Indium Tin Oxide (ITO)	NO <sub>2</sub>	51.5 °/ppm, LOD 5 ppm for NO <sub>2</sub> /N <sub>2</sub> at 240°C;	[101]
	Pt/ZnO nanoparticles	H <sub>2</sub>	5.5 Hz/ppm, LOD 2500 ppm for H <sub>2</sub> /N <sub>2</sub> at Room Temperature [RT];	[102]
	In <sub>2</sub> O <sub>3</sub>	H <sub>2</sub>	8.8 Hz/ppm, LOD 100 ppm for H <sub>2</sub> /N <sub>2</sub> at RT;	[103]
	ZnO, SnO <sub>2</sub> , TeO <sub>2</sub> , TiO <sub>2</sub>	NH <sub>3</sub>	ZnO (40 nm) ~3 Hz/ppm, LOD 400 ppm for dry NH <sub>3</sub> /N <sub>2</sub> at RT;	[104]
<b>Carbon based / Carbon hybrid materials</b>	Graphene-like nano-sheets (incomplete GO reduction)	H <sub>2</sub> / CO	0.6 Hz/ppm (H <sub>2</sub> ), LOD 600 ppm for H <sub>2</sub> /air at RT; 8.5 Hz/ppm (CO), LOD 125 ppm for CO/air at RT;	[105]
	Graphene Oxide (Drop-Casted whole device)	H <sub>2</sub> O	~53 kHz / % RH, LOD 0.5 %RH for H <sub>2</sub> O/N <sub>2</sub> at RT;	[106]

	MWCNTs/Nafion nanofibers	H <sub>2</sub> O	~400 kHz/%RH, RH detection precision 0.5 % RH at RT;	[107]
	Graphene Oxide (Inkjet-Printed between IDTs)	C <sub>2</sub> H <sub>6</sub> O / C <sub>7</sub> H <sub>8</sub> / H <sub>2</sub> O	30 Hz/ppm (C <sub>2</sub> H <sub>6</sub> O), LOD 100 ppm for C <sub>2</sub> H <sub>6</sub> O/N <sub>2</sub> at RT; 24 Hz/ppm (C <sub>7</sub> H <sub>8</sub> ), LOD 100 ppm for C <sub>7</sub> H <sub>8</sub> /N <sub>2</sub> at RT; 2.4 kHz/%RH, RH monolayer ~173 kHz for H <sub>2</sub> O/N <sub>2</sub> at RT;	[92]
	Graphene Oxide (Drop-Casted between IDTs)	C <sub>2</sub> H <sub>6</sub> O / H <sub>2</sub> O	112 Hz/ppm (C <sub>2</sub> H <sub>6</sub> O), LOD 100 ppm for C <sub>2</sub> H <sub>6</sub> O/N <sub>2</sub> at RT; 6.4 kHz/%RH, LOD ~2%RH for H <sub>2</sub> O at RT;	[89]
	Graphene/PANI	NO	~320 Hz/ppm, LOD 0.5 ppm for NO/air at RT;	[108]
	Graphene (Liquid phase exfoliated graphene / defected Graphene Oxide)	NO <sub>2</sub>	25 Hz/ppm, LOD ~0.5 ppm for NO <sub>2</sub> /air at RT;	[109]
	Graphene-nickel (Ni)-L-alanine	CO <sub>2</sub> , Ar, O <sub>2</sub> , C <sub>2</sub> H <sub>6</sub> O	2.1 Hz/ppm (0-2000 ppm of CO <sub>2</sub> /N <sub>2</sub> ), LOD 200 ppm for CO <sub>2</sub> /N <sub>2</sub> at RT;	[110]
	SWCNTs / MWCNTs	C <sub>2</sub> H <sub>6</sub> O / C <sub>4</sub> H <sub>8</sub> O <sub>2</sub> / C <sub>7</sub> H <sub>8</sub>	6.89 kHz/ppm (SWCNTs), LOD 1.3 ppm for C <sub>2</sub> H <sub>6</sub> O/N <sub>2</sub> at RT; 5.45 kHz/ppm (SWCNTs), LOD 1.6 ppm for C <sub>4</sub> H <sub>8</sub> O <sub>2</sub> /N <sub>2</sub> at RT; 7.47 kHz/ppm (SWCNTs), LOD 1.2 ppm for C <sub>7</sub> H <sub>8</sub> /N <sub>2</sub> at RT;	[111]
	MWCNTs-COOH-Poly(n,n-dimethylamino propylsilsesquioxane) [SXNR]	C <sub>2</sub> H <sub>6</sub> O	9 kHz / ppm (oxidized MWCNTs or MWCNTs-COOH-SXNR), for C <sub>2</sub> H <sub>6</sub> O/N <sub>2</sub> at RT;	[112]
	10 monolayers of SWCNTs in CdA LB / 30 monolayers of SWCNTs-in-CdA LB	NO <sub>2</sub> / NH <sub>3</sub> / H <sub>2</sub>	3.3×10 <sup>-2</sup> °/ppm (SWCNT-in-CdA LB), LOD 0.16 ppm (30 monolayers of SWCNT-LB) for NO <sub>2</sub> /air at RT; 4.7×10 <sup>-4</sup> °/ppm (SWCNT-in-CdA LB - 10), LOD 33 ppm for NH <sub>3</sub> /air	[113]

			at RT; 1.8×10 <sup>-5</sup> °/ppm (SWCNT-in-CdA LB - 10), LOD 330 ppm for H <sub>2</sub> /air at RT;	
	Cu nanoparticles-SWCNTs	H <sub>2</sub> S / H <sub>2</sub> / C <sub>2</sub> H <sub>6</sub> O / C <sub>3</sub> H <sub>8</sub> O	~2.6 kHz / ppm for H <sub>2</sub> S/Air, LOD 5 ppm at RT and selectivity for H <sub>2</sub> S/Air at 175°C;	[114]
	Polyepichlorohydrin [PECH] with different % MWCNTs / Polyetherurethane [PEUT] with different % MWCNTs	C <sub>8</sub> H <sub>18</sub> / C <sub>7</sub> H <sub>8</sub>	~1Hz/ppm (PECH with 5% of MWCNTs), LOD 9.2 ppm for C <sub>8</sub> H <sub>18</sub> /air at RT; ~4.4 Hz / ppm (PECH with 5% of MWCNTs), LOD 1.7 ppm for C <sub>7</sub> H <sub>8</sub> /air at RT;	[115]
	Polyisobutylene (PIB) mixture with MWCNTs	C <sub>8</sub> H <sub>18</sub> / C <sub>7</sub> H <sub>8</sub>	~8.1 Hz / ppm (PIB with 2% of MWCNTs), LOD 25 ppm for C <sub>8</sub> H <sub>18</sub> /air at RT; ~3.3 Hz / ppm (PIB with 2% of MWCNTs), LOD 25 ppm for C <sub>7</sub> H <sub>8</sub> /air at RT;	[116]
	Polyallylamine [PAA]-amino-CNTs / Polyethyleneimine [PEI]-amino-CNTs	CO <sub>2</sub>	~0.3 Hz / ppm (PEI-amino CNTs), LOD 500 ppm (PAA-amino-CNTs) for CO <sub>2</sub> /air at RT;	[117]
<b>Polymers</b>	Teflon AF2400	CO <sub>2</sub>	~2.1 ° / ppm, LOD 75 ppm for CO <sub>2</sub> /N <sub>2</sub> at RT;	[101]
	Polyepichlorohydrine [PECH]	C <sub>7</sub> H <sub>8</sub>	2 Hz/ppm (PECH with ZnO device - 10% O <sub>2</sub> ), LOD 25 ppm for C <sub>7</sub> H <sub>8</sub> /air at RT;	[118]
	[PIB], [PECH], [PEUT]	C <sub>8</sub> H <sub>18</sub> / C <sub>7</sub> H <sub>8</sub> / C <sub>4</sub> H <sub>8</sub> O	4 Hz /ppm (PEUT - S3 device) for C <sub>8</sub> H <sub>18</sub> /air at RT, LOD – probabilistic neural network (PNN) classification of different gas concentrations (C <sub>8</sub> H <sub>18</sub> / C <sub>7</sub> H <sub>8</sub> / C <sub>4</sub> H <sub>8</sub> O) with a 100% success rate;	[119]
	Polymethyl[3-(2-hydroxy) phenyl]siloxane [PMPS]	C <sub>3</sub> H <sub>9</sub> O <sub>3</sub> P (DMMP)	3 kHz/ppm (PMPS), LOD 5 ppm for C <sub>3</sub> H <sub>9</sub> O <sub>3</sub> P/N <sub>2</sub> at RT;	[120]



	Poly(o-phenylenediamine) - Molecularly Imprinted Polymers	$C_3H_9O_3P$ (DMMP)	487 Hz/ppm, LOD 0.1 ppm for $C_3H_9O_3P/N_2$ at RT;	[121]
	[PECH], [PEI], [PIB]	$CH_2Cl_2$ (DCM) / $C_4H_8O_2$ (EtOAc) / $C_3H_9O_3P$ (DMMP) / $C_4H_{10}FO_2P$ (GB)	649 Hz/ppm (GB), LOD $9.24 \times 10^{-3}$ ppm for $C_4H_{10}FO_2P/N_2$ at RT;	[122]
<b>Supramolecular materials</b>	Tert-butylcalix[4] arene	$C_2Cl_4$ (Tetrachloroethylene)	3.5 Hz/ppm, LOD 50 ppm for $C_2Cl_4$ /air at RT;	[123]
	Calix[4] - Calix[6] arenes	$C_8H_{10}$ / $C_7H_8$ / $C_2Cl_4$	6 Hz/ppm (P-tert-butylcalix[4]arene), LOD 20 ppm for $C_8H_{10}$ /air at RT;	[124]
	(3) Calixarene layers - Poly(diallyldimethylammonium chloride) [PDDA]	$C_2Cl_4$ / $C_2HCl_3$ / $CHCl_3$	~8.7 Hz/ppm ( $C_2Cl_4$ /air) ~4.5 Hz/ppm ( $C_2HCl_3$ /air) ~3.7 Hz/ppm ( $CHCl_3$ /air) for (3)-Calixarene layers-PDDA, at 15°C;	[125]
<b>Self-assembled monolayers (SAMs)</b>	Self-assembled Calixarene Derivatives	$C_3H_9O_3P$ (DMMP) / $C_7H_{17}O_3P$ (DIMP)	~4.4 kHz/ppm (DMMP - $5 \text{ mg/m}^3$ ), LOD $19.7 \times 10^{-3}$ ppm ( $0.1 \text{ mg/m}^3$ ) for $C_3H_9O_3P/N_2$ at 28°C;	[126]
	Siponate DS-10 / PolyEthyleneGlycol [PEG1000]	$C_6$ alcohols / $C_7H_{14}O_2$ (n-amyl acetates)	-, LOD < 1-2 ppm for odorants/air at RT;	[127]
	Self-assembled derivatives (lipopolymeric layers)	$C_4H_{10}O$ (n-butanol)	~145 Hz/ppm (Quartz ball-SAW device), LOD $29 \times 10^{-3}$ ppm for $C_4H_{10}O$ /air at RT;	[128]
<b>Nano-modifiers / Nano-composites</b>	$SiO_2/Si$ - MWCNTs in Polyethylenimine [PEI]	$C_2H_6O$ / $CH_3OH$ / $C_7H_8$	1.19 Hz/ppm (MWCNTs-PEI), LOD 15.2 ppm (Si/SiO <sub>2</sub> -PEI) for $C_2H_6O$ /air at RT;  1.14 Hz/ppm (MWCNTs-PEI), LOD 16.7 ppm (Si/SiO <sub>2</sub> -PEI) for $CH_3OH$ /air at RT;  1.23 Hz/ppm (MWCNTs-PEI), LOD 13.8 ppm (Si/SiO <sub>2</sub> -PEI) for $C_7H_8$ /air at RT;	[129]
	Surface-modified diamond nanoparticles	$C_7H_6N_2O_4$ (DNT) / $C_3H_9O_3P$	80 kHz/ppm (DNPs), LOD 0.2 ppm for $C_7H_6N_2O_4$ /air at RT;  4 kHz/ppm (DNPs), LOD 0.5 ppm	[130]

	[DNPs]	(DMMP) / NH <sub>3</sub>	for C <sub>3</sub> H <sub>9</sub> O <sub>3</sub> P/air at RT; 70 kHz/ppm (DNPs), LOD 30 ppm for NH <sub>3</sub> /air at RT;	
	Langmuir–Blodgett (LB) nanolayers DA, CA, DA- CA	C <sub>2</sub> H <sub>6</sub> O / CH <sub>3</sub> OH	16x10 <sup>-3</sup> Hz/ppm (DA - porous), for C <sub>2</sub> H <sub>6</sub> O/air at 35°C; 30x10 <sup>-3</sup> Hz/ppm (DA - porous), for CH <sub>3</sub> OH/air at 35°C;	[131]
	Laser-Deposited [LD] nanostructured of polyethylenimine [PEI]	C <sub>2</sub> H <sub>6</sub> O / CH <sub>3</sub> OH / C <sub>7</sub> H <sub>8</sub>	5, 4.5 and 5.4 Hz/ppm (LD-PEI), LOD 6, 6.7 and 5.6 ppm for C <sub>2</sub> H <sub>6</sub> O/air, CH <sub>3</sub> OH/air and C <sub>7</sub> H <sub>8</sub> /air, respectively at RT;	[132]
	Polyaniline/In <sub>2</sub> O <sub>3</sub> Nanofiber Composites	H <sub>2</sub>	1.1 Hz/ppm, LOD 600 ppm for H <sub>2</sub> /air at RT;	[133]
	ZnO nanorods	H <sub>2</sub>	183 Hz/ppm, LOD 500 ppm for H <sub>2</sub> /air at 265°C;	[134]

Table 1.1 Classification of alternative materials according to their nature, device integration, vapor selection and sensing properties criteria for SAW devices, adapted from [98].

From the outset of gas sensing applications, devices regarding the vapor detection [99] or gas [102]-[103] sensing applications have widely used metal oxide nanostructures as an enhancing layer, especially due to sensitivity and selectivity performances [99]-[104]. However, in many cases individual devices were able to perform, particularly at elevated temperature conditions [99]-[101]. The elevation of the temperature is usually based on the reaction heat between the gas species and the sensing layer that leads to the necessity for overcoming challenges like low energy consumption and sustainable gas detection devices at room temperature.

On the other hand, polymer based sensitive layers have been selected very often for the exploration of detection materials in the toolbox of SAW gas sensors. Polymer coated devices provide an attractive way to form the required shape and thickness of the sensing layer, which has proved some reversibility for gas sensor applications. These versatile polymers can be used at ambient temperatures [101], [118]-[122], which is a great advantage for vapor sensing applications due to lower energy consumption. Notwithstanding the easy fabrication processes of polymer coated structures, plenty of sophisticated polymer designs offer a route to vapor sensing materials with a good selectivity to certain analytes, such as for DMMP detections [120]-[122] for example, which insures high performance of the SAW sensors. However, a few polymer disadvantages include sensitivity to oxidation and humidity mechanisms or require a marginally complicate polymer preparation.

Supramolecular structures are large molecules formed by grouping or bonding smaller molecules together. They are usually generated through the developing of macro-molecules that are not covalently bonded, and thus form a desired shape or functionality. By taking advantage of the formed characteristics regarding the host (supramolecular) – guest (target analyte) interactions, particular structures can be obtained for specific sensing purposes. One great example such as calixarene sensing layers provides the aspect of molecular receptors for different analytes and exhibits high affinity and great selectivity towards vapor detections [123]-[125]. However, a common drawback that is affected by calixarene layers is that the supramolecular coated SAW devices tend to report cross sensitivities [125] towards Tetrachloroethylene ( $C_2Cl_4$ ), Trichloroethylene ( $C_2HCl_3$ ) and Chloroform ( $CHCl_3$ ) volatile compounds, respectively.

Self-assembled monolayers (SAMs) represent one very useful category of sensing layers for SAW devices. Since SAMs are molecular assemblies formed on surfaces, as well as organized into more or less large ordered domains, they can be efficiently used for specific analytes detection. There are plenty of interesting works in the literature [126]-[128] regarding the detection of vapor compounds, however one of the greatest assets in the field of SAW devices has been realized by calixarene derivatives [126] used as self-assembly molecular imprinted film, and thus showing high sensitivity detections of volatile agents like DMMP.

Nano-composites offer the opportunity to build certain blocks by a mixture of materials in the nanoscale arena in order to generate materials with novel properties used as sensing layers, especially in SAW devices. The idea of a mixture-based nanocomposites can be illustrated by the addition of  $SiO_2/Si$  nanoparticles and multi-wall carbon nanotubes (MWCNTs) embedded in polyethylenimine (PEI) [129], which has proved to be extremely useful for the detection of VOCs such as  $C_2H_6O$  (ethanol),  $CH_3OH$  (methanol) or  $C_7H_8$  (toluene).

Along similar lines, nano-modifiers or hybrid-based structures can be used as offered materials through a matrix for the preparation of sensing coatings on SAW devices. Improvements with high affinity towards specific compounds [130] such as  $C_7H_6N_2O_4$  (DNT),  $C_3H_9O_3P$  (DMMP) and  $NH_3$  have shown a great amount of interest in the literature, however for both cases (nano-composites and nano-modifiers) specificity still remains an issue [129], [130].

#### 1.2.4.2 Carbon-allotropes for SAW devices

As a preface, it is worth mentioning that the main aspects of this sub-chapter are focused on the graphene's material family and carbon related materials (graphene composites, defected graphene oxide, CNTs, etc.) used as sensing layers in SAW devices. This field has shown significant amount of interest by many scientists and engineers and it is constantly updated with exceptional impacts frequently, hence listing every single update would feel like a quota or Sisyphean from the ancient myths.

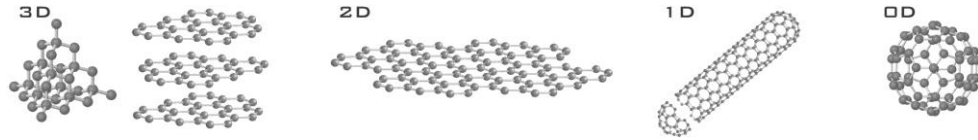


Figure 1-10 Crystal structures of the different allotropes of carbon. Three-dimensional diamond and graphite (3D); two-dimensional graphene (2D); one-dimensional nanotubes (1D); and zero-dimensional buckyballs (0D). (Adapted from [135]).

Carbon is an interesting element due to its capability to form variety of allotropes which are 3D diamond and graphite, 2D graphene, 1D carbon nanotubes, and 0D fullerenes [135].

As illustrated in Figure 1-10, plenty of carbon allotropes have been investigated by the research community, since they have shown a great amount of interest in many applications including sensory devices. A carbon atom can form various types of allotropes. In 3D structures, diamond and graphite are the allotropes of carbon. Carbon also forms low-dimensional (2D, 1D or 0D) allotropes collectively known as carbon nanomaterials. Examples of such nanomaterials are 1D carbon nanotubes (CNTs) and 0D fullerenes [135]. The electron configuration of carbon goes as  $1s^2$ ,  $2s^2$  and  $2p^2$ , respectively. The four valence electrons take part in the chemical bonds, whereas the hybridization provides the capability of single, double and triple bonds. Due to the small energy difference between the 2s and 2p ( $2p_x$ ,  $2p_y$  and  $2p_z$ ) orbitals, their wave functions could generate novel orbitals in the form of  $sp$ ,  $sp^2$  or  $sp^3$ , depending on the number of p atomic orbitals participating in the mixing with the s atomic orbital [136]. For example, in the list of carbon nanomaterials, graphene is known as 2D single layer form of graphite. It is famously known for its interleaving  $sp^2$  bonds (trigonal planar at  $120^\circ$ ) within the hexagonal lattice, since they are stronger than the  $sp^3$  bonds of diamond (tetrahedral at  $109.5^\circ$ ), thus highlighting graphene as a very strong material. Last but not least, graphene has been used for many years due to its remarkable behavior regarding the mechanical and electrical properties, and has been actively investigated also in sensory device applications [105]-[110].

Nowadays, graphene-based communities are mainly focused on the synthesis of high-quality nanoscale materials for large-scale production, since it is still remaining one of the biggest technological challenges. Focusing on extraordinary materials, processability played a significant role in the fabrication of graphene. Moreover, nanotechnology emerged to develop plenty of solutions for graphene implementation by using sophisticated technological processes in order to achieve inexpensive and low power devices, and later on to propose its effectiveness as an alternative to silicon-based technology that involves graphene-rigorous, and therefore adaptive micro-electronic strategies [137].

To approach the synthesis of state-of-the-art carbon based nano-composites, scientists and engineers have categorized two following groups, the “Top - Down” and the “Bottom - Up”. Each group is related to the scale and the processing method of the graphene-based material. The “Bottom - Up” approach consists of a molecular carbon precursor that is mainly used in standard

deposition techniques, such as CVD and epitaxial method [137]. On the other hand, the “Top - Down” approach covers the downsized materials from large-scale into nanometer-scale structures. There have been several synthesis methods for the “Top - Down” perspective, such as thermal, chemical exfoliation, sonication and functionalization [137]. Regarding the sensing application materials, the atomic size, shape, stability and the composition of graphene-based materials can be tailored by using the “Top - Down” strategy, especially due to its large-scale fabrication advantages. A top-down approach necessitates a feasible process development in the field of micro-sensory devices, since the addition of graphene-based materials arises to provide solutions into the ‘classical’ needs of sensitivity and selectivity as device features [137]. As illustrated in Figure 1-11, graphene is mostly obtained from graphite on a relatively large scale through oxidation - exfoliation - reduction, thus resulting the form of graphene oxide (GO).

As a matter of fact, the following technological trends show clearly that a variety of graphene based nano-materials is of the utmost importance since their functional characteristics, such as adsorption kinetics of graphene (high surface to volume ratio) and absorption kinetics of CNTs (high aspect ratio) are often related to the different tree selection of the process development (Figure 1-11). Thus, to provide alternative solutions in major technological issues, a particular route has to be validated, and therefore selected according to the application advantages in electronic, mechanical, thermal or optical properties, respectively.

For example, the GO structure contains plenty of oxygen-functional groups such as hydroxides and epoxides on the basal plane and carbonyl and carboxyl groups on the edge of the graphene structure. In general, the oxidation process, as well as the GO reduction method, could generate several defective sites on the graphene which offer numerous advantages regarding the gas sensing applications. Therefore, there is a great interest to exploit graphene as a sensing layer for SAW sensor devices. The employed graphene/SAW devices provided a better understanding in the graphene sensing mechanisms towards several greenhouse gases, however there are a number of questions that still remain to be answered.

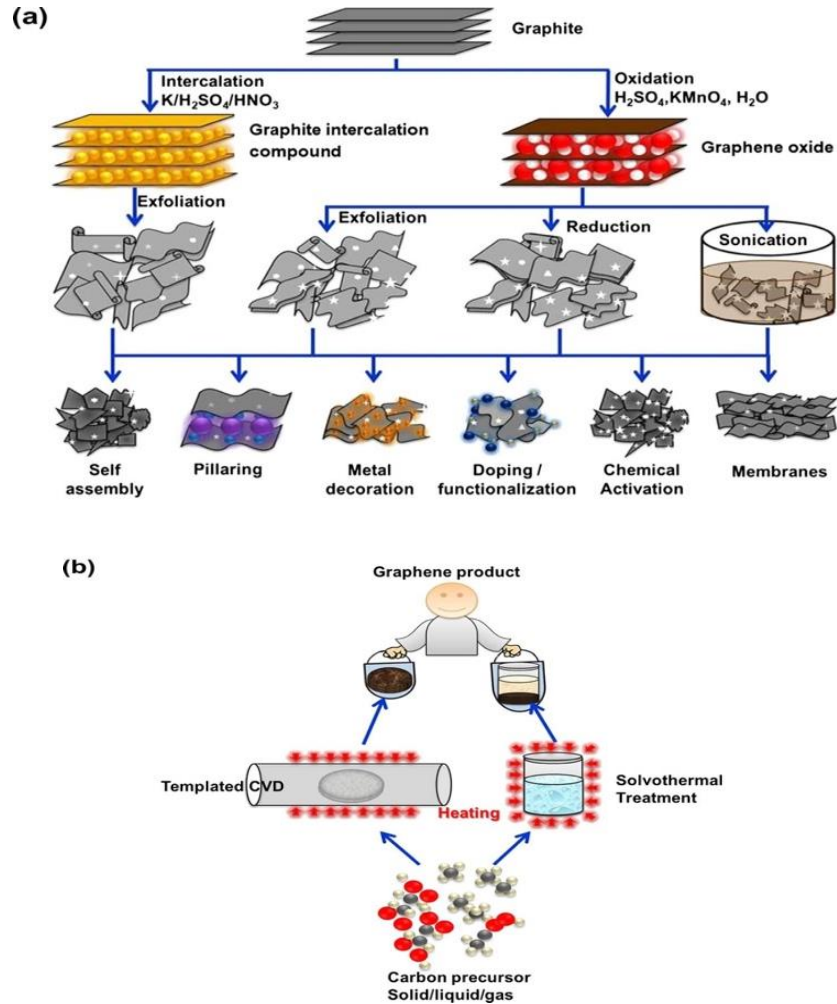


Figure 1-11 (a) Graphitic top-down approach and (b) molecular carbon precursor bottom-up approach for producing a wide variety of carbon-based allotropes in large quantities [90].

### 1.3 Conclusion

The aim of this PhD project was to develop a novel, stable, highly sensitive gas and humidity micro-sensors. In general, many requirements of the sensory devices were fulfilled since the prototype devices were exposed directly to the toxic environment, thus studying the interaction of sensing layers with the target analytes. This means that the sensor was also exposed to corrosive or contamination species, which can deteriorate and interfere with the performance of the sensing material. Great efforts have been made to investigate the important aspects of the Love wave sensors; sensitivity, selectivity, stability and reproducibility. To meet these demands, we have used a very well-known Love wave platform from previous research programs in order to acquire certainty of the novel sensors towards gas sensing applications. Many experiments were conducted, especially based on standard chemical engineering principles and specific characterization methods, as it will be extensively discussed later on the next chapters. This work includes the efforts to enhance the performance of traditional micro-electronic acoustic wave devices by using functionalized nano-composites. Recent advances in graphene technologies have

provided the opportunity to obtain high performances towards gas sensing applications compared to polycrystalline-based gas sensors. The selection of graphene as a unique material in the state-of-the-art literature allows a lot of novel synthetic nano-structured materials to target very high surface to volume ratio to interact with gas species. Thus, tailoring the size and the length of the graphene-based nano-structure materials through pre- and post- deposition methods, we have observed superior physical and chemical properties that are of great interest for sensor applications. In addition, electro-mechanical properties of the graphene nano-structure materials have shown that the devices can be further tuned in comparison to the bulk form of the same material, as well as they have opened new ways and questions for the Love-wave graphene based project, thus providing an excellent opportunity to build broad consensus on such practical aspects towards commercialized graphene-sensory devices.

## References or Bibliography (if any)

- [1] G. A. Ayoko and H. Wang, "Volatile Organic Compounds in Indoor Environments," in *Indoor Air Pollution*, Springer, Berlin, Heidelberg, 2014, pp. 69–107.
- [2] M. J. Mendell, "Indoor residential chemical emissions as risk factors for respiratory and allergic effects in children: a review," *Indoor Air*, vol. 17, no. 4, pp. 259–277, Aug. 2007.
- [3] Y. Wang, M. M. Tong, D. Zhang, and Z. Gao, "Improving the Performance of Catalytic Combustion Type Methane Gas Sensors Using Nanostructure Elements Doped with Rare Earth Cocatalysts," *Sensors*, vol. 11, no. 1, pp. 19–31, Dec. 2010.
- [4] D. J. Wales *et al.*, "Gas sensing using porous materials for automotive applications," *Chem. Soc. Rev.*, vol. 44, no. 13, pp. 4290–4321, 2015.
- [5] R. Moos *et al.*, "Selective ammonia exhaust gas sensor for automotive applications," *Sens. Actuators B Chem.*, vol. 83, no. 1, pp. 181–189, Mar. 2002.
- [6] E. R. Thaler and C. W. Hanson, "Medical applications of electronic nose technology," *Expert Rev. Med. Devices*, vol. 2, no. 5, pp. 559–566, Sep. 2005.
- [7] J. W. Gardner, H. W. Shin, and E. L. Hines, "An electronic nose system to diagnose illness," *Sens. Actuators B Chem.*, vol. 70, no. 1, pp. 19–24, Nov. 2000.
- [8] A. P. Jones, "Indoor air quality and health," *Atmos. Environ.*, vol. 33, no. 28, pp. 4535–4564, Dec. 1999.
- [9] T. Salthammer, "Release of Organic Compounds and Particulate Matter from Products, Materials, and Electrical Devices in the Indoor Environment," in *Indoor Air Pollution*, Springer, Berlin, Heidelberg, 2014, pp. 1–35.
- [10] D. Stipanicev and J. Marasovic, "Networked embedded greenhouse monitoring and control," in *Proceedings of 2003 IEEE Conference on Control Applications, 2003. CCA 2003.*, 2003, vol. 2, pp. 1350–1355 vol.2.
- [11] "WHO | WHO Global Urban Ambient Air Pollution Database (update 2016)," *WHO*. [Online]. Available: [http://www.who.int/phe/health\\_topics/outdoorair/databases/cities/en/](http://www.who.int/phe/health_topics/outdoorair/databases/cities/en/).
- [12] B. R. Gurjar, T. M. Butler, M. G. Lawrence, and J. Lelieveld, "Evaluation of emissions and air quality in megacities," *Atmos. Environ.*, vol. 42, no. 7, pp. 1593–1606, Mar. 2008.
- [13] J. M. Daisey, W. J. Angell, and M. G. Apte, "Indoor air quality, ventilation and health symptoms in schools: an analysis of existing information," *Indoor Air*, vol. 13, no. 1, pp. 53–64, Mar. 2003.
- [14] Z. Chen and C. Lu, "Humidity sensors: a review of materials and mechanisms," *Sens. Lett.*, vol. 3, no. 4, pp. 274–295, 2005.
- [15] A. V. Arundel, E. M. Sterling, J. H. Biggin, and T. D. Sterling, "Indirect health effects of relative humidity in indoor environments.," *Environ. Health Perspect.*, vol. 65, pp. 351–361, Mar. 1986.
- [16] W. H. Organization, "The public health impact of chemicals: knowns and unknowns," *World Health Organization*, pp. 13, (2016) [Online]. Available: <http://www.who.int/iris/handle/10665/206553>.
- [17] "Climate Change: Vital Signs of the Planet: Causes." [Online]. Available: <https://climate.nasa.gov/causes/>.
- [18] "WHO | Ambient air pollution: Health impacts," *WHO*. [Online]. Available: <http://www.who.int/airpollution/ambient/health-impacts/en/>.
- [19] A. A. Konnov, "The effect of temperature on the adiabatic laminar burning velocities of CH<sub>4</sub>-air and H<sub>2</sub>-air flames," *Fuel*, vol. 89, no. 9, pp. 2211–2216, Sep. 2010.



- [20] N. Abatzoglou and S. Boivin, "A review of biogas purification processes," *Biofuels Bioprod. Biorefining*, vol. 3, no. 1, pp. 42–71, Jan. 2009.
- [21] F. Biasioli, F. Gasperi, C. Yeretzi, and T. D. Märk, "PTR-MS monitoring of VOCs and BVOCs in food science and technology," *TrAC Trends Anal. Chem.*, vol. 30, no. 7, pp. 968–977, Jul. 2011.
- [22] G. Eranna, B. C. Joshi, D. P. Runthala, and R. P. Gupta, "Oxide Materials for Development of Integrated Gas Sensors—A Comprehensive Review," *Crit. Rev. Solid State Mater. Sci.*, vol. 29, no. 3–4, pp. 111–188, Jul. 2004.
- [23] K. Arshak, E. Moore, G. M. Lyons, J. Harris, and S. Clifford, "A review of gas sensors employed in electronic nose applications," *Sens. Rev.*, vol. 24, no. 2, pp. 181–198, Jun. 2004.
- [24] J. Janata, "Chemical sensors," *Anal. Chem.*, vol. 62, no. 12, pp. 33–44, Jun. 1990.
- [25] S. S. Schiffman and T. C. Pearce, "Introduction to Olfaction: Perception, Anatomy, Physiology, and Molecular Biology," in *Handbook of Machine Olfaction*, T. C. Pearce, S. S. Schiffman, H. T. Nagle, and J. W. Gardner, Eds. Wiley-VCH Verlag GmbH & Co. KGaA, 2002, pp. 1–31.
- [26] F. Zee and J. W. Judy, "Micromachined polymer-based chemical gas sensor array," *Sens. Actuators B Chem.*, vol. 72, no. 2, pp. 120–128, Jan. 2001.
- [27] G. Yang, C. Lee, J. Kim, F. Ren, and S. J. Pearton, "Flexible graphene-based chemical sensors on paper substrates," *Phys. Chem. Chem. Phys.*, vol. 15, no. 6, pp. 1798–1801, Jan. 2013.
- [28] A. Kaushik, R. Kumar, R. D. Jayant, and M. Nair, "Nanostructured Gas Sensors for Health Care: An Overview," *J. Pers. Nanomedicine*, vol. 1, no. 1, pp. 10–23, Jul. 2015.
- [29] Z. Yunusa, M. N. Hamidon, A. Kaiser, and Z. Awang, "Gas sensors: A review," *Sens. Transducers*, vol. 168, no. 4, pp. 61–75, 2014.
- [30] T. Wang *et al.*, "A Review on Graphene-Based Gas/Vapor Sensors with Unique Properties and Potential Applications," *Nano-Micro Lett.*, vol. 8, no. 2, pp. 95–119, Apr. 2016.
- [31] M. S. Nieuwenhuizen, A. W. Barendsz, E. Nieuwkoop, M. J. Vellekoop, and A. Venema, "Transduction mechanisms in SAW gas sensors," *Electron. Lett.*, vol. 22, no. 4, pp. 184–185, Feb. 1986.
- [32] G. Sberveglieri, *Gas Sensors: Principles, Operation and Developments*. Springer Science & Business Media, 2012.
- [33] S. Bender, F. L. Dickert, W. Mokwa, and P. Pachatz, "Investigations on temperature controlled monolithic integrated surface acoustic wave (SAW) gas sensors," *Sens. Actuators B Chem.*, vol. 93, no. 1, pp. 164–168, Aug. 2003.
- [34] M. Penza, F. Antolini, and M. V. Antisari, "Carbon nanotubes as SAW chemical sensors materials," *Sens. Actuators B Chem.*, vol. 100, no. 1, pp. 47–59, Jun. 2004.
- [35] C. Zimmermann, D. Rebière, C. Déjous, J. Pistré, E. Chastaing, and R. Planade, "A love-wave gas sensor coated with functionalized polysiloxane for sensing organophosphorus compounds," *Sens. Actuators B Chem.*, vol. 76, no. 1, pp. 86–94, Jun. 2001.
- [36] T. M. A. Gronewold, S. Glass, E. Quandt, and M. Famulok, "Monitoring complex formation in the blood-coagulation cascade using aptamer-coated SAW sensors," *Biosens. Bioelectron.*, vol. 20, no. 10, pp. 2044–2052, Apr. 2005.
- [37] S. Datta, *Surface acoustic wave devices*. Englewood Cliffs, N.J.: Prentice-Hall, 1986.
- [38] D. P. Morgan, "History of SAW devices," in *Proceedings of the 1998 IEEE International Frequency Control Symposium (Cat. No.98CH36165)*, 1998, pp. 439–460.
- [39] W. P. Mason, "Electromechanical Transducers and Wave Filters, New Your, D," *Van Nostrand*, 1942.

- [40] D. Damjanovic, "Materials for high temperature piezoelectric transducers," *Curr. Opin. Solid State Mater. Sci.*, vol. 3, no. 5, pp. 469–473, Oct. 1998.
- [41] M.-I. Rocha-Gaso, C. March-Iborra, Á. Montoya-Baides, and A. Arnau-Vives, "Surface Generated Acoustic Wave Biosensors for the Detection of Pathogens: A Review," *Sensors*, vol. 9, no. 7, pp. 5740–5769, Jul. 2009.
- [42] K. Länge, B. E. Rapp, and M. Rapp, "Surface acoustic wave biosensors: a review," *Anal. Bioanal. Chem.*, vol. 391, no. 5, pp. 1509–1519, Jul. 2008.
- [43] T.-Y. Lin, C.-H. Hu, and T.-C. Chou, "Determination of albumin concentration by MIP-QCM sensor," *Biosens. Bioelectron.*, vol. 20, no. 1, pp. 75–81, Jul. 2004.
- [44] R. Gabl *et al.*, "Novel integrated FBAR sensors: a universal technology platform for bio- and gas-detection," in *Proceedings of IEEE Sensors 2003 (IEEE Cat. No.03CH37498)*, 2003, vol. 2, pp. 1184–1188 Vol.2.
- [45] G. Sehra, M. Cole, and J. W. Gardner, "Miniature taste sensing system based on dual SH-SAW sensor device: an electronic tongue," *Sens. Actuators B Chem.*, vol. 103, no. 1, pp. 233–239, Sep. 2004.
- [46] R. L. Baer, C. A. Flory, M. Tom-Moy, and D. Solomon, "STW chemical sensors," in *IEEE 1992 Ultrasonics Symposium Proceedings*, 1992, pp. 293–298 vol.1.
- [47] G. Kovacs, M. J. Vellekoop, R. Hauéis, G. W. Lubking, and A. Venema, "A love wave sensor for (bio)chemical sensing in liquids," *Sens. Actuators Phys.*, vol. 43, no. 1, pp. 38–43, May 1994.
- [48] S. J. Martin, A. J. Ricco, T. M. Niemczyk, and G. C. Frye, "Characterization of SH acoustic plate mode liquid sensors," *Sens. Actuators*, vol. 20, no. 3, pp. 253–268, Dec. 1989.
- [49] W. Y. Chang, P. H. Sung, C. H. Chu, C. J. Shih, and Y. C. Lin, "Phase Detection of the Two-Port FPW Sensor for Biosensing," *IEEE Sens. J.*, vol. 8, no. 5, pp. 501–507, May 2008.
- [50] Tokimatsu Kohji, Tamura Shuji, and Kojima Hisaya, "Effects of Multiple Modes on Rayleigh Wave Dispersion Characteristics," *J. Geotech. Eng.*, vol. 118, no. 10, pp. 1529–1543, Oct. 1992.
- [51] C. Zhang, J. J. Caron, and J. F. Vetelino, "The Bleustein–Gulyaev wave for liquid sensing applications," *Sens. Actuators B Chem.*, vol. 76, no. 1, pp. 64–68, Jun. 2001.
- [52] D. S. B. Jr *et al.*, *Acoustic Wave Sensors: Theory, Design and Physico-Chemical Applications*. Elsevier, 1996.
- [53] A. E. H. Love, *A Treatise on the Mathematical Theory of Elasticity*. Cambridge University Press, 2013.
- [54] Z. Su, L. Ye, and Y. Lu, "Guided Lamb waves for identification of damage in composite structures: A review," *J. Sound Vib.*, vol. 295, no. 3, pp. 753–780, Aug. 2006.
- [55] S. Krishnamurthy, "Wireless Passive Surface Acoustic Wave (SAW) Sensing System," *Dissertations*, Aug. 2007.
- [56] H. Campanella *et al.*, "Localized-mass detection based on thin-film bulk acoustic wave resonators (FBAR): Area and mass location aspects," *Sens. Actuators Phys.*, vol. 142, no. 1, pp. 322–328, Mar. 2008.
- [57] X. L. He *et al.*, "Film bulk acoustic resonator pressure sensor with self temperature reference," *J. Micromechanics Microengineering*, vol. 22, no. 12, p. 125005, 2012.
- [58] L. García-Gancedo *et al.*, "Dual-mode thin film bulk acoustic wave resonators for parallel sensing of temperature and mass loading," *Biosens. Bioelectron.*, vol. 38, no. 1, pp. 369–374, Oct. 2012.
- [59] P. Jin, S. Dong, H. Jin, and M. Wu, "Processing Chip for Thin Film Bulk Acoustic Resonator Mass Sensor," *J Control Sci Eng*, vol. 2012, pp. 7:7–7:7, Jan. 2012.

- [60] Y. Q. Fu *et al.*, “Advances in piezoelectric thin films for acoustic biosensors, acoustofluidics and lab-on-chip applications,” *Prog. Mater. Sci.*, vol. 89, pp. 31–91, Aug. 2017.
- [61] K. Aki, “Study of earthquake mechanism by a method of phase equalization applied to Rayleigh and Love waves,” *J. Geophys. Res.*, vol. 65, no. 2, pp. 729–740, Feb. 1960.
- [62] Lord Rayleigh, “On Waves Propagated along the Plane Surface of an Elastic Solid,” *Proc. Lond. Math. Soc.*, vol. s1-17, no. 1, pp. 4–11, Nov. 1885.
- [63] K. D. Souza, G. P. Lees, P. C. Wait, and T. P. Newson, “Diode-pumped Landau-Placzek based distributed temperature sensor utilising an all-fibre Mach-Zehnder interferometer,” *Electron. Lett.*, vol. 32, no. 23, pp. 2174–2175, Nov. 1996.
- [64] D. W. Burns, J. D. Zook, R. D. Horning, W. R. Herb, and H. Guckel, “Sealed-cavity resonant microbeam pressure sensor,” *Sens. Actuators Phys.*, vol. 48, no. 3, pp. 179–186, May 1995.
- [65] J. Devkota, P. R. Ohodnicki, and D. W. Greve, “SAW Sensors for Chemical Vapors and Gases., SAW Sensors for Chemical Vapors and Gases,” *Sens. Basel Switz. Sens. Basel Switz.*, vol. 17, no. 4, Apr. 2017.
- [66] B. Drafts, “Acoustic wave technology sensors,” *IEEE Trans. Microw. Theory Tech.*, vol. 49, no. 4, pp. 795–802, Apr. 2001.
- [67] P. Kiełczyński, M. Szalewski, R. M. Siegoczyński, and A. J. Rostocki, “New ultrasonic Bleustein-Gulyaev wave method for measuring the viscosity of liquids at high pressure,” *Rev. Sci. Instrum.*, vol. 79, no. 2, p. 026109, Feb. 2008.
- [68] F. Martin, M. I. Newton, G. McHale, K. A. Melzak, and E. Gizeli, “Pulse mode shear horizontal-surface acoustic wave (SH-SAW) system for liquid based sensing applications,” *Biosens. Bioelectron.*, vol. 19, no. 6, pp. 627–632, Jan. 2004.
- [69] B. A. Auld, *Acoustic fields and waves in solids*. Рипол Классик, 1973.
- [70] T. Nomura, A. Saitoh, and Y. Horikoshi, “Measurement of acoustic properties of liquid using liquid flow SH-SAW sensor system,” *Sens. Actuators B Chem.*, vol. 76, no. 1, pp. 69–73, Jun. 2001.
- [71] R. L. Baer and C. Flory, “Chemical sensor utilizing a surface transverse wave device,” 5283037, 01-Feb-1994.
- [72] I. D. Avramov, “Microwave oscillators stabilized with surface transverse wave resonant devices,” in *Proceedings of the 1992 IEEE Frequency Control Symposium*, 1992, pp. 391–408.
- [73] V. Raimbault, D. Rebière, and C. Dejous, “A microfluidic surface acoustic wave sensor platform: Application to high viscosity measurements,” *Mater. Sci. Eng. C*, vol. 28, no. 5, pp. 759–764, Jul. 2008.
- [74] C. Zimmermann, *Conception, réalisation et étude de micro-capteurs à ondes de Love pour applications en milieu gazeux: Cas de la détection de composés organophosphorés*. Bordeaux 1, 2002.
- [75] V. Raimbault, *Etude et développement d’un système microfluide à ondes de Love dédié à la caractérisation de fluides complexes*. Bordeaux 1, 2008.
- [76] O. Tamarin *et al.*, “Study of acoustic Love wave devices for real time bacteriophage detection,” *Sens. Actuators B Chem.*, vol. 91, no. 1, pp. 275–284, Jun. 2003.
- [77] E. Gizeli, A. C. Stevenson, N. J. Goddard, and C. R. Lowe, “A novel Love-plate acoustic sensor utilizing polymer overlayers,” *IEEE Trans. Ultrason. Ferroelectr. Freq. Control*, vol. 39, no. 5, pp. 657–659, Sep. 1992.

- [78] M. D. Schlensog, T. M. A. Gronewold, M. Tewes, M. Famulok, and E. Quandt, "A Love-wave biosensor using nucleic acids as ligands," *Sens. Actuators B Chem.*, vol. 101, no. 3, pp. 308–315, Jul. 2004.
- [79] Y. Q. Fu *et al.*, "Recent developments on ZnO films for acoustic wave based bio-sensing and microfluidic applications: a review," *Sens. Actuators B Chem.*, vol. 143, no. 2, pp. 606–619, Jan. 2010.
- [80] K. Mitsakakis, A. Tserepi, and E. Gizeli, "Integration of Microfluidics With a Love Wave Sensor for the Fabrication of a Multisample Analytical Microdevice," *J. Microelectromechanical Syst.*, vol. 17, no. 4, pp. 1010–1019, Aug. 2008.
- [81] D. W. Branch and S. M. Brozik, "Low-level detection of a Bacillus anthracis simulant using Love-wave biosensors on 36°YX LiTaO<sub>3</sub>," *Biosens. Bioelectron.*, vol. 19, no. 8, pp. 849–859, Mar. 2004.
- [82] M. J. Vellekoop, "Acoustic wave sensors and their technology," *Ultrasonics*, vol. 36, no. 1, pp. 7–14, Feb. 1998.
- [83] B. Jakoby, G. M. Ismail, M. P. Byfield, and M. J. Vellekoop, "A novel molecularly imprinted thin film applied to a Love wave gas sensor," *Sens. Actuators Phys.*, vol. 76, no. 1, pp. 93–97, Aug. 1999.
- [84] B. Jakoby and M. J. Vellekoop, "Viscosity sensing using a Love-wave device," *Sens. Actuators Phys.*, vol. 68, no. 1, pp. 275–281, Jun. 1998.
- [85] J. Du, G. L. Harding, J. A. Ogilvy, P. R. Dencher, and M. Lake, "A study of Love-wave acoustic sensors," *Sens. Actuators Phys.*, vol. 56, no. 3, pp. 211–219, Sep. 1996.
- [86] R.-C. Chang, S.-Y. Chu, C.-S. Hong, and Y.-T. Chuang, "A study of Love wave devices in ZnO/Quartz and ZnO/LiTaO<sub>3</sub> structures," *Thin Solid Films*, vol. 498, no. 1, pp. 146–151, Mar. 2006.
- [87] J. Du, G. L. Harding, A. F. Collings, and P. R. Dencher, "An experimental study of Love-wave acoustic sensors operating in liquids," *Sens. Actuators Phys.*, vol. 60, no. 1, pp. 54–61, May 1997.
- [88] I. Nikolaou *et al.*, "Novel SAW gas sensor based on graphene," in *2015 30th Symposium on Microelectronics Technology and Devices (SBMicro)*, 2015, pp. 1–4.
- [89] I. Nikolaou *et al.*, "Drop-casted Graphene Oxide Love Wave sensor for detection of humidity and VOCs," *J. Integr. Circuits Syst.*, vol. 11, no. 1, pp. 49–56, Apr. 2016.
- [90] I. Nikolaou *et al.*, "Electro-mechanical properties of inkjet-printed graphene oxide nanosheets," *Phys. Status Solidi A*, vol. 214, no. 3, 1600492, Mar. 2017.
- [91] I. Nikolaou, H. Hallil, O. Tamarin, C. Dejous, and D. Rebière, "A three-dimensional model for a graphene guided SH-SAW sensor using finite element method," in *2016 31st Symposium on Microelectronics Technology and Devices (SBMicro)*, 2016, pp. 1–4.
- [92] I. Nikolaou, H. Hallil, V. Conédéra, G. Deligeorgis, C. Dejous, and D. Rebière, "Inkjet-Printed Graphene Oxide Thin Layers on Love Wave Devices for Humidity and Vapor Detection," *IEEE Sens. J.*, vol. 16, no. 21, pp. 7620–7627, Nov. 2016.
- [93] I. Esteban, "Etude et intégration de capteurs acoustiques à modes de plaque transverses horizontaux (SH-APM): application à la détection de gaz organophosphorés," thesis, Bordeaux 1, 1999.
- [94] P. Luginbuhl *et al.*, "Microfabricated Lamb wave device based on PZT sol-gel thin film for mechanical transport of solid particles and liquids," *J. Microelectromechanical Syst.*, vol. 6, no. 4, pp. 337–346, Dec. 1997.
- [95] A. K. Pantazis, G. Konstantinidis, and E. Gizeli, "Study of the Effect of the Operating Frequency of a GaN Lamb Wave Device to Viscosity and Protein Sensing," *IEEE Sens. J.*, vol. 16, no. 19, pp. 7028–7036, Oct. 2016.

- [96] W. Xuan *et al.*, “High sensitivity flexible Lamb-wave humidity sensors with a graphene oxide sensing layer,” *Nanoscale*, vol. 7, no. 16, pp. 7430–7436, 2015.
- [97] M. Vieno *et al.*, “Corrigendum: The UK particulate matter air pollution episode of March–April 2014: more than Saharan dust (2016 *Environ. Res. Lett.* 11 [http://dx.doi.org/10.1088/1748-9326/11/4/044004] 044004 ),” *Environ. Res. Lett.*, vol. 11, no. 5, p. 059501, 2016.
- [98] A. Afzal, N. Iqbal, A. Mujahid, and R. Schirhagl, “Advanced vapor recognition materials for selective and fast responsive surface acoustic wave sensors: A review,” *Anal. Chim. Acta*, vol. 787, pp. 36–49, Jul. 2013.
- [99] S. J. Ippolito *et al.*, “Layered WO<sub>3</sub>/ZnO/36° LiTaO<sub>3</sub> SAW gas sensor sensitive towards ethanol vapour and humidity,” *Sens. Actuators B Chem.*, vol. 117, no. 2, pp. 442–450, Oct. 2006.
- [100] J. A. Thiele and M. P. da Cunha, “Dual configuration high temperature hydrogen sensor on LGS SAW devices,” in *IEEE Ultrasonics Symposium, 2004*, 2004, vol. 2, pp. 809–812 Vol.2.
- [101] C. Lim, W. Wang, S. Yang, and K. Lee, “Development of SAW-based multi-gas sensor for simultaneous detection of CO<sub>2</sub> and NO<sub>2</sub>,” *Sens. Actuators B Chem.*, vol. 154, no. 1, pp. 9–16, May 2011.
- [102] D.-T. Phan and G.-S. Chung, “Surface acoustic wave hydrogen sensors based on ZnO nanoparticles incorporated with a Pt catalyst,” *Sens. Actuators B Chem.*, vol. 161, no. 1, pp. 341–348, Jan. 2012.
- [103] C. Wang, Y. Wang, S. Zhang, L. Fan, and X. Shui, “Characteristics of SAW hydrogen sensors based on InOx/128°YX-LiNbO<sub>3</sub> structures at room temperature,” *Sens. Actuators B Chem.*, vol. 173, pp. 710–715, Oct. 2012.
- [104] V. B. Raj, H. Singh, A. T. Nimal, M. Tomar, M. U. Sharma, and V. Gupta, “Effect of metal oxide sensing layers on the distinct detection of ammonia using surface acoustic wave (SAW) sensors,” *Sens. Actuators B Chem.*, vol. 187, pp. 563–573, Oct. 2013.
- [105] R. Arsat *et al.*, “Graphene-like nano-sheets for surface acoustic wave gas sensor applications,” *Chem. Phys. Lett.*, vol. 467, no. 4, pp. 344–347, Jan. 2009.
- [106] W. Xuan *et al.*, “Fast Response and High Sensitivity ZnO/glass Surface Acoustic Wave Humidity Sensors Using Graphene Oxide Sensing Layer,” *Sci. Rep.*, vol. 4, p. 7206, Nov. 2014.
- [107] L. Sheng, C. Dajing, and C. Yuquan, “A surface acoustic wave humidity sensor with high sensitivity based on electrospun MWCNT/Nafion nanofiber films,” *Nanotechnology*, vol. 22, no. 26, p. 265504, 2011.
- [108] B. Wang, L. Zheng, and L. Zhou, “Surface acoustic wave sensors with Graphene/PANI nanocomposites for nitric oxide detection,” *IOP Conf. Ser. Earth Environ. Sci.*, vol. 100, no. 1, p. 012044, 2017.
- [109] S. Thomas *et al.*, “Graphene-coated Rayleigh SAW Resonators for NO<sub>2</sub> Detection,” *Procedia Eng.*, vol. 87, pp. 999–1002, Jan. 2014.
- [110] S. Xu, C. Li, H. Li, M. Li, C. Qu, and B. Yang, “Carbon dioxide sensors based on a surface acoustic wave device with a graphene–nickel–L-alanine multilayer film,” *J. Mater. Chem. C*, vol. 3, no. 16, pp. 3882–3890, Apr. 2015.
- [111] M. Penza, F. Antolini, and M. V. Antisari, “Carbon nanotubes as SAW chemical sensors materials,” *Sens. Actuators B Chem.*, vol. 100, no. 1, pp. 47–59, Jun. 2004.
- [112] H.-L. Hsu, J.-M. Jehng, Y. Sung, L.-C. Wang, and S.-R. Yang, “The synthesis, characterization of oxidized multi-walled carbon nanotubes, and application to surface

- acoustic wave quartz crystal gas sensor,” *Mater. Chem. Phys.*, vol. 109, no. 1, pp. 148–155, May 2008.
- [113] M. Penza, P. Aversa, G. Cassano, W. Wlodarski, and K. Kalantar-Zadeh, “Layered SAW gas sensor with single-walled carbon nanotube-based nanocomposite coating,” *Sens. Actuators B Chem.*, vol. 127, no. 1, pp. 168–178, Oct. 2007.
- [114] M. Asad and M. H. Sheikhi, “Surface acoustic wave based H<sub>2</sub>S gas sensors incorporating sensitive layers of single wall carbon nanotubes decorated with Cu nanoparticles,” *Sens. Actuators B Chem.*, vol. 198, pp. 134–141, Jul. 2014.
- [115] I. Sayago *et al.*, “New sensitive layers for surface acoustic wave gas sensors based on polymer and carbon nanotube composites,” *Sens. Actuators B Chem.*, vol. 175, pp. 67–72, Dec. 2012.
- [116] I. Sayago *et al.*, “Surface acoustic wave gas sensors based on polyisobutylene and carbon nanotube composites,” *Sens. Actuators B Chem.*, vol. 156, no. 1, pp. 1–5, Aug. 2011.
- [117] B. Serban *et al.*, “Surface acoustic wave CO<sub>2</sub> sensing with polymer-amino carbon nanotube composites,” in *2008 International Semiconductor Conference*, 2008, vol. 1, pp. 73–76.
- [118] M. C. Horrillo *et al.*, “Optimization of SAW sensors with a structure ZnO–SiO<sub>2</sub>–Si to detect volatile organic compounds,” *Sens. Actuators B Chem.*, vol. 118, no. 1, pp. 356–361, Oct. 2006.
- [119] M. J. Fernández *et al.*, “Discrimination of volatile compounds through an electronic nose based on ZnO SAW sensors,” *Sens. Actuators B Chem.*, vol. 127, no. 1, pp. 277–283, Oct. 2007.
- [120] X. Du, Z. Ying, Y. Jiang, Z. Liu, T. Yang, and G. Xie, “Synthesis and evaluation of a new polysiloxane as SAW sensor coatings for DMMP detection,” *Sens. Actuators B Chem.*, vol. 134, no. 2, pp. 409–413, Sep. 2008.
- [121] W. Wen, H. Shitang, L. Shunzhou, L. Minghua, and P. Yong, “Enhanced sensitivity of SAW gas sensor coated molecularly imprinted polymer incorporating high frequency stability oscillator,” *Sens. Actuators B Chem.*, vol. 125, no. 2, pp. 422–427, Aug. 2007.
- [122] F. Di Pietrantonio *et al.*, “Volatile toxic compound detection by surface acoustic wave sensor array coated with chemoselective polymers deposited by laser induced forward transfer: Application to sarin,” *Sens. Actuators B Chem.*, vol. 174, pp. 158–167, Nov. 2012.
- [123] P. A. Lieberzeit, C. Palfinger, F. L. Dickert, and G. Fischerauer, “SAW RFID-Tags for Mass-Sensitive Detection of Humidity and Vapors,” *Sensors*, vol. 9, no. 12, pp. 9805–9815, Dec. 2009.
- [124] P. A. Lieberzeit, W. Greibl, H. Stathopoulos, F. L. Dickert, G. Fischerauer, and W.-E. Bulst, “Covalently anchored supramolecular monolayers on quartz surfaces for use in SAW sensors,” *Sens. Actuators B Chem.*, vol. 113, no. 2, pp. 677–683, Feb. 2006.
- [125] X. Yang, S. Johnson, J. Shi, T. Holesinger, and B. Swanson, “Polyelectrolyte and molecular host ion self-assembly to multilayer thin films: An approach to thin film chemical sensors,” *Sens. Actuators B Chem.*, vol. 45, no. 2, pp. 87–92, Dec. 1997.
- [126] B.-Q. Cao, Q.-B. Huang, and Y. Pan, “Study on the Surface Acoustic Wave Sensor with Self-Assembly Imprinted Film of Calixarene Derivatives to Detect Organophosphorus Compounds,” *Am. J. Anal. Chem.*, vol. 03, no. 09, p. 664, Aug. 2012.
- [127] T. Nakamoto, K. Aoki, T. Ogi, S. Akao, and N. Nakaso, “Odor sensing system using ball SAW devices,” *Sens. Actuators B Chem.*, vol. 130, no. 1, pp. 386–390, Mar. 2008.
- [128] L. J. Kepley, R. M. Crooks, and A. J. Ricco, “A selective SAW-based organophosphonate chemical sensor employing a self-assembled, composite monolayer: a new paradigm for sensor design,” *Anal. Chem.*, vol. 64, no. 24, pp. 3191–3193, Dec. 1992.

- [129] C. Viespe and C. Grigoriu, "Surface acoustic wave sensors with carbon nanotubes and SiO<sub>2</sub>/Si nanoparticles based nanocomposites for VOC detection," *Sens. Actuators B Chem.*, vol. 147, no. 1, pp. 43–47, May 2010.
- [130] E. Chevallier, E. Scorsone, and P. Bergonzo, "Modified diamond nanoparticles as sensitive coatings for chemical SAW sensors," *Procedia Chem.*, vol. 1, no. 1, pp. 943–946, Sep. 2009.
- [131] A. Balcerzak, M. Aleksiejuk, G. Zhavnerko, and V. Agabekov, "Sensing properties of two-component Langmuir–Blodgett layer and its porous derivative in SAW sensor for vapors of methanol and ethanol," *Thin Solid Films*, vol. 518, no. 12, pp. 3402–3406, Apr. 2010.
- [132] I. Nicolae, C. Viespe, and C. Grigoriu, "Nanocomposite sensitive polymeric films for SAW sensors deposited by the MAPLE direct write technique," *Sens. Actuators B Chem.*, vol. 158, no. 1, pp. 418–422, Nov. 2011.
- [133] A. Z. Sadek, W. Wlodarski, K. Kalantar-zadeh, K. Shin, and R. B. Kaner, "A Room Temperature Polyaniline/In<sub>2</sub>O<sub>3</sub> Nanofiber Composite Based Layered ZnO/64° YX LiNbO<sub>3</sub> SAW Hydrogen Gas Sensor," in *2006 5th IEEE Conference on Sensors*, 2006, pp. 687–690.
- [134] A. Z. Sadek *et al.*, "A ZnO nanorod based layered ZnO/64° YX LiNbO<sub>3</sub> SAW hydrogen gas sensor," *Thin Solid Films*, vol. 515, no. 24, pp. 8705–8708, Oct. 2007.
- [135] M. I. Katsnelson, "Graphene: carbon in two dimensions," *Mater. Today*, vol. 10, no. 1, pp. 20–27, Jan. 2007.
- [136] M. Rai and S. Sarkar, "Carbon nanotube as a vlsi interconnect," in *Electronic Properties of Carbon Nanotubes*, InTech, 2011.
- [137] S. Gadipelli and Z. X. Guo, "Graphene-based materials: synthesis and gas sorption, storage and separation," *Prog. Mater. Sci.*, vol. 69, pp. 1–60, 2015.





## Chapter 2

# Sensors and Materials Integration

## II. Graphene Oxide sensing material integration in the acoustical platform

### II.1 Introduction

A fundamental objective in research and development of sensory devices is the aim to integrate top-down solid state technology with bottom-up nanofabricated materials, such as graphene and its derivatives, thus leading to functional devices that overlap in size at the nano- to micro- scale interactions [1], [2]. According to the literature, a variety of functional nanomaterials have been previously developed [3], and several processes are available for integrating nanomaterials of different compositions into functional devices [4]. In particular, chapter II analyzes the aspects of preparation and fabrication techniques to integrate the graphene material on Love wave platforms. Furthermore, it presents the experimental characterization methods (SEM, FEM, AFM and Raman Spectroscopies) used for the graphene oxide sensing layers. However, due to the initial demands of the preliminary study, especially on carbon materials integration process, a standard deposition method was selected (drop-casting). Since the developed methods of novel sensory devices are in need of reliable, reproductive and mass-production integration method, an inkjet-printing technique was selected later on, regarding the criteria and compromises of this research.

### II.2 Love wave platform fabrication

The devices were produced in collaboration with LAAS-CNRS, as part of the Renatech national network of Cleanroom facilities with IMS laboratory. Typically, 14 sensor devices are made simultaneously on a 4-inch quartz substrate. The Love wave sensors used in this work were designed in Céline's Zimmermann thesis [5]. This platform is based on two delay lines (Figure 2-1), consisting of two Love wave transducers, transmitter and receiver, respectively. The input transducer induces mechanical stresses (or elastic) in the piezoelectric substrate due to the inverse piezoelectric effect. The resultant strains propagate along the surface of the substrate away from the input transducer in the form of acoustic waves with respect to the particular "delay-line" configuration of the device, while the conversion of acoustic-to-electric energy by the output transducer provides an electrical signal (direct piezoelectric effect).

Each transducer is composed of 4 interdigitated electrode pairs and two contact pads (on Figure 2-1). The spatial periodicity of the electrodes (fingers),  $\lambda$ , is  $40\mu\text{m}$  in order to operate around 118MHz frequency. Figure 2-1 shows a representative example of a split finger, and therefore the width of an electrode corresponds to  $5\mu\text{m}$ , since the spacing between each electrode is  $\lambda/8=5\mu\text{m}$  with  $\lambda$  equaled to  $40\mu\text{m}$ , accordingly. The aperture,  $W$ , of the transducers is equal to 40 times  $\lambda = 1.6\text{ mm}$ . Moreover, the Center to Center distance of the IDTs or  $L_{cc}$  corresponds to  $209.125\lambda$ , ( $\lambda=40\mu\text{m}$ ). The acoustic wave velocity is found from the relation  $V = f_0\lambda$ , where equals to  $4720\text{ m/s}$  ( $40\mu\text{m}$  of the acoustic wavelength  $\lambda$  times the center frequency of 118 MHz).

Figure 2-1 shows the detailed process of a Love wave platform during its subsequent process development. Firstly, a quartz substrate (500  $\mu\text{m}$  – thickness) with an AT-cut crystallographic orientation (Euler angles:  $0^\circ$ ,  $121.5^\circ$ ,  $90^\circ$ ) was used to generate pure shear horizontal acoustic waves. As illustrated in Figure 2-1(a), the metallization of the IDTs was based on different metallic layers of [Ti (20 nm) + Au (100 nm) + Ti (20 nm) = 140 nm], which have been evaporated by using lift-off process towards good adhesion between the metallization and quartz. Then, the electrical contacts have been thickened with Ti (20 nm) + Au (90 nm) = 110 nm as shown in the Figure 2-1(b), respectively.

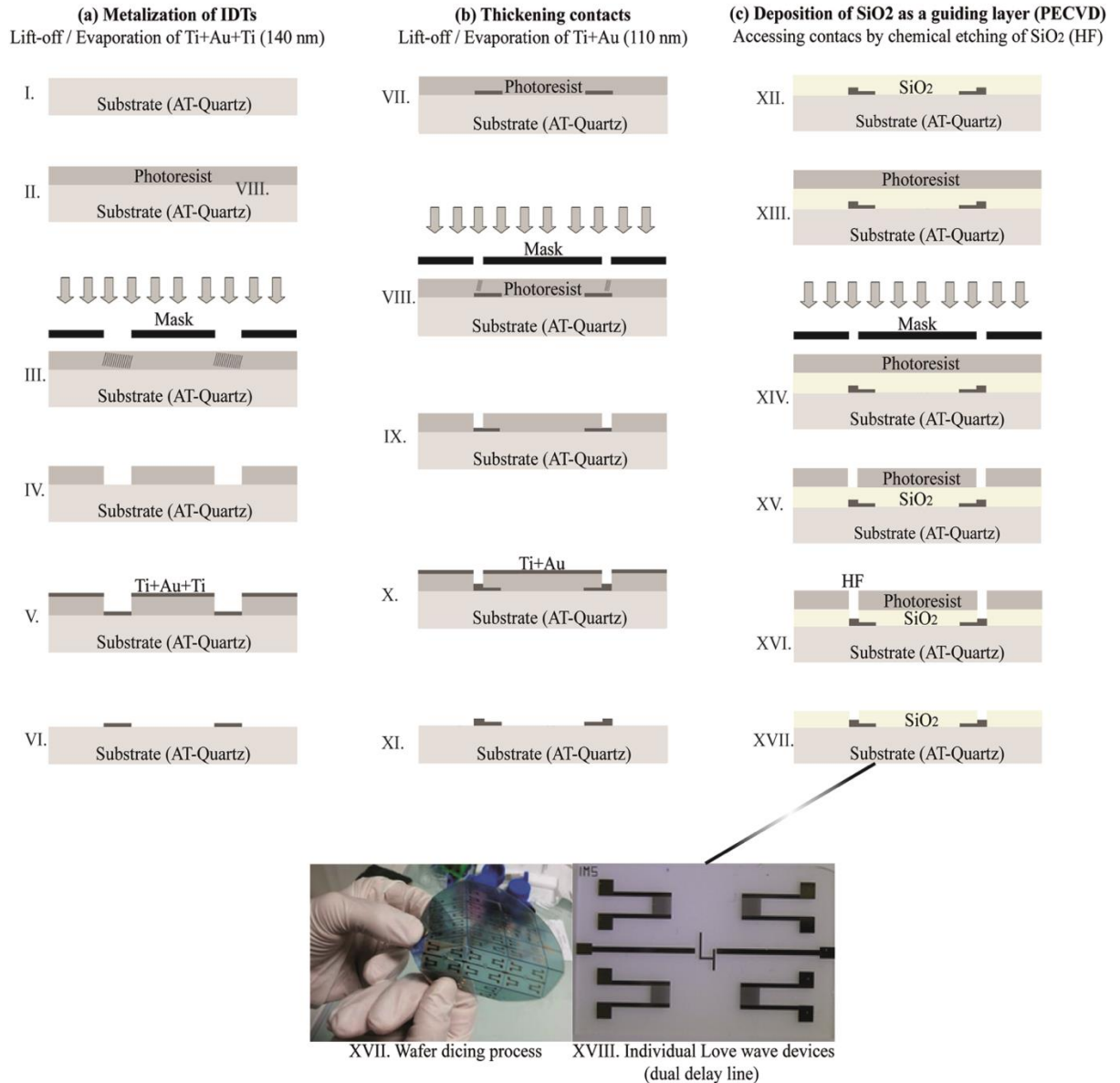


Figure 2-1 Technological process steps of Love wave devices.

As mentioned above, the IDTs are each composed of 44 split finger pairs with a  $40\mu\text{m}$  periodicity, corresponding to the wavelength. Figure 2-1(c) shows the next step of the fabrication procedure, which consists a  $4.1\ \mu\text{m}$  silicon dioxide (SiO<sub>2</sub>) film deposited by Plasma Enhanced Chemical Vapor Deposition (PECVD) as a guiding layer. The SiO<sub>2</sub> guiding layer allows to trap

the mechanical energy near the surface and therefore, to ensure the sensitivity due to the surface perturbations. The low temperature of the PECVD deposition (around 300 °C) was essential to maintain the piezoelectric characteristics of the quartz. Then, the silica was etched chemically, by following a new photolithography step, to clear the electrical contacts. Several generations of the Love wave devices have been fabricated previously, and plenty of improvements have been encapsulated within the fabrication process [5].

Following the fabrication process of the micro-devices, as represented in Figure 2-2, the addition of a chemical sensitive film was necessary to target different application areas based on innovative material compositions, such as graphene. As it will be discussed later, sophisticated graphene depositions were realized from the acoustic wave propagation path to an even further extent by enlarging the sensing surface, in order to enhance performances for different gas detection applications. Especially, for multi-gas sensory purposes, the functionalized graphene film permits to amplify the immobilization of the targeted gas molecules, and subsequently, enhances mass loading effect (sensitivity) of the Love wave coated devices.

## II.3 Preparation of graphene oxide solution and its Drop-Casting deposition

### II.3.1 Graphene Oxide solution preparation and its characterization

The Love wave platform reported in this thesis was mainly based on a dual ‘delay-line’ setup, especially over two different acoustic wave propagation paths. The first one corresponds to the coated delay line, and subsequently, the second one is related to the uncoated (bare) part of the sensor. Additionally, the Love wave platform has a double-action differential technique which allows the evaluation of novel sensing materials. This differential technique provides certainty, as well as clarity to different detections and target analytes, respectively. Figure 2-3 graphically depicts a representative graphene-based Love wave device and its potential application on vapor exposures.

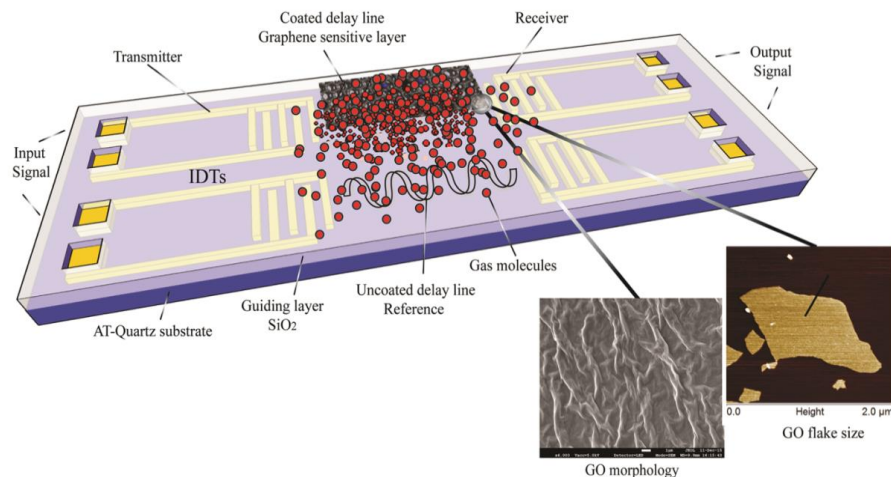


Figure 2-2 Visualization perspectives (3-D) of the final Graphene based Love wave device under vapor exposures.

The initial composition of the GO solution was prepared by Prof. Hermenegildo Garcia (ITQ Valencia) with whom Dr. George Deligeorgis had collaborated for the preliminary graphene coated Love wave devices. With his knowledge and expertise on chemical composites, the GO solution was enhanced dramatically and further used as the pivotal column in pursuing research within the graphene sensitive materials.

In 1958, Hummers [7] reported the method most commonly used today; the graphite is oxidized by treatment with  $\text{KMnO}_4$  and  $\text{NaNO}_3$  in concentrated  $\text{H}_2\text{SO}_4$ . The most common source of graphite used for chemical reactions, including its oxidation, is flake graphite, which is a naturally occurring mineral that is purified to remove heteroatomic contamination [8]. Graphene oxide (GO) prepared from flake graphite can be readily dispersed in water and has been used on a large scale for preparing large graphitic films, as a binder for carbon products. Moreover, the hydrophilicity of GO allows it to be uniformly deposited onto substrates in the form of thin films, which is necessary for applications in electronics [9].

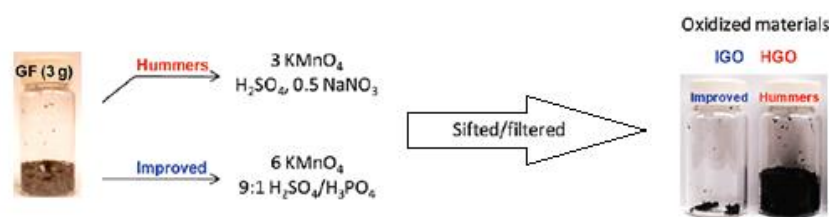


Figure 2-3 GO Preparation methods used starting with graphite flakes (GF) - Graphite oxidation and GO filtered suspensions [10].

The sample of GO used in the present study was obtained from commercial graphite by Hummers [7] oxidation followed by subsequent exfoliation of the resulting GO by sonication in water. Inks of permanent GO suspensions with concentration of  $1.2 \text{ mg} \times \text{ml}^{-1}$  were prepared. Analytically, a particular method (improved – Figure 2-3) has been utilized to produce high quality oxidized graphene, that is, a mixture of concentrated  $\text{H}_2\text{SO}_4/\text{H}_3\text{PO}_4$  (360:40 mL) was added to a mixture of graphite flakes (3g) and  $\text{KMnO}_4$  (18g) to produce an exothermic reaction that was controlled in an ice bath. Then, the mixture was heated to  $50 \text{ }^\circ\text{C}$  and stirred for 24 h, then cooled to room temperature (RT) and poured onto ice (400 mL) that contained 30%  $\text{H}_2\text{O}_2$  (3mL). The suspension was filtered, washed with aqueous  $\text{HCl}$  (1:10, 37%) and water and the resultant solid suspension was centrifuged and dried at  $60 \text{ }^\circ\text{C}$ . The GO suspensions were prepared by exfoliation of the GO solids by sonication in Milli-Q water for 2 h with an ultrasound source (400 W) to give aqueous suspensions of GO sheets with a concentration of  $500 \text{ mg L}^{-1}$ . Drying of these GO suspensions renders powdered black solids with a specific surface area of  $29 \text{ m}^2 \times \text{g}^{-1}$  which falls in the range of the reported values for these materials. Figure 2-4(a) shows Raman spectra for high oxidation of graphene sensitive coatings. Infrared (IR) spectroscopy of these GO powders is presented in the Figure 2-4(b) below, wherein the characteristic vibrations of OH, COOH, C=C and C-O groups appearing at  $3430$ ,  $1726$ ,  $1626$  and  $1055 \text{ cm}^{-1}$ , respectively, can be observed.

Exfoliation and single layer configuration of the GO suspended in water was assessed by AFM measurements of the flake thickness. Figures 2-5(a) and (b) show a typical AFM image of GO flakes that has a vertical height of 1.4 nm, which is in the range of the reported literature [11] values.

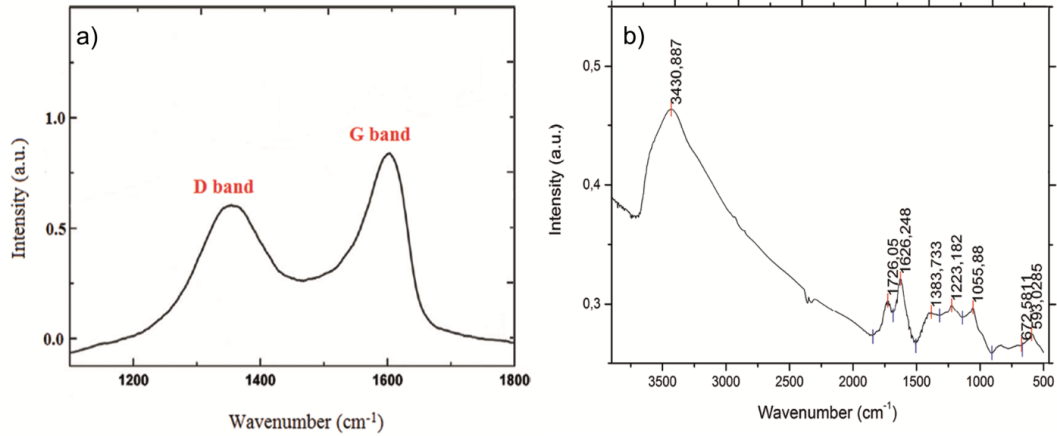


Figure 2-4 (a) Raman spectra recorded with  $\lambda = 514.5$  nm Ar ion laser excitation source. D-G bands are indicated, and (b) Infrared Spectroscopy of GO powder. Characteristic vibrations of OH ( $3430\text{ cm}^{-1}$  attached heteroatoms), of COOH ( $1726\text{ cm}^{-1}$ ), of C = C ( $1626\text{ cm}^{-1}$ ) and C - O ( $1055\text{ cm}^{-1}$ ), respectively, can be seen.

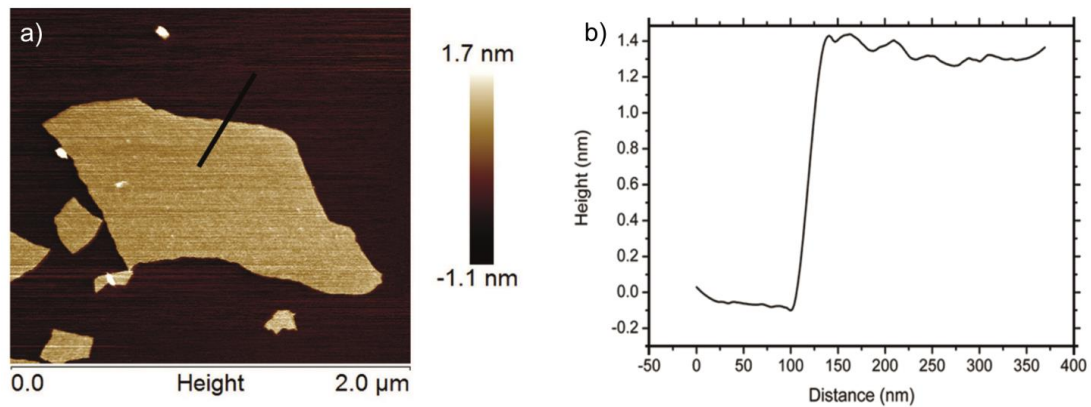


Figure 2-5 (a) Typical AFM image of GO sheets, and (b) Single layer thickness of GO sheet at 1.4nm.

### II.3.2 Drop - Casting technique for GO deposition

As represented in Figure 2-6, drop-casting utilizes the topographical impingement of a liquid solution, usually results in a spreading ‘stamp’, thus providing several difficulties to control the topography of a non-uniform thin solid film after the solvent evaporation. However, drop-casting is simple, low-cost, versatile, and potentially scalable casting method [12]. Hence, regarding the GO deposition method, the sensor platforms were heated at  $80\text{ }^{\circ}\text{C}$ . The GO solution was maintained at room temperature and a circular spot was deposited by using drop casting [13] on the area between the transducers. The ink was administered from a distance of 1mm and a drop

size was of  $0.05\text{ml}\times\text{min}^{-1}$ . In total, two drops per site were used and the ink was allowed to dry for 1 hour. As represented in Figure 2-7 the integration of alternative graphene-structured materials was successful by using a standard drop-casting deposition method. Analytically, all the drop-casted solutions were prepared by Prof. Hermenegildo Garcia (ITQ Valencia), thus initiating the amalgamation of graphene related Love wave devices. As described earlier, the actual material synthesis and solution preparation were mainly focused on highly oxidized graphene inks, since they revealed interest in the establishment of this thesis. Moreover, the sample numbers on the coated devices correspond to particular wafer tape-outs, such as no.7: Run37, Wafer B, device 07. Then the samples were named according to the traits of the sensing layer characteristics. A summary of the graphene based devices is represented in the Figure 2-7, i.e., (a) Device no.7 was coated with a highly oxidized graphene solution or namely called ‘upraised’ graphene oxide; (b) Device no.8 was coated with a graphene solution (flakes); and (c) Device no.09 was coated with a standard oxidized graphene solution, but nonetheless the oxidation level remained lower than the Device no.07, respectively.

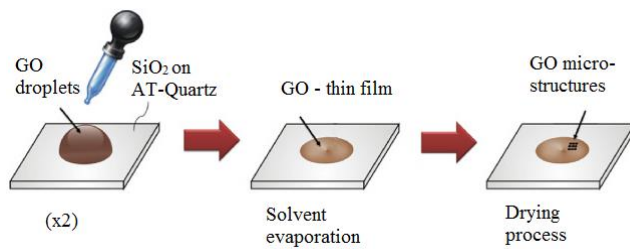


Figure 2-6 Representation of the GO drop-casting technique and process integration.

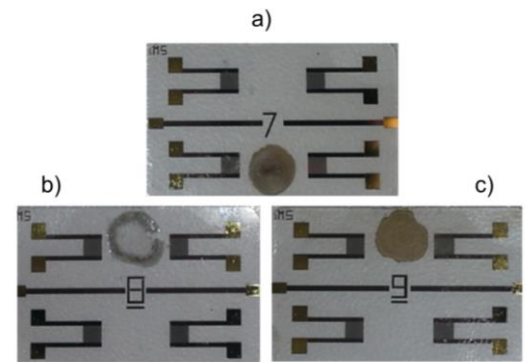


Figure 2-7 Drop-Casting deposition technique of different graphene-based materials, such as (a) Upraised-GO, (b) Graphene flakes, and (c) Standard-GO structures, respectively.

A first observation of the GO deposition sample (no. 07 - Run) was performed by an optical microscope in order to evaluate the uniformity of drop casting. Figures 2-8(a) and 2-8(b) illustrate the morphology of different droplet formations, especially in the outer and center highly oxidized graphene areas, respectively. The initial observations from the optical point of view showed a particular interest towards GO morphologies; however, each GO synthesis has unique properties tailored to the specific laboratory know-how conditions.

Notwithstanding the limitations of the methodology used (optical microscope), it was important to provide further GO morphological analysis based on a High - Resolution Scanning Electron Microscope (H-R SEM). For instance, the morphology and shape information derived from the detection of secondary electrons in H-R SEM and the recorded SEM images of the top and tilted GO areas were recorded respectively, as shown in Figure 2-9(a)-(h). To give an illustration of the thickness and to show clearly the GO morphology, tilt-sectional H-R SEM images were recorded

at a scale of 100nm. As shown in Figure 2-9(h), the dimensions identified that the GO film thickness was in the range of 285-338nm. In the evidence of further morphological analyses, the H-R SEM images have been shown that GO solution was uniformly distributed in a wide range of the sampling areas. Likewise, GO analysis of this work argues compellingly in favor of the current literature [14], and further provides essential information towards structure formation, characteristics and distribution of GO deposits.

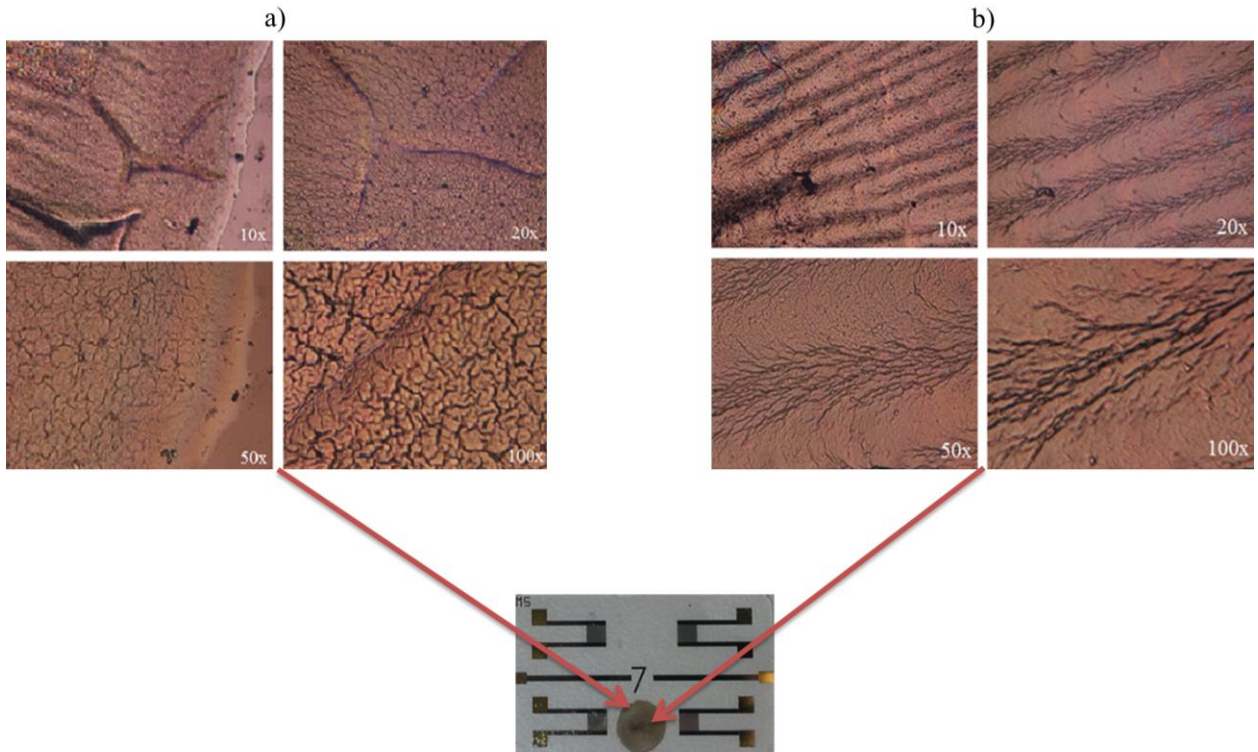


Figure 2-8 (a) Optical Microscope (Polyvar) images of the GO sample - extended magnification on the outer perimeter of the droplet formation, and (b) Optical Microscope (Polyvar) images of the tilted GO sample - extended magnification on the center of the droplet formation.



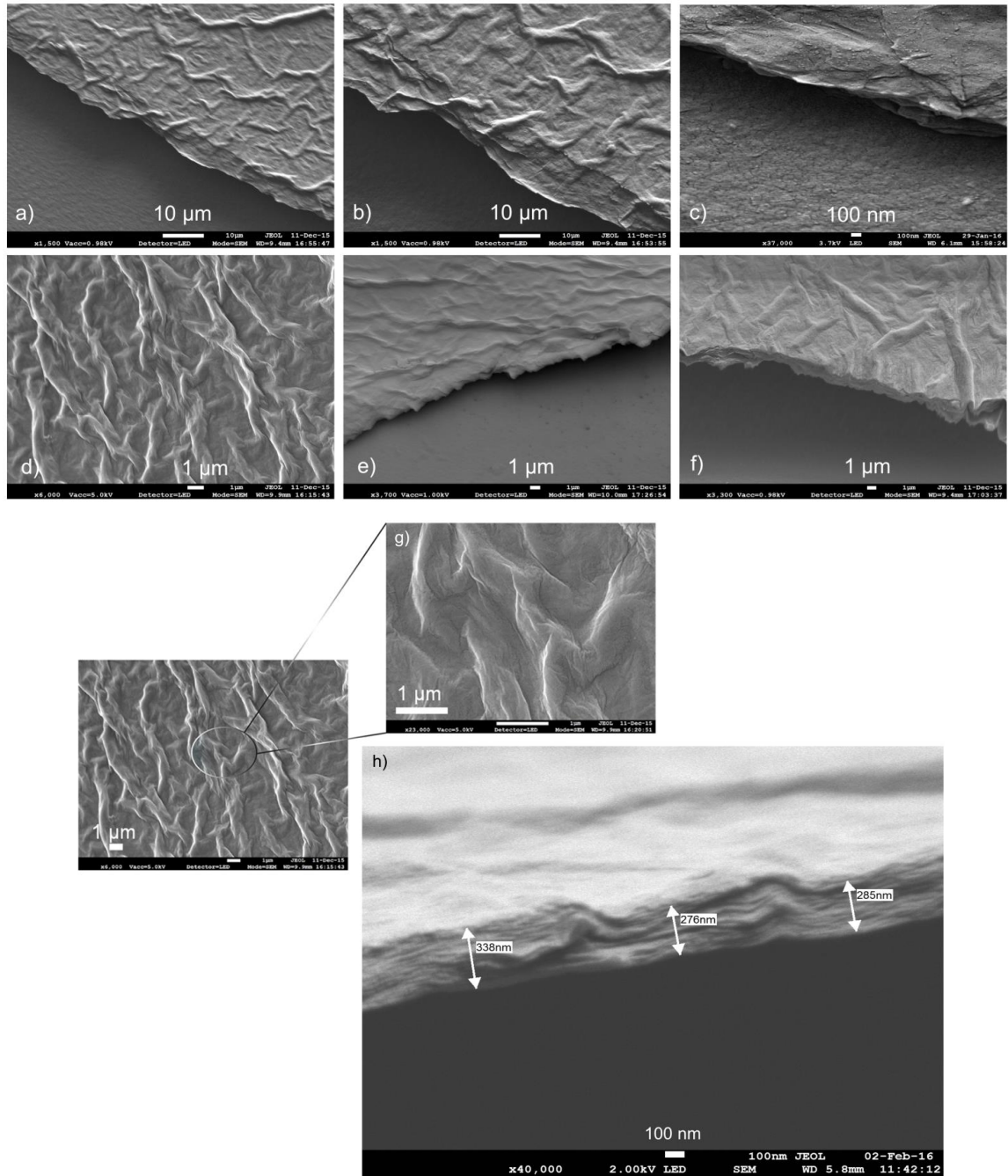


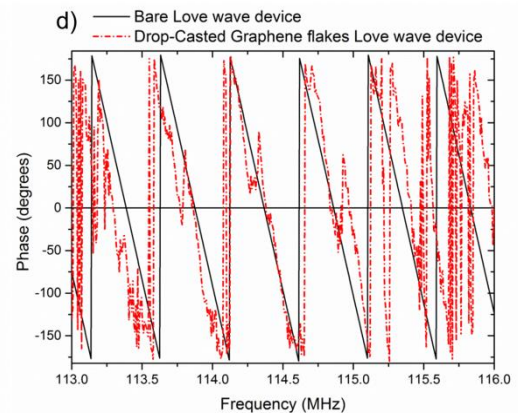
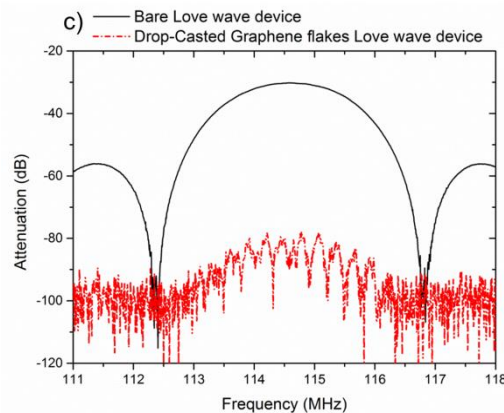
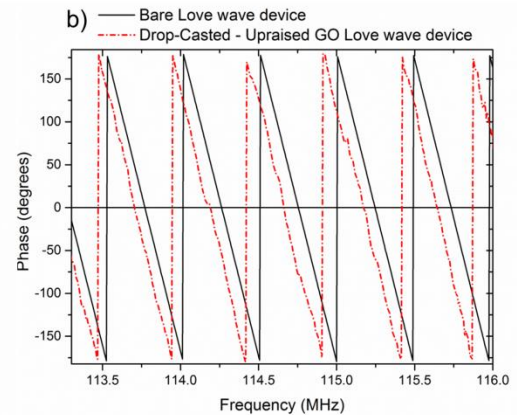
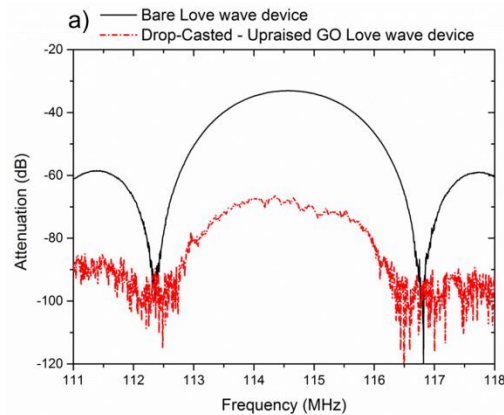
Figure 2-9 Top-sectional SEM images of the GO sensing layer (a), (b), (g); Tilt-sectional SEM images of the GO layer (c), (d), (e), (f), (h); The (d) GO area shows particular interest and it is primarily extended, magnified and analyzed in (h), to show clearly the GO morphology.

In conclusion, the evidence points almost exclusively shed light on the drop-casting technique of the GO solutions. Above all, it seems pertinent to remember that successful tailoring of the material process integration was based on three key characteristics: firstly, the high-quality of the graphene oxide sustained solutions; secondly, the initial conditions of the GO droplet formation. And thirdly, the calibration and measurement techniques of the H-R SEM were based on sample preparation, especially for the non-infringement areas in the outer perimeter of the GO droplet formation.

### II.2.3. Electrical characterization of the Drop-Casted GO Love wave devices

The electrical characterization of the Drop-Casted GO Love wave devices was performed by using the Network Analyzer ANRITSU-MS2026B, to maintain similar measurement conditions with bare and coated acoustic wave devices, respectively. Hence, a wide high-accuracy spectrum has been selected in the VNA measurement setup to determine the minimum of insertion loss, of the bared and coated delay lines, and to obtain electrical performances of the graphene sensory devices. Fig. 2-10 (a) and (b) illustrate the transmission line characteristics ( $S_{21}$ ) in terms of the attenuation and phase, respectively. The minimum of insertion loss for the bared devices is about -33 dB, corresponding to a synchronous frequency equal to 114.595 MHz and the phase shows a linear evolution in the useful frequency range. As mentioned earlier, the samples were categorized and electrically characterized according to three different groups that of highly oxidized graphene (Upraised – GO), graphene flakes and standard oxidized graphene devices, respectively. Moreover, the characterization results of the graphene devices are provided below in support of

- Sample no.07: Figures (a) and (b) - Integrated Upraised - GO on Love wave devices.
- Sample no.08: Figures (c) and (d) - Integrated Graphene flakes on Love wave devices.
- Sample no.09: Figures (e) and (f) - Integrated Standard - GO on Love wave devices.



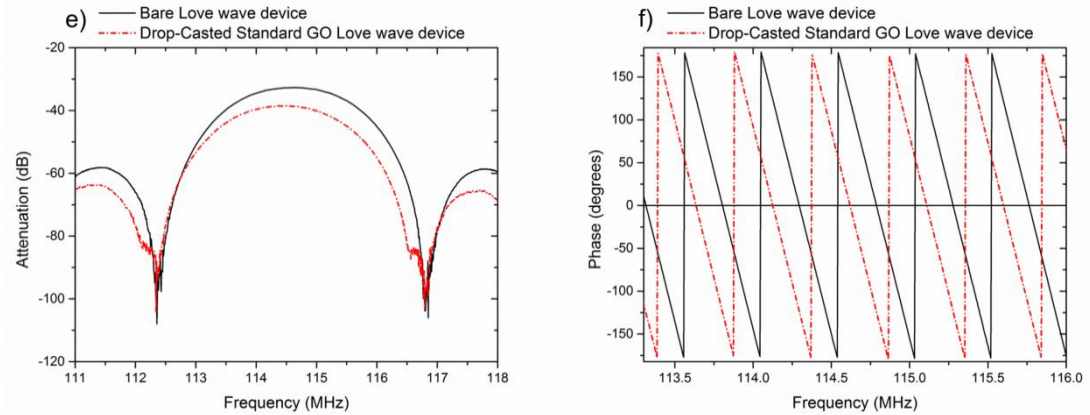


Figure 2-10 Summary transmission line characteristics ( $S_{21}$ ) in terms of the attenuation and phase of (a)-(b) Upraised – GO, (c)-(d) Graphene flakes, and (e)-(f) Standard – GO materials integrated on Love wave devices, respectively.

Notably, the Upraised - GO coated delay line shows that  $S_{21}$  parameters are strongly modified after the deposition. From the insertion loss curve as a function of frequency, the supplementary insertion loss is nearly -34 dB, near its synchronous frequency. Also, the frequency shift in phase corresponds to -55.625 kHz. Electrical characterization shows that even high GO thicknesses can be supported on the top of the Love wave sensor, as shown in the Figure 2-10 (a). Figures 2-10 (a), (c) and (e) show clearly that different graphene composition will have a great impact on the coated devices. However, in order to maintain the Love wave excitation with an over-layer hyper-oxidized graphene, it is essential to take account of the viscoelastic characteristics of each graphene composition, separately, as well as its thickness. In general, the device sensitivity increases as the acoustic wave velocity at the sensing surface increases - i.e., as the acoustic energy is trapped to the GO sensing surface. For instance, a purely elastic, lossless film will have different energy confinement than Upraised - GO (high insertion loss) sensor since the acoustic wave energy will most likely be confined between the Quartz -  $\text{SiO}_2$  and  $\text{SiO}_2$  - GO interfaces, respectively.

In particular, regarding the electrical characterization analysis of the Upraised – GO based Love wave device (sample no.07, named as R37B07), it has been shown that high insertion loss occurred with the current deposition aspects. However, high efficiency of the vapor sensing detections ensured and necessitated a further investigation analysis of the GO cross-sensitivity, since its predisposed detections will be discussed in a later chapter. Even with an attenuation of -34 dB and frequency shift of - 55.625 kHz, the devices showed high performances, especially on the humidity-based applications. Furthermore, the Fig. 2-10 (a)-(b) have been depicted to this graph representation in order to show the whole perspective of the Drop-Casting nano-structured materials and to compare the nearly operated insertion loss with different coated Love wave devices.

The upcoming material integration covers the graphene flakes coated Love wave device. Here, the coated delay line of the sample no.8 (named as R37B08 - after the deposition) provides a very high insertion loss, such as -48 dB in terms of attenuation and frequency shift equal to -45.625 kHz, as illustrated in Fig. 2-10 (c)-(d), respectively and therefore makes the device inoperable. Particular problems were observed with the surfactant / graphene flakes' solution, which may be related to the high ratio of the surfactant to the initial solution, thus leading to a higher density of the surfactant / flakes ink solution integration, since high insertion loss recorded on the acoustic wave devices.

Finally, regarding the sample no.9, named as R37B09, the Standard-GO solution was coated on the Love wave device. In this case, the coated delay line provides an operable insertion loss, such as a -6 dB in terms of attenuation, with a relative frequency shift of -169.375 kHz, as depicted in Fig. 2-10 (e)-(f). Even though the sample no.9 has provided promising preliminary results, low performance characteristics were observed at the vapor sensing applications.

In conclusion, a particular interest was shown to the comparison of different oxidation levels of the graphene solutions, especially due to the high amount of insertion loss of the Upraised - GO Love wave devices. Most likely, this effect is related to the oxidation level of the graphene solution, as represented in Figure 2-10 (e)-(f), and it was then analyzed electrically based on similar deposition aspects. Finally, the Standard - GO provides more value than the Upraised - GO integrated sensor, in terms of attenuation and frequency shift, respectively. However, in comparative terms, gas sensing performances proclaimed that Upraised – GO coated Love wave devices would be the main objective to identify different target analytes and establish high sensing performance characteristics.

The main interest of the carbon-based materials, as will be discussed in Chapter IV (gas characterization) analytically, resides in the study of the Upraised – GO regime, which is inextricably correlated with the results-oriented comparison studies. Subsequently, particular GO surfaces were selected to further understand, analyze and tailor the morphology of the next generation of hyper-oxidized graphene - Love wave devices.

## II.4 Preparation of GO based materials and Inkjet-Printing deposition technique

### II.4.1 Graphene Oxide solution preparation and its characterization

A commercial GO solution ( $C = 0.5 \text{ mg. mL}^{-1}$ ) was purchased from Graphene Supermarket® (HC Graphene Oxide aqueous solution). Briefly, the GO commercial solution is based on the oxidization of crystalline graphite with the mixture of sulfuric acid, sodium nitrate, and potassium permanganate i.e. well-known Hummers' method.

For the preparation of the GO inks, a commercial GO solution ( $C = 0.5 \text{ mg. mL}^{-1}$ ) and ethylene glycol (purity  $\geq 99.5\%$ ) were purchased from Graphene Supermarket® (HC Graphene Oxide aqueous solution) and Sigma-Aldrich, respectively, and used as received. The elemental

composition of this solution revealed the presence of carbon (79%) and oxygen (20%), with a flake size between 0.5 - 5 microns, as illustrated in Figure 2-11.

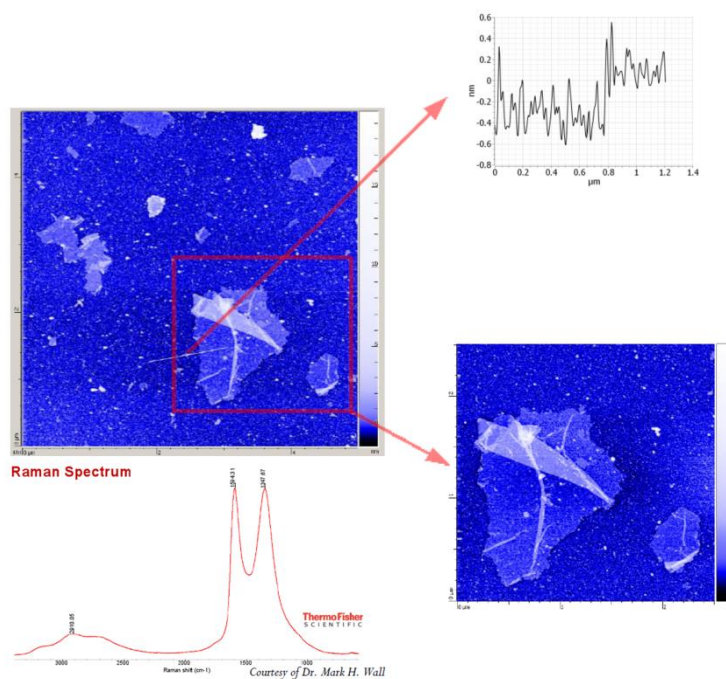


Figure 2-11 AFM image and height profile of the GO commercial solution deposited onto functionalized mica. The image was generated by SmartSPMTM (AIST-NT, Inc.), Courtesy of Dr. Andrey Krayev [15], [16].

Structurally, GO can be visualized as a graphene sheet with its basal plane decorated by oxygen-containing groups (Fig. 2-11 – Raman spectra). Due to high affinity to water molecules by these groups, GO is hydrophilic and can be dissolved in water. The solubility in water makes the deposition of the thin films of the GO straightforward. Conventionally, the reduction is done by hydrazine. GO and its reduced forms have an extremely high surface area; because of this, these materials are under consideration for usage as electrode material in batteries and double-layered capacitors, as well as in studies of hydrogen storage, fuel cells, and gas sensor applications [17]. Moreover, the particular GO solution was selected to enhance further the vapor performance of humidity applications separately, since the solution offers GO with Brunauer-Emmett-Teller (BET) Specific Surface Area as high as  $833 \text{ m}^2/\text{g}$ .

Furthermore, regarding the final step of the GO-ink preparation, water-dispersed GO sheets were used to prepare GO/ethylene-glycol composites by modifying the initial viscosity of the GO commercial solution and realizing a feasible ink-jet printing for large scale applications. It was found that GO sheets undergo excellent morphological distribution within the ethylene-glycol, giving rise to transparent and semi-transparent composites. In order to prepare the ink composed of GO ( $\gamma = 0.42 \text{ mg} \cdot \text{mL}^{-1}$ ), an amount of 0.6g of ethylene glycol was added to the 3 g of GO solution under stirring. Assuming that the density of aqueous GO/ethylene glycol does not differ significantly from the density of the pure water, the weight percentage of GO was calculated to be 0.042 wt %.

## II.4.2 Inkjet-Printing integration of Graphene Oxide thin films

In general, the GO-sensitive film deposited on the acoustic device is of primary importance, which has to be efficient for target immobilization/recognition, lossless in regards to the acoustic wave, reproducible and has to meet friendly properties in terms of industrial processability. The proposed GO inkjet-printing integration technology is based on the strategy to provide an easy, low-cost, reproducible, energy-saving and environmentally friendly technique that can find a wide range of applications in coating technology. Drop on Demand (DoD) inkjet-printing process [18] has been used in order to deposit GO modified solutions on Love wave devices. Moreover, microfabrication print head assemblies have been integrated as subsystems into a custom commercial inkjet system (Alta-Drop), as represented in the Fig. 2-12. Droplets are produced by pressure/velocity transients that are caused by volumetric change, which are induced by a piezoelectric feature. This part was performed in close collaboration with LAAS-CNRS [19].

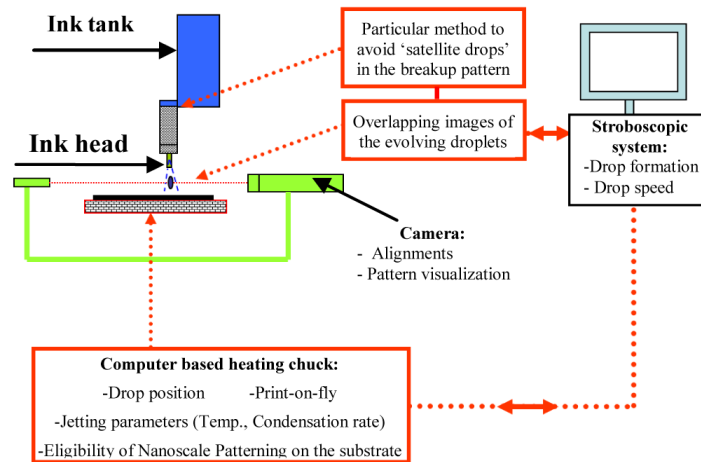


Figure 2-12 Inkjet - Printed GO/ethylene-glycol processability overview.

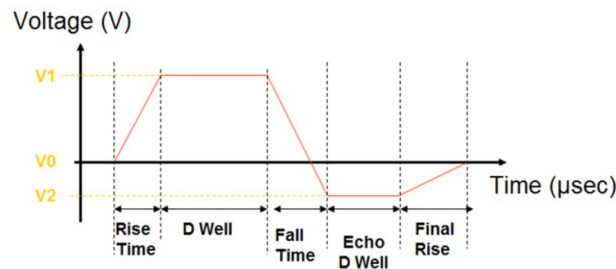


Figure 2-13 Bipolar actuation pulse of the print-head.

Figure 2-13 illustrates a common bipolar waveform, along with a brief description of the significance of each section of the waveform, such as voltages and times, respectively (Table 2.1 – jetting parameters). In this case, a double trapezoidal waveform was applied to the print-head to generate the sensing material droplets. The reason that the waveform contains two trapezoidal

pulses is that the standard pulse (positive pulse) which is used in the print-head consists of one resonating pulse. Notwithstanding a positive trapezoidal pulse is able to jet a drop efficiently, however it generates residual oscillations. In order to cancel any of these residual oscillations, the positive pulse was followed by a negative trapezoidal pulse, as illustrated in the Fig. 2-15. Moreover, the profile and magnitude of the applied waveform of 50 microns nozzle head in diameter are presented on table 2-1 and Figure 2-13, respectively.

Waveform *	Voltage characteristics	Times
Initialization	$V_0 = 0$ Volts	1 sec
Positive	$V_0$ to $V_1$ transition	<b>Rise time: 6 <math>\mu</math>sec</b>
Positive	$V_1 = 35$ Volts	<b>Dwell: 25<math>\mu</math>sec</b>
Positive/Negative	$V_1$ to $V_2$ transition	<b>Fall Time: 5<math>\mu</math>sec</b>
Negative	$V_2 = -35$ Volts	<b>Echo D Well: 4<math>\mu</math>sec</b>
Negative	$V_2$ to $V_0$ transition	<b>Final Rise: 1<math>\mu</math>sec</b>

Table 2.1: GO/ethylene glycol jetting parameters. \* Bipolar waveform jetting characteristics.

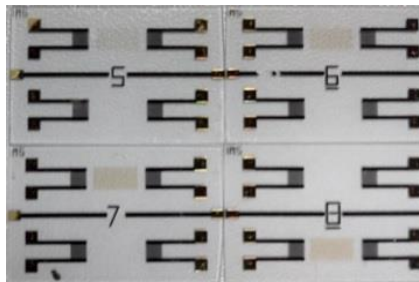


Figure 2-14 Inkjet - Printed GO coatings on Love wave devices. The above-named devices 5-6-7-8 therefore correspond to 1-2-3-4 Inkjet-Printed GO passes, respectively.

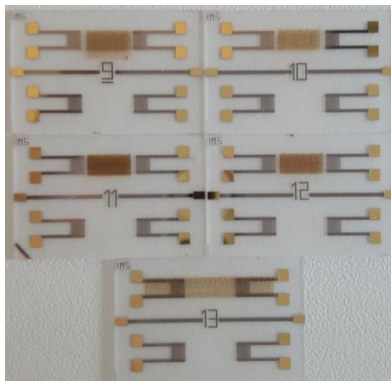


Figure 2-15 Inkjet - Printed GO coatings on Love wave devices. The above-named devices 09, 10, 11, 12 and 13 therefore fulfill the comparison study of different printed GO passes, as represented in the table 2.2, respectively.

Run40 * information	Sample number	Number of inkjet passes and position
<b>Initialization of jetting</b>	<b>No. 05 (Top)</b>	<b>1 - between the IDTs</b>

<b>Low thickness investigation</b>	<b>No. 06 (Top)</b>	<b>2 - between the IDTs</b>
<b>Coverage approach</b>	<b>No. 07 (Top)</b>	<b>3 - between the IDTs</b>
<b>Thickness optimization</b>	<b>No. 08 (Bottom)</b>	<b>4 - between the IDTs</b>
<b>Reproducibility of jetting</b>	<b>No. 09 (Top)</b>	<b>4 - between the IDTs</b>
<b>Reproducibility of jetting</b>	<b>No. 10 (Top)</b>	<b>4 - between the IDTs</b>
<b>Extra-passes investigation</b>	<b>No.12 (Top)</b>	<b>6 - between the IDTs</b>
<b>Multi-passes investigation</b>	<b>No.11 (Top)</b>	<b>10 - between the IDTs</b>
<b>Over-coated (full-length)</b>	<b>No.13 (Top)</b>	<b>4 - whole area and IDTs</b>

Table 2.2: GO comparison study of jetting passes characteristics. \* Run40 - Wafer A, IMS database.

Consequently, this novel compound determined that a stable jet was formed when using the following composition formation of the selected mixture (GO-ink), as illustrated in Figures 2-14 and 2-15. Furthermore, the temperature of the samples during the jetting was maintained at 80 °C with a delay of one second between two different drops, thus allowing the evaporation of the solvent efficiently. The inkjet-printed GO occupies a rectangular surface area measuring 17mm by 2.6mm and the jetting process was fully realized in 60 minutes; however, a multi-nozzle technique can be easily adapted to decrease the time of the GO based depositions. Precisely, 208 columns and 32 lines were printed with a resolution of 80µm, respectively, at the same contact angle (less than 10°). The implementation of the ultraviolet light (UV) or ozone treatment of the SiO<sub>2</sub> plays an important role in the sustainability of a stable jet process, since the drop lands on a pre-treated surface. The thickness of the inkjet-printed films was varied by increasing the same track in extra- and multiple passes, starting from 1-4 times up to 10 times (see table 2.2).

As expected, the following comparison study has raised after recognizing the detection limits of several VOCs and humidity, however for the sake of completeness and clarity, a summary of this analysis follows. Exploration of high number of jetting passes (GO/ethylene glycol) were realized to fabricate alternative sensing thin films based on cross sensitivities to gases such as, C<sub>2</sub>H<sub>6</sub>O, C<sub>7</sub>H<sub>8</sub>, NO<sub>2</sub>, or water vapor. The comparison study and the full-length GO coverage approach of the Love wave devices endorses the notion that different thicknesses can be utilized according the detection demands of the specified / targeted analytes.

### II.4.3 Inkjet-Printing characterization of Graphene Oxide thin films

For the sake of discussion, it was clarified earlier the number of the printing passes corresponds to the counted number of the printing layers and not to the number of the GO layers, since the size of a GO monolayer is about  $1.1 \pm 0.2$  nm thick (Graphene Supermarket®). Furthermore, a multilayer configuration of the GO suspended in ethylene glycol was assessed by optical interference profiling measurements to obtain accurate surface information of each printed layer.



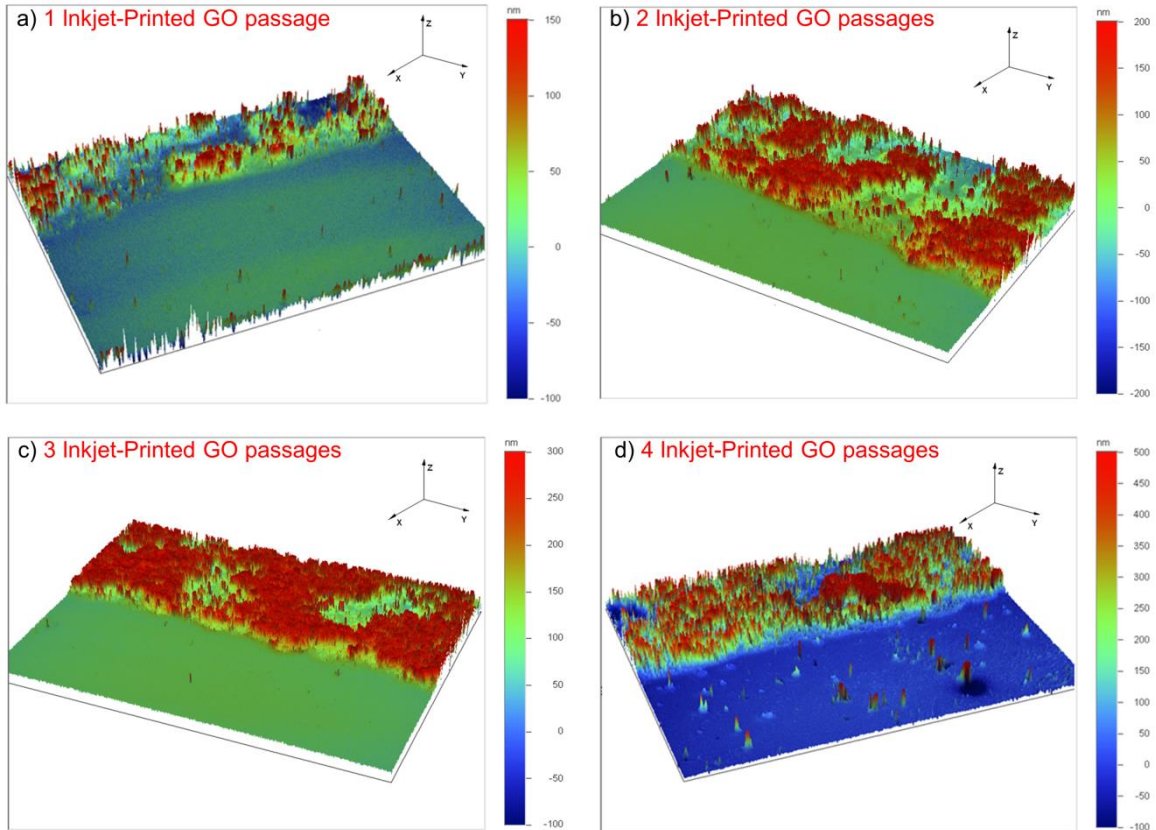


Figure 2-16 Optical interference profiling (3D) of 1, 2, 3- and 4-layers Inkjet - Printed GO films.

The optical profiles of the Figure 2-16 (a), (b), (c) and (d) represent typical 3D images of the GO sheets that have an average vertical height of 89.3 nm, 180.8 nm, 268.2 nm and 436.5 nm for 1, 2, 3 and 4 Inkjet-Printed GO passages, respectively in the range of what has been reported in the GO-ink solution specifications. In particular, the repeated GO passes showed a good uniformity and coverage of the  $\text{SiO}_2$  substrate, especially at higher number of passages, and subsequently at higher thickness levels, as illustrated in Figure 2-16 (c)-(d). The analysis of the microstructure of the printed process shows that the GO sheets were formed a continuous layer with each other, thus ensuring continuity of the GO coating films; even at lower thicknesses (no trenches were observed).

A further investigation showed that the morphology of G-O on top of a device covered by 4 inkjet-printed passes, as depicted in Figure 2-17 (a) was studied by Scanning Electron Microscopy (SEM) followed by the Figure 2-17 (b and c - its extended magnification) along with Atomic Force Microscopy (Figure 2-18 (a)). Analytically, the corresponding image magnification of very high oxidation areas in the SEM images (Figure 2-17(c)) shows indeed that GO sheets exhibit typical wrinkled behavior that caused sheet folding [20], [21].

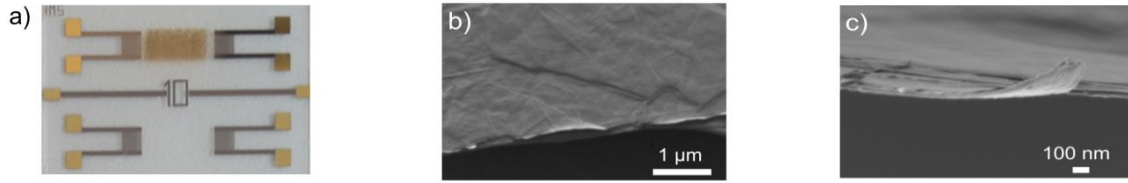


Figure 2-17 GO nanosheets - (a) Optical microscope image of the 4 GO passes, (b) Tilt-sectional SEM image of the 4 GO passes, and (c) its corresponding image magnification, respectively.

Furthermore, topographic tapping-mode Atomic Force Microscopy (AFM) imaging of deposited GO on a GO/LW device and the corresponding Raman mapping of the very same area were performed using an instrument described in detail elsewhere [22]. AFM imaging was carried out by means of a commercial silicon probe (PPP-NCL, nominal resonance frequency 190 kHz, nominal force constant 48 N / m). Raman microscopic measurements were achieved under 561 nm irradiation using a 60 × glass-corrected microscope objective. A 10 s time integration was considered for each collected spectrum.

In addition, AFM measurements reveal significant height differences on the GO surface, suggesting a noticeable roughness of the GO films. For instance, the height difference between points 1 and 2 is only 9 nm, whereas it reaches 38 nm between points 3 and 4 (Fig. 2-18 (a)).

As AFM does not provide chemical characterization of the deposited GO, Raman microscopic measurements have been carried out in the very same region. Figure 2-18 (b) presents the Raman map plotting the ratio ID/IG between integrated intensities associated with the disorder-induced D band and the graphite-like G band, centered at  $\sim 1340$  and  $\sim 1600$   $\text{cm}^{-1}$ , respectively (Figure 2-18 (d)) [23]. Note that the significant breadth of the D band is directly related to the presence oxygen-induced defects in G-O and is fully congruent with the spectral line shape reported by the GO manufacturer (Graphene Supermarket® - HC Graphene Oxide aqueous solution). The values of the ID/IG ratio range between 0.7 and 1, which suggests an almost similar chemical fingerprint of GO over large regions. Furthermore, this chemical homogeneity spreads over the whole thickness of the GO film since the Raman peak at  $\sim 520$   $\text{cm}^{-1}$  assigned to the silicon of the AFM probe, and appears in all Raman spectra, thus showing that the GO film is completely probed by the 561 nm excitation. In fact, only subtle changes can be observed, as indicated by Raman spectra, corresponding to points 1 and 2 (Figure 2-18 (b) and (d)). This homogeneity is also reflected by the absence of clear correlation between the topographic AFM image and the ID/IG Raman map. This strongly contrasts with the Raman map inferred from the ratio ID+G/IQ, where ID+G stands for the sum of ID and IG integrated intensities, and IQ for the integrated intensity of the spectral feature assigned to the quartz substrate at 468  $\text{cm}^{-1}$  [24]. Protrusions are indeed conveniently associated with intense Raman signals (point 3 in Figure 2-18 (c) and (d)), while holes essentially lead to weak Raman signals (point 4 in Fig. 2-18 (c) and (d)), considering the limited 400-500 nm spatial optical resolution of the Raman map.

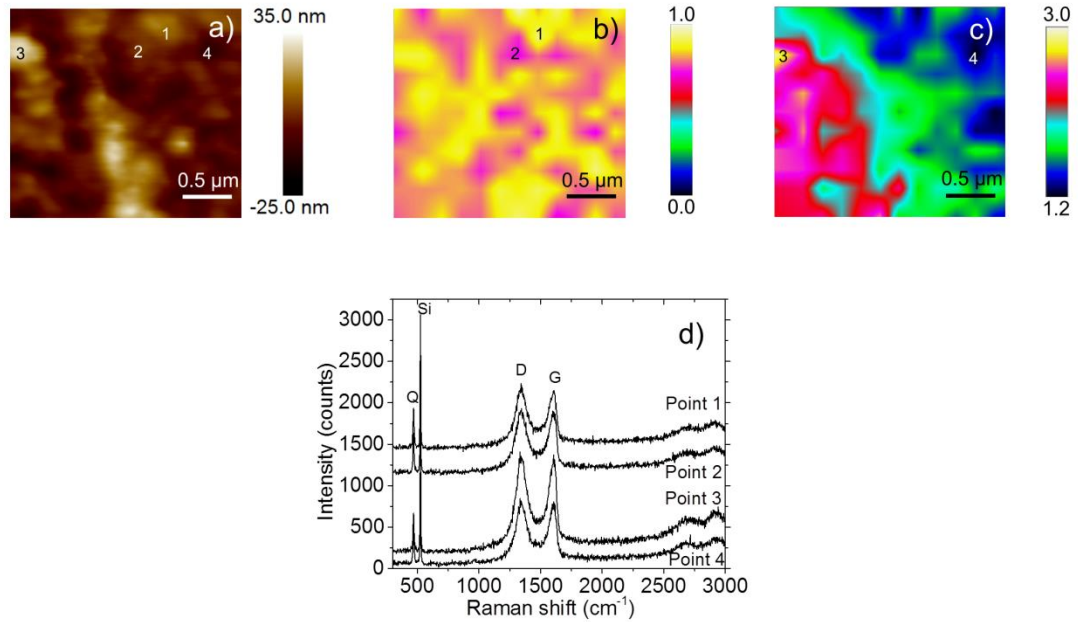


Figure 2-18 (a) Typical topographic tapping-mode AFM image of the device covered by 4 G-O inkjet-printed passes, and corresponding Raman maps showing the variation of (b) the intensity ratio  $I_D/I_G$ , and (c) the intensity ratio  $I_{D+G}/I_Q$ . (d) Raman spectra associated with 4 different areas (points 1, 2, 3 and 4). D and G bands assigned to G-O are indicated, as well as Q and Si bands attributed to the quartz substrate and the silicon AFM probe.

#### II.4.4 Electrical characterization of the Inkjet-Printed G-O thin films

S-parameters of the Inkjet-Printed sensing platforms were performed using a network analyzer (ANRITSU MS2026B). A wide high-accuracy spectrum has been selected in the radio-frequency network analyzer to determine the minimum of insertion loss, of the uncoated - coated delay lines. In order to obtain electrical performances of the Inkjet-Printed GO devices, sensor responses were recorded before and after the depositions of the GO coating solutions. The synchronous frequency was observed nearly at 116 MHz and the acoustic path characteristics were not strongly modified after the GO-ink deposition.

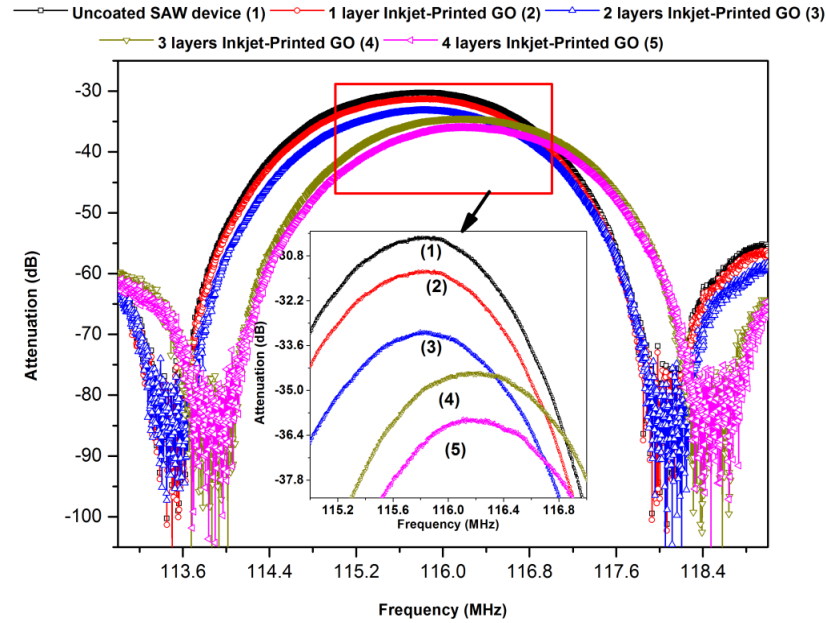


Figure 2-19 Attenuation before and after the deposition of 1, 2, 3 and 4 Inkjet - Printed GO sensitive coatings.

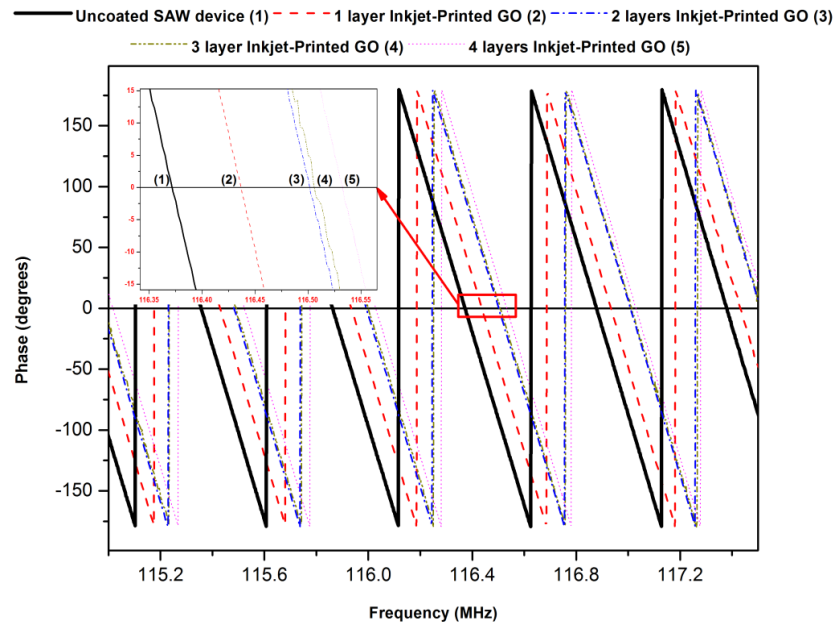
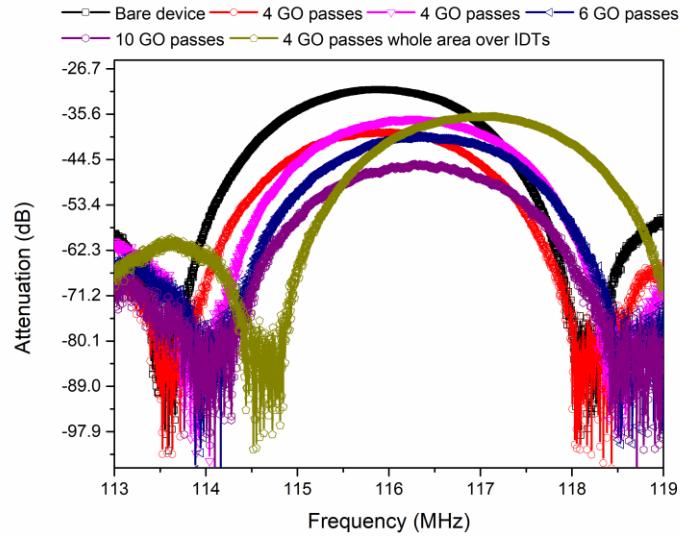


Figure 2-20 Phase before and after the deposition of 1, 2, 3 and 4 Inkjet - Printed GO sensitive coatings.

As represented in Figure 2-19, the induced GO insertion losses depend on the difference in size and thickness of inkjet-printed films and correspond to -1 dB, -1.92 dB, -3.35 dB and -4.62 dB for one, two, three and four GO passages, respectively. Furthermore, the phase shows a linear evolution in the useful frequency range (Figure 2-20). It was also observed a shift towards the high frequencies (i.e. a phase advance, especially after four GO passes). Figures 2-19, 2-20 and 2-21 show the evolution of the frequency shift when GO dispersions occurred on a full-length device or when the GO thickness is constantly increased between the IDTs. According to the electrical measurements of the reported samples in table 2.2, highlighting the sample no. 13 with

a particular interest, the properties of the GO dispersions on a full-length coverage device produce a positive shift in synchronous frequency regarding the  $S_{21}$  parameters.

a)



a)

b)

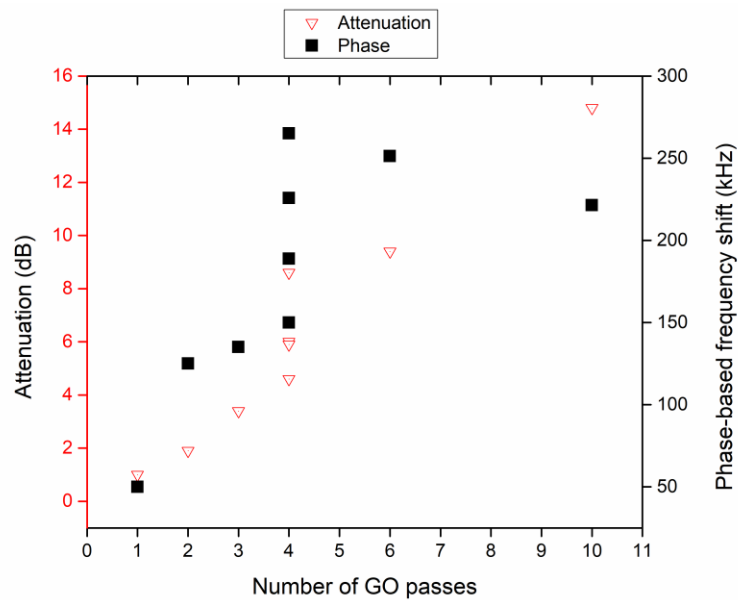


Figure 2-21 Electrical characterization responses of several coated GO/LW devices. Follow-up study comparison based on table 2.2 of the Inkjet-Printed GO sensitive coatings. (a-b) Sample no. 09 coated with 4 GO passes between the IDTs with an attenuation of -8.63dB and frequency shift of -225.75 kHz; Sample no. 10 coated with 4 GO passes between the IDTs with an attenuation of -6.02dB and frequency shift of -188.82 kHz; Sample no. 12 coated with 6 GO passes between the IDTs with an attenuation of -9.41dB and frequency shift of -251.21 kHz; Sample no. 11 coated with 10 GO passes between the IDTs with an attenuation of -14.78dB and frequency shift of -221.4 kHz; Sample no. 13 coated with 4 GO passes over the whole device and between the IDTs with an attenuation of -5.85dB and frequency shift of 265.01 kHz, respectively.

**Post-deposition effect of Inkjet-Printed GO – 4 GO passes over the IDTs:**

Elasto-viscosity is particularly significant in the systems of anisotropic [25] colloidal particles, polymers or composite-like materials, where external organic compound (ethylene glycol) can readily induce alignment and orientational order. To understand the orientational behavior of GO dispersions after the evaporation of the solvent and clearly understand the inkjet-printed GO impact on the Love wave devices, an analytical model was proposed that focused on the electrical characterizations of several inkjet-printed GO devices. Last but not least, physical implementation parameters of the GO devices predicate the necessity of having a regime that can be well modeled and analyzed by using finite element method (FEM), especially due to the Comsol physical modeling software, which will be discussed in the next chapter.

## References or Bibliography (if any)

- [1] Y. Xia, Y. Xiong, B. Lim, and S. E. Skrabalak, "Shape-Controlled Synthesis of Metal Nanocrystals: Simple Chemistry Meets Complex Physics?," *Angew. Chem. Int. Ed.*, vol. 48, no. 1, pp. 60–103, Jan. 2009.
- [2] H. Rohrer, "The nanoworld: chances and challenges," *Microelectron. Eng.*, vol. 32, no. 1, pp. 5–14, Sep. 1996.
- [3] A. K. Geim and K. S. Novoselov, "The rise of graphene," *Nat. Mater.*, vol. 6, no. 3, p. 183, Mar. 2007.
- [4] A. D. Franklin *et al.*, "High-density integration of carbon nanotubes via chemical self-assembly," *Nat. Nanotechnol.*, vol. 7, no. 12, p. 787, Dec. 2012.
- [5] C. Zimmermann, *Conception, réalisation et étude de micro-capteurs à ondes de Love pour applications en milieu gazeux: Cas de la détection de composés organophosphorés*. Bordeaux 1, 2002.
- [6] H. Tarbague, *Étude et mise au point d'une plateforme de biodétection de micro-organismes couplant immunocapteur a ondes de love et dispositifs PDMS microfluidiques*. Bordeaux I, 2011.
- [7] W. S. Hummers and R. E. Offeman, "Preparation of Graphitic Oxide," *J. Am. Chem. Soc.*, vol. 80, no. 6, pp. 1339–1339, Mar. 1958.
- [8] M. Wissler, "Graphite and carbon powders for electrochemical applications," *J. Power Sources*, vol. 156, no. 2, pp. 142–150, Jun. 2006.
- [9] B. Z. Jang, A. Zhamu, J. Shi, and J. Guo, "Carbon anode compositions for lithium ion batteries," US9029019B2, 12-May-2015.
- [10] D. C. Marcano *et al.*, "Improved Synthesis of Graphene Oxide," *ACS Nano*, vol. 8, no. 4, pp. 4806–4814, Aug. 2010.
- [11] S. Min and G. Lu, "Dye-Sensitized Reduced Graphene Oxide Photocatalysts for Highly Efficient Visible-Light-Driven Water Reduction," *J. Phys. Chem. C*, vol. 115, no. 28, pp. 13938–13945, Jul. 2011.
- [12] M. Eslamian and F. Zabihi, "Ultrasonic Substrate Vibration-Assisted Drop Casting (SVADC) for the Fabrication of Photovoltaic Solar Cell Arrays and Thin-Film Devices," *Nanoscale Res. Lett.*, vol. 10, Dec. 2015.
- [13] D. Li, M. B. Müller, S. Gilje, R. B. Kaner, and G. G. Wallace, "Processable aqueous dispersions of graphene nanosheets," *Nat. Nanotechnol.*, vol. 3, no. 2, pp. 101–105, Feb. 2008.
- [14] M. Beidaghi and C. Wang, "Micro-Supercapacitors Based on Interdigital Electrodes of Reduced Graphene Oxide and Carbon Nanotube Composites with Ultrahigh Power Handling Performance," *Adv. Funct. Mater.*, vol. 22, no. 21, pp. 4501–4510, 2012.
- [15] "Improved Synthesis of Graphene Oxide - ACS Nano (ACS Publications)." .
- [16] J. W. Suk, R. D. Piner, J. An, and R. S. Ruoff, "Mechanical Properties of Monolayer Graphene Oxide," *ACS Nano*, vol. 4, no. 11, pp. 6557–6564, Nov. 2010.
- [17] Y. Zhu *et al.*, "Graphene and Graphene Oxide: Synthesis, Properties, and Applications," *Adv. Mater.*, vol. 22, no. 35, pp. 3906–3924, Sep. 2010.
- [18] F. Torrisi *et al.*, "Inkjet-Printed Graphene Electronics," *ACS Nano*, vol. 6, no. 4, pp. 2992–3006, Apr. 2012.
- [19] D. Pech, M. Brunet, P.L. Taberna, P. Simon, N. Fabre, F. Mesnilgrete, V. Conédéra, and H. Durou, "Elaboration of a microstructured inkjet-printed carbon electrochemical capacitor," *Journal of Power Sources*, vol. 195, no. 4, pp.1266-1269, 2010.

- [20] H. Zhang and P. X. Feng, “Fabrication and characterization of few-layer graphene,” *Carbon*, vol. 48, no. 2, pp. 359–364, Feb. 2010.
- [21] L. Ortolani *et al.*, “Folded Graphene Membranes: Mapping Curvature at the Nanoscale,” *Nano Lett.*, vol. 12, no. 10, pp. 5207–5212, Oct. 2012.
- [22] D. Talaga, M. Comesaña-Hermo, S. Ravaine, R. A. L. Vallée, and S. Bonhommeau, “Colocalized dark-field scattering, atomic force and surface-enhanced Raman scattering microscopic imaging of single gold nanoparticles,” *J. Opt.*, vol. 17, no. 11, p. 114006, 2015.
- [23] D. Kostiuk *et al.*, “Reliable determination of the few-layer graphene oxide thickness using Raman spectroscopy,” *J. Raman Spectrosc.*, vol. 47, no. 4, pp. 391–394, Apr. 2016.
- [24] R. S. Krishnan, “Raman Spectrum of Quartz,” *Nature*, vol. 155, no. 3937, p. 452, Apr. 1945.
- [25] S. Naficy *et al.*, “Graphene oxide dispersions: tuning rheology to enable fabrication,” *Mater. Horiz.*, vol. 1, no. 3, pp. 326–331, 2014.





## Chapter 3

### Sensor simulation

## III. Theoretical studies

### III.1 Introduction

The scope of this chapter is focused on the theoretical analysis of the graphene oxide-based SH-SAW sensors. The main theoretical premise behind the Love wave devices is that by using a piezoelectric substrate and an over-layer with a lower shear wave velocity, a Love wave can be generated and propagated [1]. The advantage of this mode is that it operates a thin trapping layer to guide the propagating wave to the surface of the substrate instead of alternative invasive detection methods.

From a materials point of view, if inkjet-printed GO dispersions exhibit Newtonian or non-Newtonian (shear thinning) behavior, it had to be defined at which GO formed composition (thickness analogous to passages) and/or on how many passages have to be realized to exceed a typical shear-thinning behavior. Furthermore, it was essential to study the mechanical properties of GO composites regarding the Inkjet-Printed deposition method towards future enhancements of the GO devices. Theoretical investigation approaches, such as analytical modeling through the electrical behavior of the GO Love wave devices, as well as FEM analyses could provide useful information in order to explain the physical mechanical properties of the GO sheets, respectively. The necessity of having an analytical approach is to uncover the ‘golden ratio’ of the unique GO viscoelastic properties, previously reported in [2], since multiple GO passes could be realized as an appealing technique to unambiguously discern between different gas multi-sensor environmental applications. For these reasons, modeling results were able to provide further understanding of the rheological properties of the GO-inks. Therefore, highly-tuned Inkjet-Printed GO devices provided higher cross-sensitivities of the target analytes. Moreover, the viscosity is found to show non-monotonic behavior with higher GO compositions, or monotonic for particular regimes, which will be discussed later.

### III.2 Modeling of the Love wave sensor

A particular coordinate system set up was defined according to the piezoelectric material orientation of an AT-cut quartz crystal. Figure 3-1 represents the coordination system used for the acoustic wave solutions. Precisely, the tensor constants (stiffness, piezoelectric and permittivity) of a piezoelectric AT-cut quartz crystal have been calculated and used in numerical and analytical modeling as parameters based on the Euler angles ( $\varphi = 0^\circ$ ,  $\theta = 121.5^\circ$ ,  $\psi = 90^\circ$ ).

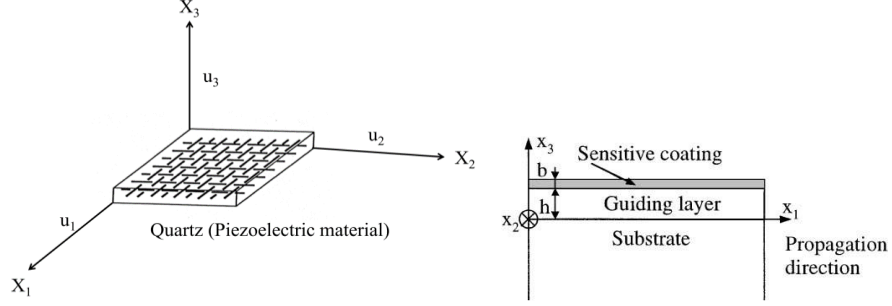


Figure 3-1 The coordinate system of the acoustic wave solutions.

The  $X_1$  acoustic wave propagation direction with a rotated  $Y$  – cut quartz crystal is determined by the calculated constants of the novel coordinate system, respectively. Thus, by selecting the piezoelectric devices module of the FEM model, the coupled constitutive equations (3.1, 3.2, 3.3, and 3.4) can be represented in the Table 3.1:

Stress-Charge expression	
Numerical formula: Matrix representation	Analytical formula
$T = c_E \cdot S - e^T \cdot E$ (3.1)	$T_{ij} = C_{ijkl}^E \cdot S_{kl} - e_{ijk} \cdot E_k$ (3.3)
$D = e \cdot S + \varepsilon_s \cdot E$ (3.2)	$D_j = e_{jkl} \cdot S_{kl} + \varepsilon_{jk}^S \cdot E_k$ (3.4)

Table 3.1: Stress-Charge expression formulas.

where:  $i, j, k, l = 1, 2, 3$ , respectively and represent the  $X_1, X_2$ , and  $X_3$  directions on Figure 3-1. When considering the expanded formula,  $T_{ij}$  is the stress,  $S_{kl}$  is the strain (which is equal to  $\frac{1}{2} \left( \frac{\partial u_k}{\partial x_l} + \frac{\partial u_l}{\partial x_k} \right)$ , where  $U_k$  and  $U_l$  represents the particle displacement),  $E_k$  is the electric field,

which is equal to  $\left( \frac{-\partial \Phi}{\partial x_k} \right)$ , where the electric potential is noted by  $\Phi$ ,  $D_j$  is the electric displacement,  $C_{ijkl}^E$  is the elasticity matrix,  $e_{jkl}$  is the coupling matrix and  $\varepsilon_{jk}^S$  is the permittivity matrix. The expanded formulas (equations 3.3 and 3.4) are calculated by COMSOL according to the Cartesian coordinate system, and are expressed as equation (3.1) and equation (3.2). In order to inquire the numerical simulator, we need to express:

$C_E$  = the elasticity matrix (rank 4 tensor equivalent)

$e^T$  = transpose coupling matrix (rank 3 tensor equivalent)

$e$  = coupling matrix (rank 3 tensor representation)

$\varepsilon_s$  = permittivity matrix (rank 2 tensor representation)

To acquire the expression of the acoustic displacements of the Love wave device, it is necessary to calculate the pure Shear Horizontal (SH) displacement  $u_2(X_1, X_3, t)$  in each of the volume materials components constituting the Love wave device. Regarding the conditions of the Love wave sensors, the plane acoustic wave is propagating along the  $X_1$  and  $X_3$  direction and the particle displacement is in the  $X_2$  direction (Figure 3-1). The particle displacement can be expressed by the Equation (3.5) below:

$$u_2(x_1, x_3, t) = A \cdot e^{j[\omega t - k_1 x_1 - k_3 x_3]} \quad (3.5)$$

where: A is the amplitude of the particle displacement,  $\omega$  is the angular frequency,  $k_1$  is the wavenumber in the  $X_1$  direction,  $k_3$  is the wavenumber in the  $X_3$  direction and j is the imaginary unit.

<p>«French» literature: The wave is provided by: <math>U = U_0 e^{j(\omega t - kx)}</math> The wave vector is written by: <math>k = k_0 - j \alpha</math> The wave expression is given by: <math>U = U_0 e^{-\alpha x} e^{j(\omega t - k_0 x)}</math></p>	<p>Both of these notations are correct; however, it depends on which direction is defined positive for vertical displacements of <math>X_3</math> (i.e. upwards <math>k = k_0 - j \alpha</math> and downwards <math>k = k_0 + j \alpha</math>). In this work, we always consider the positive direction of <math>X_3</math> upwards. The two wave expressions give different answers to problems. In order to have similar answers, we must consider <math>\varphi = \pi</math> to its initial form.</p>	<p>«English» literature: The wave is provided by: <math>U = U_0 e^{j(kx - \omega t)}</math> The wave vector is written by: <math>k = k_0 + j \alpha</math> The wave expression is given by: <math>U = U_0 e^{-\alpha x} e^{j(k_0 x - \omega t)}</math></p>
---	--	--

We can express the Newton's law by the fact that the force per volume unit ( $F_i/V$ ) related to the piezoelectric effect transmits the acceleration  $a_i$  to the density  $\rho$ , thus the particle motion  $u_i$  can be explained as follow in a volume unit:

$$\frac{\partial T_{ij}}{\partial X_j} = \rho \frac{\partial^2 u_i}{\partial t^2} \quad (3.6)$$

By giving the strain expression  $S_{kl}$  its expression in equation 3.3 (by applying the Voigt convention assuming than  $S_{kl} = S_{lk}$ ), and substitute it in equation 3.6, it can be easily obtained:

$$C_{ijkl} \frac{\partial^2 u_l}{\partial x_j \partial x_k} - e_{kij} \frac{\partial^2 \Phi}{\partial x_j \partial x_k} = \rho \frac{\partial^2 u_i}{\partial t^2} \quad (3.7)$$

Where  $\rho$  is the density and  $C_{ijkl}$  are the stiffness coefficients related to the Equation (3.3).

Analytically, the electrical variables that can describe a piezoelectric solid are the electric field  $E_i$  and the electric displacement  $D_i$ , respectively (equation 3.8). The electric displacement obeys the Poisson's equation, and therefore equation (3.9) can be obtained as follows:

$$E_i = -\frac{\partial\Phi}{\partial X_i} \quad (3.8)$$

$$\nabla^2\Phi = -\frac{\rho}{\varepsilon_0} \xrightarrow{\rho=0} -\frac{\partial D_j}{\partial X_j} = 0 \quad (3.9)$$

where  $\rho/\varepsilon_0$ , usually noted as  $\rho_e$  describes the density of free charges per unit volume and  $\varepsilon_0$  refers to permittivity. Therefore, the electric displacement of the equation (3.4) which variables have been extracted from the equations 3.8 and 3.9 respectively, and can be described as follows:

$$D_j = e_{jkl} \cdot S_{kl} + \varepsilon_{jk}^S \cdot E_k, \text{ where } E_k = -\frac{\partial\Phi}{\partial x_k}$$

$$\frac{\partial D_j}{\partial x_j} = e_{jkl} \frac{\partial^2 u_l}{\partial x_j \partial x_k} - \varepsilon_{jk} \frac{\partial^2 \Phi}{\partial x_j \partial x_k} = 0 \quad (3.10)$$

An insulating solid such as quartz must satisfy the Poisson's equation, and therefore equation 3.9 has been set equal to zero since there is no electrical charge in our medium. Moreover, the amplitude of the particle displacement along the  $X_3$  direction may be neglected with respect to the wavelength (40  $\mu\text{m}$ ) and thickness of the guiding layer (4  $\mu\text{m}$ ), whilst the acoustic wave propagates in the  $X_1$  direction and the particle displacement is in the  $X_2$  direction.

### III.3 Analytical simulation modeling

In order to further examine the behavior of the GO sheets deposited on the LW devices and validate the theoretical analyses, a simple analytical approach was formulated based on LW phase velocity and the attenuation coefficient of the acoustic waves. Firstly, LW propagation in a viscoelastic surface layer is considered. In addition, it is assumed that all materials of the LW structure are isotropic and dense (non nano-structured), except the quartz substrate (anisotropic and dense). In this approach, in order to take into account, the damping of the acoustic wave due to the GO layer, a complex shear modulus is considered. The shear modulus  $G$ , as defined later in the FEM calculations, therefore describes the complex shear modulus, thus  $G^* = G' + j G''$  of the GO viscoelastic layer.  $G'$  is the shear modulus of the material (also called storage shear modulus), and  $G''$  is the loss moduli which is expressed by the relation  $G'' = \omega \eta$ , with  $\omega$  the pulsation, and  $\eta$ , the viscosity of the medium in Pa.s. For a pure elastic film without losses  $G'' = 0$ .

Thus, the wave vector  $k_i$  introduced in equation (3.5) for the expression of the particle displacement becomes complex since the propagation occurs in a viscoelastic medium and can be described as  $k = k_0 - j \alpha$ , where  $k_0 = 2 \pi / \lambda$  with a wavelength  $\lambda = 40 \mu\text{m}$ . The angular frequency is equal to  $\omega = k_0 V$ , where  $V$  represents the wave phase velocity in m/s, since it derives from the real part ( $k_0$ ) of the wave vector  $k$ . Based on the set of equation given by equation (3.7) and equation (3.10), we apply the same calculation approach carried out by Céline Zimmerman [6]. The difference in our specific case is that we take into account a complex shear modulus for the GO layer, and a complex wave number. Thus, we obtain the complex and nonlinear dispersion relation given by equation (3.11):

$$k \chi_h h - \arctan\left(\frac{C_{44} \chi_s}{\mu_{hs} \chi_{hs}}\right) + \arctan\left(\frac{G_b^* \chi_b \tan(k \chi_b b)}{\mu_{hs} \chi_{hs}}\right) = 0 \quad (3.11)$$

with the  $\chi_s$ ,  $\chi_{hs}$  and  $\chi_b$  defined by the following ways:

$$\text{in the substrate: } \chi_s = C_a \sqrt{1 - \frac{V^{*2}}{V_s^2}};$$

$$\text{in the guiding layer: } \chi_{hs} = \sqrt{\frac{V^{*2}}{V_{hs}^2} - 1};$$

$$\text{in the sensitive layer: } \chi_b = \sqrt{\frac{V^{*2}}{V_b^2} - 1};$$

$$V_s = C_a \sqrt{\frac{C_{44}}{\rho_s}}; V_{hs} = \sqrt{\frac{\mu_{hs}}{\rho_{hs}}}; V_b = \sqrt{\frac{G_b^*}{\rho_b}}; C_a = \sqrt{\frac{C_{66}}{C_{44}} - \frac{C_{46}^2}{C_{44}^2}}$$

where  $G_b^*$  is the complex shear modulus and  $\rho_b$  is the density of the GO structure defined as an over-layer on the top of the guiding layer. In order to have a simple dispersion equation we present  $V^* = \omega/k$  as a complex term (homogeny to velocity, the real part of this expression is the Love wave phase velocity). Similarly, the subscripts hs, s and b stand for the material properties of the guiding layer (SiO<sub>2</sub>), the substrate (AT-cut quartz) and the sensing layer (GO), respectively.  $C_{44}$ ,  $C_{46}$  and  $C_{66}$  are the elastic constants of the quartz substrate which have a contribution to the pure shear horizontal displacement of the particle. Finally,  $\mu_i$  and  $\rho_i$  represent the storage shear modulus and the density of the material, respectively. Then, referring to the method of numerical calculation of [3]-[4], the complex dispersion Equation (3.11) can be written as:

$$F(k, G_b^*, \omega, \rho_b, \rho_{hs}) = 0 \quad (3.12)$$

where F is identical to left side of equation (3.11). The quantities  $\rho_b$ ,  $\rho_{hs}$  and  $\omega$  in equation (3.12) are real, while quantities k and  $G_b^*$  are complex. Then, treating the quantities  $\rho_b$ ,  $\rho_{hs}$  and  $\omega$  in equation (3.12) as parameters and the quantities k and  $G_b^*$  as variables, as similarly expressed in [5]. If it is further assumed that the amplitude of the surface wave diminishes very slowly as it travels, then the dispersion equation (3.11) can be expanded into the Taylor series about the point  $(k_0, G')$  with respect to small increments  $(\alpha, G'')$  [5]. By taking the linear terms of the Taylor series, it is obtained the real part of the dispersion equation (3.11), already expressed in [6] and the imaginary part that leads to the attenuation of the Love waves, which is linear to the viscosity. Neglecting terms higher than linear, a new approximate dispersion equation can be obtained:

$$F(k, G_b^*) \approx F(k_0, G') + \frac{\partial F}{\partial k} \Big|_{k=k_0, G_b^*=G'} \cdot j\alpha + \frac{\partial F}{\partial G_b^*} \Big|_{k=k_0, G_b^*=G'} \cdot jG'' = 0 \quad (3.13)$$

where  $G'' = \omega\eta$ . The partial derivatives in equation (3.13) are calculated at the point  $(k_0, G')$  for given values of the parameters  $G_b^*$ ,  $\rho_b$ ,  $\rho_{hs}$  and  $\omega$ . The solution of equation (3.13) requires that

both real and imaginary parts be set equal to zero. By equating to the zero real part of equation (3.13) and under  $k=k_0$ ,  $G_i^* = G_i$  substitutions we have:

$$k_0 \chi_h h - \arctan \left( \frac{C_{44} C_a \sqrt{1 - \frac{w^2 \rho_s}{k_0^2 C_a^2 C_{44}}}}{G_{hs} \chi_h} \right) + \arctan \left( \frac{G_b \sqrt{\frac{w^2 \rho_b}{k_0^2 G_b} - 1} \tan \left( k_0 \sqrt{\frac{w^2 \rho_b}{k_0^2 G_b} - 1} b \right)}{G_{hs} \chi_h} \right) = 0 \quad (3.14)$$

By equating to zero the imaginary part of equation (3.13) and under  $k=k_0$ ,  $G_b^* = G'$  and  $\omega \eta = G''$ , we obtain:

$$\alpha = \frac{-G'' \cdot \frac{\partial F}{\partial G_b^*} \Big|_{k=k_0, G_b^*=G'}}{\frac{\partial F}{\partial k} \Big|_{k=k_0, G_b^*=G'}} \quad (3.15)$$

All quantities in equation (3.15) are real. Equation (3.14) is identical with the dispersion equation for Love wave in loss-less media. Performing calculations in equations (3.14) and (3.15), it can be obtained an analytical formula (see Appendix C - Chapter III - Maple calculations) for the normalized attenuation coefficient of the Love wave  $\alpha h$ , as a function of the normalized propagation constant of the Love wave  $k_0 h$ , and represents that the attenuation coefficient of the Love wave is directly proportional to the imaginary part of shear modulus  $G_b^*$ .

### III.4 Numerical (FEM) modeling

Comsol Multiphysics® offers plenty of capabilities regarding the simulation of SAW devices; it is possible to realize simulations of the piezoelectric media that require the complete set of fundamental equations in relation to the mechanical and electrical phenomena. In general, the procedure for simulating Love wave devices using the FEM is the following: 1) the 3D model of the device is build using a computer-aided design (CAD) software; 2) the 3D model is imported to a commercial finite element software, which allows piezoelectric analysis; 3) the material properties of the involved materials are introduced in the software; 4) the convenient piezoelectric finite element is selected; 5) the model is meshed with the selected finite element and 6) the simulation is run in the software. As result the software obtains the particle displacements and voltage at every node of the model. Thus, setting up particular model conditions focused on the Love wave devices, allows the user to control various standards of piezoelectricity and the acoustic wave displacement components.

Although FEM simulations are extremely useful tools for studying Love wave devices, the numerical simulations in real size are still a challenge. Delay lines in practice are of many wavelengths and to simulate them would require having too many finite elements. For these reasons, in order to achieve simulations able to reproduce real cases, it is necessary to downscale the dimensions of the simulated Love wave devices compared of real ones. Otherwise, it would



consume excessive computational resources and any simulation results would not have been able to realize the theoretical premises of this work.

The Table 3.2 summarizes the main feature characteristics of the simulated and fabricated Graphene - Love wave sensors, respectively. The simulated dimensions have been sized concerning the aspect ratio of the real device and its boundary conditions. For example, the number of the IDTs is two times smaller than the actual fabricated device, so there are differences on the device's bandwidth (simulated). Short IDT and Lcc lengths impact the acoustic wave propagation that leads to a twice as large bandwidth on the simulated device [7]. Another limitation of the FEM simulation was that reflections of the quartz excitation were closely interrelated at the output responses of the sensory device. Therefore, the output IDTs had to be selected manually and noted as a domain (separately) in order to encounter such difficulties. However, many improvements were realized from previous FEM modeling analyses, especially that of remodeling adaptations towards previous versions of Comsol © (v.4 to v.5.2). Another significant advantage was the reduction of the calculation time from days to hours. Moreover, the addition of a highly-tuned meshing area, that is of a sensing graphene oxide mono-layer was able to provide responsive and representative results in the literature [7]-[8] towards allowing the extraction of GO's mechanical parameters (Young's and shear moduli).

Table 3.2: Summarizing the main feature characteristics towards simulated and fabricated devices, respectively.

	Substrate		Guiding layer		Sensitive layer		IDTs	
Materials	AT cut Quartz		Silicon dioxide - SiO <sub>2</sub>		Graphene oxide - GO		Au	Au/Ti
Conditions	Simulated	Fabricated	Simulated	Fabricated	Simulated	Fabricated	Simulated	Fabricated
Length (μm)	2150	24224	2150	24224	300 - 2150	6570 - 10160	1750	3590
Width (μm)	800	5600	800	5600	800	2400	2x88 IDTs	5x88 IDTs
Thickness (μm)	80	500	4	4	0.02 - 0.9	0.09 - 0.437	0	0.11-0.14

The Love wave device structural model composed of this FEM consists of three simulation segments, a) the AT-cut quartz substrate (Euler angles: 0°; 121.5°; 90°), thus allowing the horizontal transverse polarization of the acoustic waves; b) the guiding layer of isotropic SiO<sub>2</sub>, where the propagation of the acoustic waves is confined within and c) the Au transmitter-emitter (IDTs) to generate and receive the acoustic waves, respectively. The model structure is represented in Figure 3-2. In particular, 2D - massless electrodes are assumed for the transmitting and receiving IDTs in order to avoid the mass loading effect regarding the geometrical aspects of the fabricated Love wave device. The IDTs are composed of 44 split-finger pairs of gold with a wavelength  $\lambda$  (spatial periodicity) equal to 40μm. Split-fingers are electrically placed as ground and RF potential, alternatively, as represented in Figure 3-3. The acoustic aperture (W) and the

center-to-center distance of transmitting and receiving IDTs ( $L_{cc}$ ) are equal to respectively  $40\lambda$  and  $210\lambda$ . Analytically, the electric potential is applied to the left side (input) IDTs, in order to generate the Love wave through the reverse piezoelectric effect. Indeed, an applied voltage across the faces of the cut produces shear stresses with the crystal.

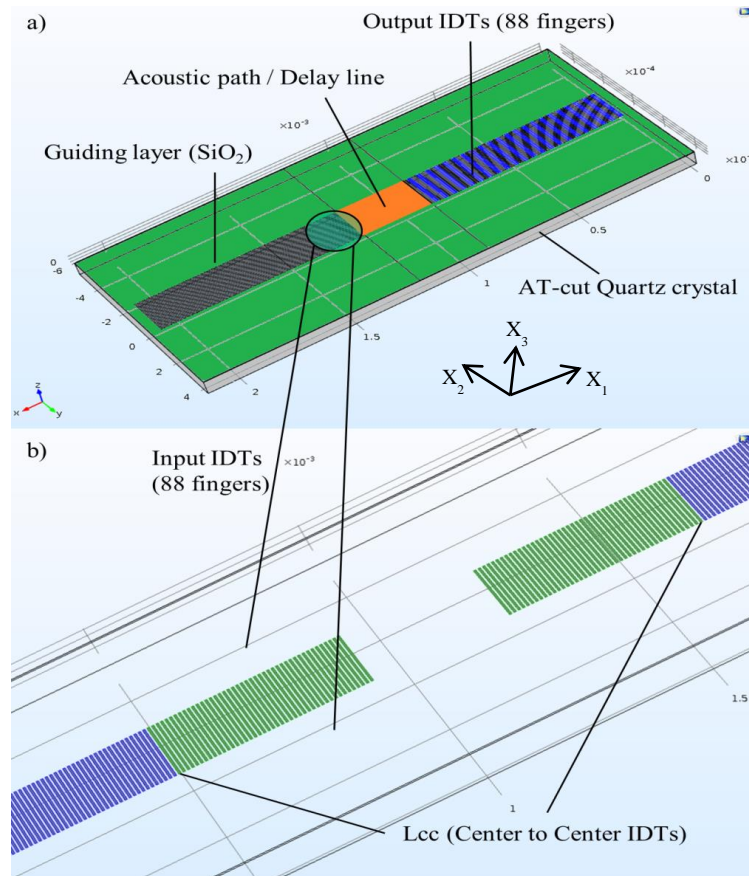


Figure 3-2 (a) Love wave sensor design in Comsol Multiphysics and (b) its extended magnification on the center-to-center distance between IDTs.

This work considers the vibration of an AT-cut quartz, focusing on the mechanical response of the system with respect to the time domain variations. The acoustic wave propagates in the  $X_1$  direction with the maximum of its energy confined in the guiding layer ( $\text{SiO}_2$ ). After a certain time, commonly named delay time, the acoustic wave reaches the output IDTs and it is converted into an electrical signal through the direct piezoelectric effect. As the IDTs of the fabricated Love wave device are periodic, similar boundary conditions can be applied to the boundaries of the transmitting IDTs. Analytically, the following excitation has been applied to the input IDTs, as represented in Figure 3-3. The pulse has a width of 4 nanoseconds and a potential of  $V_+$  and  $V_-$  alternately, in the frequency of 117 MHz.

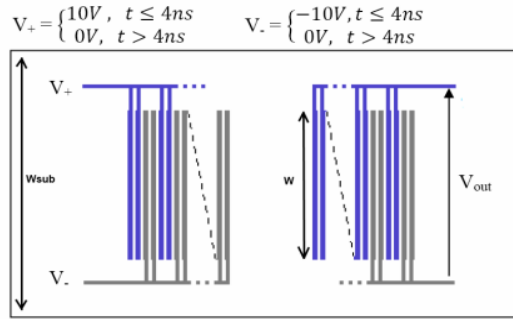


Figure 3-3 Illustration of the impulsive excitation of the emitter IDTs, and the measurement of the output voltage of the receiving IDTs.

Nevertheless, the domain analysis of the Love wave sensor is generally performed in three stages. Firstly, following the electrical excitation of the emitting IDTs, Figure 3-4 shows the wave progression on the simulated device, thus depicting the operating device at 166 ns. The Total Displacement (TD) is plotted accordingly, which corresponds to the longitudinal, shear horizontal and shear vertical polarization  $u$ ,  $v$  and  $w$  respectively, as written in the equation 3.16:

$$TD = \sqrt{u^2 + v^2 + w^2} \quad (3.16)$$

The intensity of the acoustic wave displacement has been plotted at the time frame of 166 ns, as illustrated in Figure 3-4.

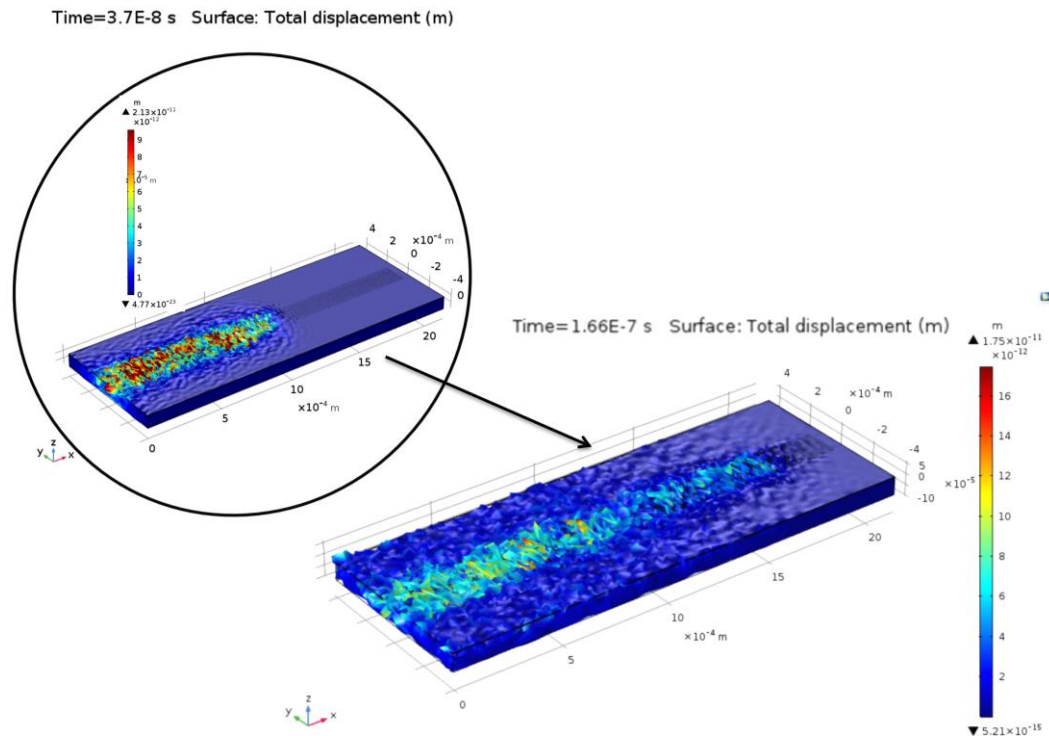


Figure 3-4 Illustration of the wave propagation on the guiding layer and the output IDTs based on the total displacement of the structure at 166 ns.

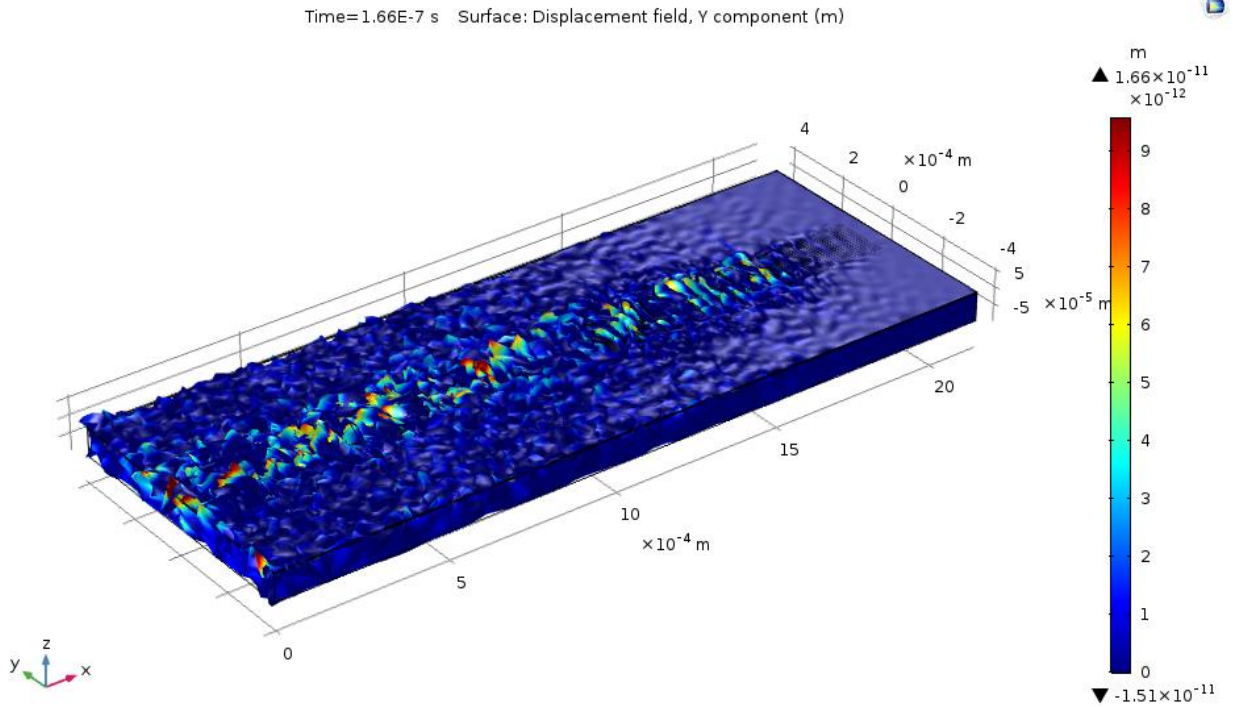


Figure 3-5 Shear horizontal component of the Y - displacement (positive part).

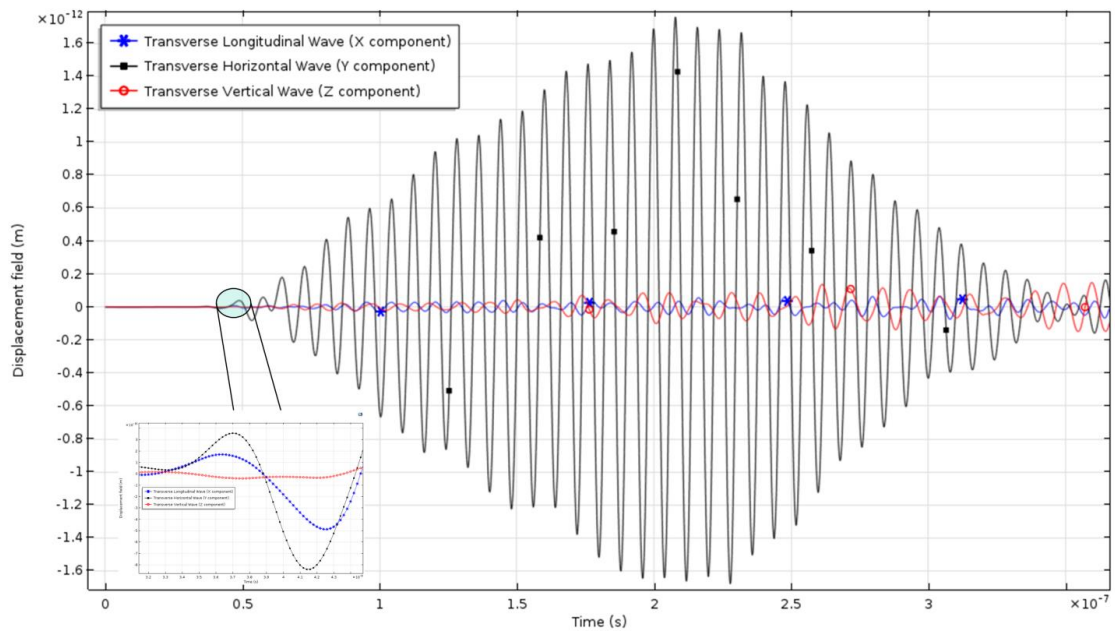


Figure 3-6 Displacement components measured on the alternate split fingers of the receiver IDTs.

By plotting the positive part of the shear horizontal component of the displacement, as depicted in Fig. 3-5, the generated acoustic wave can be observed in an appropriate way. The mechanical deformation due to the propagation of the wave is measured at alternate split fingers of the receiver IDTs. The total Longitudinal (LG), Shear Horizontal (SH) and the Shear Vertical (SV) displacement components are plotted in Fig.3-6 with respect to time. Moreover, the amplitude of

the SH displacement is greater than the longitudinal and SV components. This result verifies that the generated wave is a Love wave. The maximum amplitude of the measured displacement is around 1.6 pm. The delay time (37 nanoseconds) before the appearance of the amplitude displacement corresponds to the time that the wave takes to travel from the emitting to the receiving IDTs. Then, by measuring the amplitude of the Love wave across the entire geometry of the device (cross section), the location of the confined energy can be estimated accordingly. Figure 3-7 shows the wave penetration depth within the substrate and the guiding layer (GL), in which the amplitude of the acoustic wave is close to zero at a depth of  $40 \mu\text{m} \approx \lambda$  (substrate) and confines itself at  $80 \mu\text{m}$  (substrate's thickness) in the guiding layer.

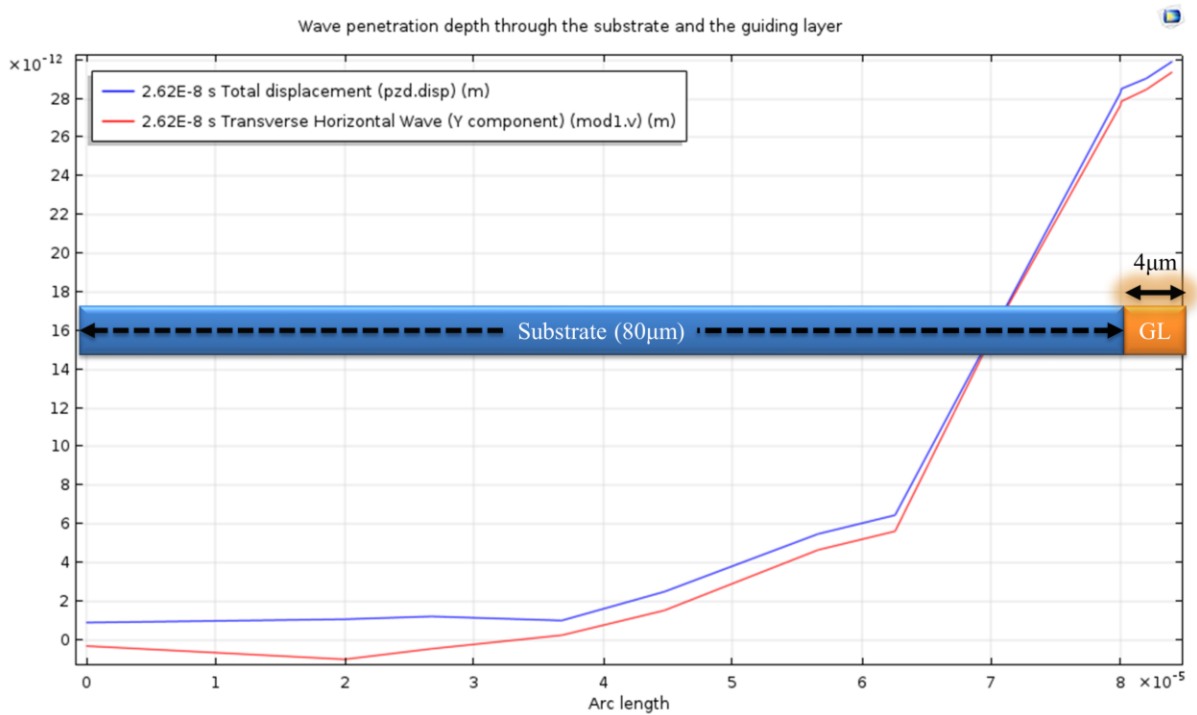


Figure 3-7 Wave penetration depth through the substrate and the guiding layer.

Finally, the electric potential was calculated with respect to time by using the surface average method (FEM) and compared with the experimental measurements from the oscilloscope. Analytically, waveforms of the bare Love wave devices and the driving output voltages were recorded using a digital oscilloscope Lecroy. The number of the experimental data points, obtained by sampling interpolated values with a time step of 700 ns. Subsequently, equivalent time domains were selected to compare if the theoretical waveforms are in agreement with the experimental ones, as represented in the Figure 3-8. This comparison allows observing differences between the simulated and fabricated waveforms and shows that the order of magnitude towards  $L_{cc}$  (center to center IDTs) plays a significant role to our analysis. According to the Table 3.2, the  $L_{cc}$  corresponds to  $29.375 \lambda$  and  $209.125 \lambda$  for the simulated and fabricated devices, respectively. Figure 3-8 provides the theoretical and experimental responses of a shape similar towards amplitude perspective; however clear diversification on a time scale can be observed due to  $L_{cc}$  distance variations on the acoustic wave propagation.

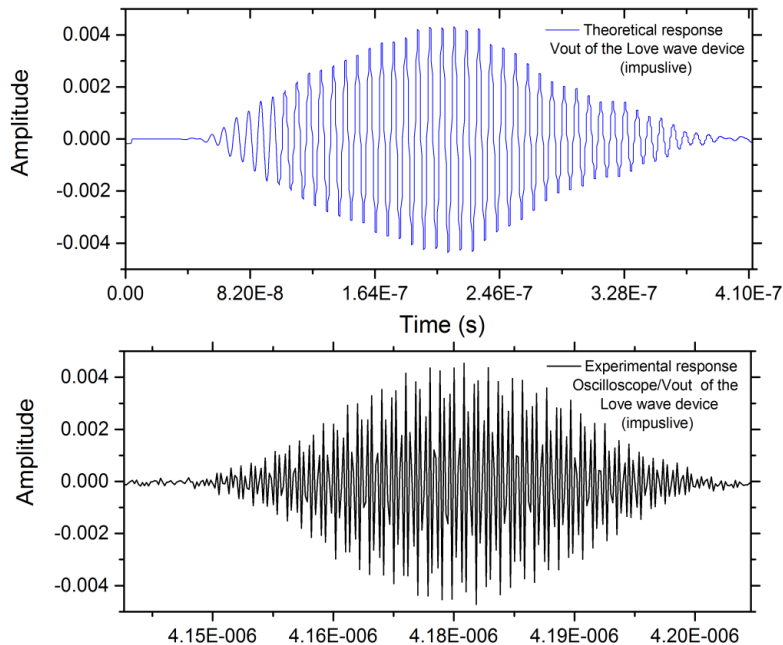


Figure 3-8 Theoretical and experimental electric potential of the Love wave device recorded at the receiver IDTs.

Following the numerical simulation analyses, a particular method has been applied, by means of a Fast Fourier Transformation (FFT). To characterize the received signals, all transformed from the time domain to the frequency domain by using discrete FFT analysis. This process allowed easier comparisons towards experimental responses obtained by VNA. The time domain analysis exported from Comsol transformed by using the equation 3.17:

$$X_k = \sum_{n=0}^{N-1} x_n e^{-i2\pi \frac{k}{N} n} \quad (3.17)$$

where:  $X_k$  is the amount of signal at frequency  $k$  in the output signal based on its amplitude and phase (complex number),  $n$  is the number of samples, starting from zero up to  $N-1$ ,  $x_n$  is the time domain signal and  $k$  is the current frequency under consideration from 0 Hz up to  $N-1$  Hz.

### III.5 Results and discussion: Application to the numerical and analytical simulations

During the past years, there has been an inconclusive debate about the atomic structure of GO, since it is rather complicated. It has been recently shown that the ordered GO sheets possess larger Young's modulus (380 - 470 GPa) and intrinsic strength than the amorphous GO (290-430 GPa) [9]. Suk et al. used Atomic Force Microscopy (AFM) measurements combined with Finite Element Method (FEM) calculations and considered one, two and three overlapped layers of GO, thus reporting that a GO monolayer has Young modulus of a  $207.6 \pm 23.4$  GPa [2]. Along similar lines, Paci et al. calculated the Young modulus of the GO structure near 670 GPa through Molecular Dynamics (MD) simulation, considering short Van der Waals distances ( $3.4 \text{ \AA}$ ) between the GO layers [10].

The following section is an attempt to address the critical issues of the mechanical properties of GO and investigate the most common uses of GO composites in order to encapsulate graphene

derivatives within the fabrication technologies. Analytically, this sub-section provides information regarding the mechanical properties of Inkjet-Printed ordered GO sheets deposited on  $\text{SiO}_2$  and highlighting the wave-guide properties of the GO/ $\text{SiO}_2$  composites, focusing on the lossy mechanisms of the viscoelastic and gravimetric effects. Before computing mechanical properties of the GO sheets, it is essential to provide information about the geometrical characteristics of the coated LW devices, as illustrated in Figure 3-9. The FEM modelling computations of the GO coated LW devices were performed with the solid mechanics interfaces of the structural mechanics module.

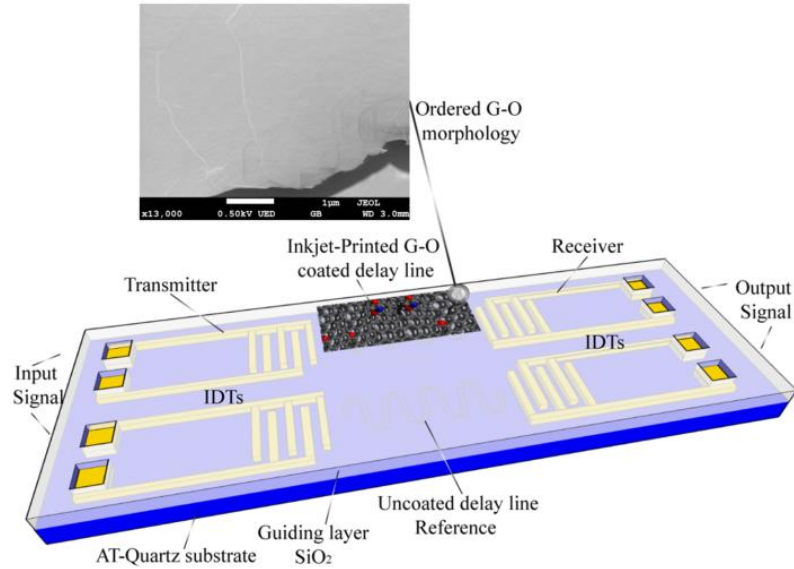


Figure 3-9 Visualization of the Inkjet-Printed GO coated LW devices.

Further, the shear modulus without viscous losses  $G$  was calculated through the following relationship [11]:

$$G = \frac{E}{2(1+\nu)} \quad (3.18)$$

where  $E$  is the Young's modulus, and  $\nu$  is the Poisson's ratio. These parameters are commonly found in tables or material data of Comsol Multiphysics<sup>®</sup>, but not for the GO based structures.

Initial FEM analyses have shown that without taking account the shear modulus  $G$ , a significant difference can be observed towards lossy material approximations. Moreover, four different devices were simulated under similar FEM conditions, especially focused on graphene sensitive coatings to provide a GO thickness investigation. Regarding the mass loading effect of the four graphene sensing layers, the model shows good agreement with the experimental results, since the attenuation of the devices increases with the thickness of graphene-based coatings, as represented in the Figure 3-10 below. It is worth noting that the viscoelastic properties of the graphene layers have an additional effect on the behavior of the coated Love wave devices, especially at higher thickness level. The modelling part of this state is not particularly suitable for the prediction of multi-layer graphene coated devices, regarding its mechanical properties. Besides, the addition of the graphene sensing layers enhanced the acoustic wave propagation and no heavy losses were added, as could be seen in the case of polymers used as sensitive materials

[3]. This theoretical approximation can be sufficiently improved to merit any further viscous losses, as it will be discussed later. Along similar lines, a frequency response analysis is performed for the transmitting IDTs with a synchronous frequency at 116 MHz, approximatively. The minimum of insertion loss, in terms of attenuation, was found at -30.34 dB and -31.02 dB for the theoretical and experimental results, respectively. For the bare devices (pure Love wave platform), the experimental scattering parameters have shown a good agreement with the modelling results, as represented in Figures 3-10 and 3-11, respectively.

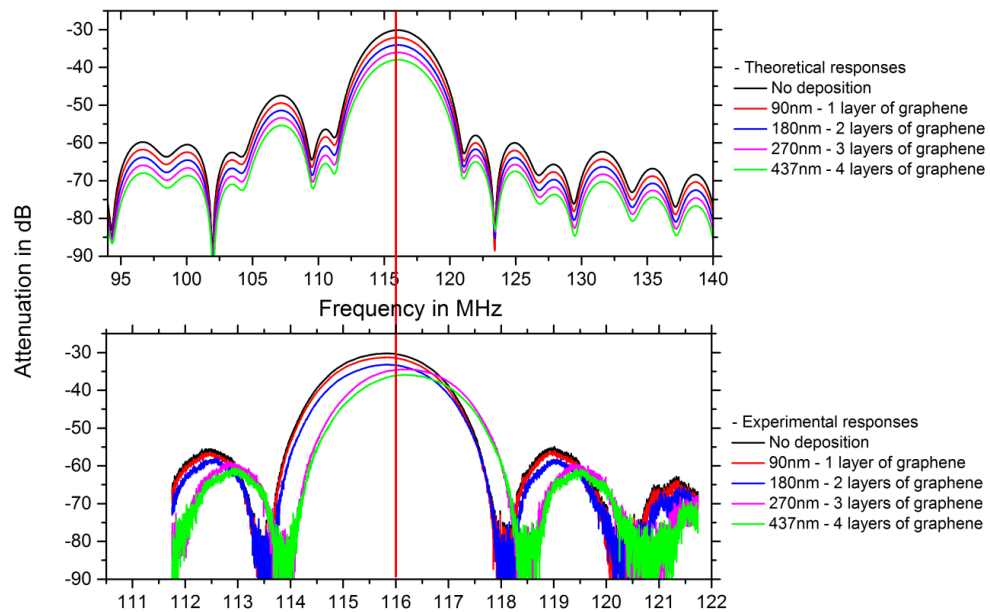


Figure 3-10 Theoretical and experimental attenuation of the bare and coated Love wave devices.

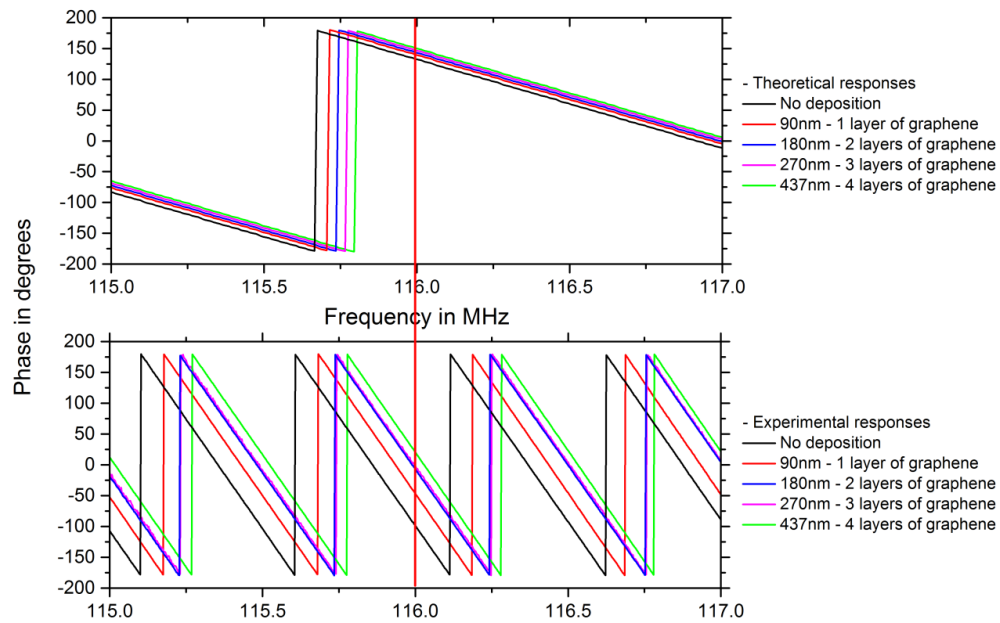


Figure 3-11 Theoretical and experimental phase of the Love wave recorded at the receiver IDTs.



However, the shift in frequency of these findings underlines the need for further improvement of the accuracy of the FEM analysis at the level of an operational shear modulus  $G$ , similar to the responses of the fabricated GO-LW devices. With this in mind, novel FEM simulations were realized towards better approximations to estimate the concurrent value of the GO shear modulus. The data collected here (Table 3.3) and the optimization towards FEM analyses has shown that there is compelling evidence of a correlation between the mechanical properties of GO sheets and higher operating device frequencies. Regarding the simulation of the sensor device, the FEM semi-empirical modelling considers GO, as a linear viscoelastic material (certain thicknesses). The theoretical scattering transmission characteristics have been reported in Figure 3-12 top panel and show convergence to the experimental characterization results (Figure 3-12 bottom panel), thus it was possible to extract useful information regarding the electro-mechanical properties of the GO sensing material.

Samples*	No. of GO passes	Attenuation - $S_{21}$ (dB) / Fabricated device	Attenuation - $S_{21}$ (dB) / Simulated FEM device
R40A10	4 - between IDTs	6.02	2.07
R40A12	6 between IDTs	9.41	4.15
R40A11	10 - between IDTs	14.78	6.09
R40A13	4 - whole device	5.25	2.19

Table 3.3 VNA - Electrical characterizations\*. Inkjet-Printed GO coated LW device characteristics.

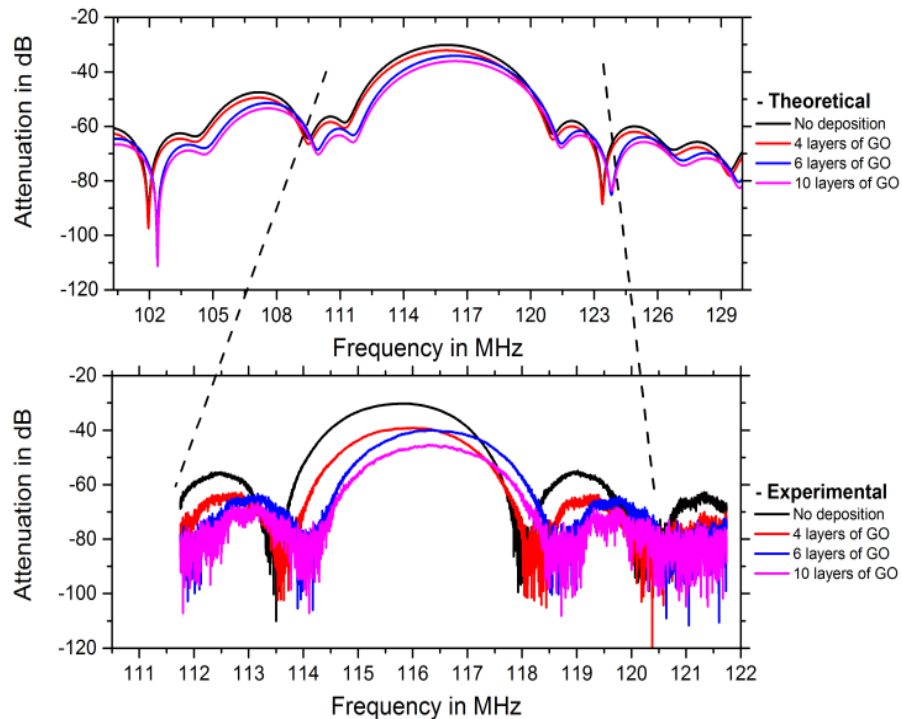


Figure 3-12 Theoretical (FEM) and Experimental  $S_{21}$  parameters of the bared and GO LW devices, respectively.

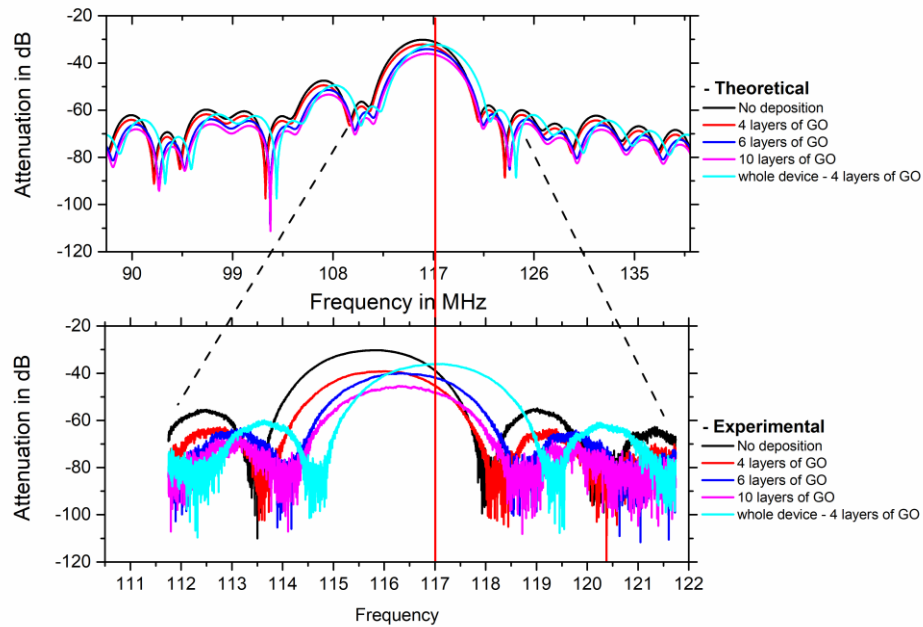


Figure 3-13 Theoretical (FEM) and Experimental  $S_{21}$  parameters of the bared and GO LW devices, respectively.

There are several techniques designed to analyze the viscoelastic aspects of the material behavior empirically, such as the generalized Maxwell's model (see Appendix C - Chapter III - Comsol calculations). As represented in the Figure 3-13, the whole area of the device is covered by GO material, which is considered as a linear viscoelastic solid where its state acts to remember or 'memorize' previous deformations that influence the present behavior. The FEM analysis results confirm that the mechanical properties of the Inkjet-Printed GO sheets report Young's modulus and Poisson's ratio equal to  $470 \pm 1.7$  GPa and 0.197, respectively, which are consistent with the current literature [9], [12]. By using equation (13), the calculated shear modulus is equal to  $G = 195.83 \pm 1.7$  GPa. In general, the verification of FEM approximation showed good convergence between theoretical and experimental frequency data.

Regarding the analytical modeling approach, the shear modulus  $G$  of the numerical FEM analysis has been imported to the analytical approximation as  $G'$  (real part of the equation  $G^* = G' + j G''$ ) to provide further investigation of attenuation coefficient  $\alpha$  (from which we can deduce the insertion losses). As illustrated in the Figure 3-14, analytical simulation data were not able to fit exactly on the experimental losses towards different viscosities. One possible explanation could be that as the GO layer thickness increases, the viscosity decreases, since the properties of the GO fabricated materials are dependent on the specific designated thicknesses, themselves intrinsically influenced by the material viscosity and Young's modulus. It has been previously reported that the Young's modulus generally decreases in higher GO thicknesses [9]. As demonstrated in Figure 3-14, five different GO coated LW devices (triangles) show that the GO viscosity decreases with higher thicknesses of GO sheets, thus providing essential information

regarding the rheological behavior of the GO. The reduction of the Young's modulus is modified due to the changes in basal plane stresses which are derived from different surface tension. Literature shows that a higher amount of the oxide sites increases the coverage of the functional groups [13], [14].

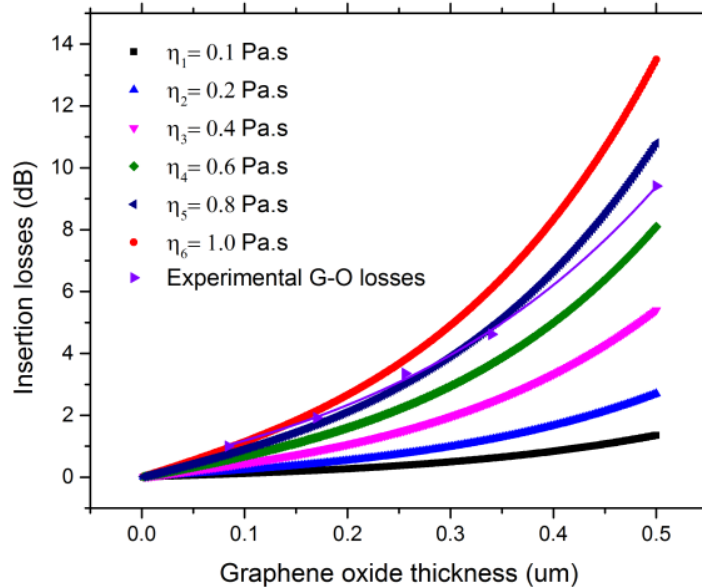


Figure 3-14 The analytical calculated attenuation coefficient versus the GO layer thickness, under different viscosity parameters and correlation between the experimental GO insertion losses (triangles) and their rheological behavior.

In summary, the correlation of the proportional viscosity ( $\eta$ ) with shear modulus ( $G$ ), and subsequently, with Young's modulus ( $E$ ) of the equation 3.18 was taken into account [15], which compensates low Poisson's ratio composites (0.197 was considered for numerical simulations - below 0.5). The particular unique viscoelastic properties of these GO sheets are related with the GO concentration, since accurate reproduction and stable GO inks have been reported for gas sensing applications [16]. Moreover, the GO dispersions may show biphasic behavior [17], since the experimental losses show clearly that different GO thicknesses permit a large variety of potential applications while making the preparation of high-tunable composite inks with multi-functional properties.

## References or Bibliography (if any)

- [1] A. E. H. Love, *A Treatise on the Mathematical Theory of Elasticity*. Cambridge University Press, 2013.
- [2] J. W. Suk, R. D. Piner, J. An, and R. S. Ruoff, “Mechanical properties of monolayer graphene oxide,” *ACS Nano*, vol. 4, no. 11, pp. 6557–6564, Nov. 2010.
- [3] W. Wang and S. He, “Theoretical analysis on response mechanism of polymer-coated chemical sensor based Love wave in viscoelastic media,” *Sens. Actuators B Chem.*, vol. 138, no. 2, pp. 432–440, May 2009.
- [4] P. Kielczyński, “Attenuation of Love waves in low-loss media,” *J. Appl. Phys.*, vol. 82, no. 12, pp. 5932–5937, Dec. 1997.
- [5] P. Kielczyński and J. D. N. Cheeke, “Love waves propagation in viscoelastic media [and NDT application],” in *1997 IEEE Ultrasonics Symposium Proceedings. An International Symposium (Cat. No.97CH36118)*, 1997, vol. 1, pp. 437–440 vol.1.
- [6] C. Zimmermann, D. Rebière, C. Déjous, J. Pistré, E. Chastaing, and R. Planade, “A love-wave gas sensor coated with functionalized polysiloxane for sensing organophosphorus compounds,” *Sens. Actuators B Chem.*, vol. 76, no. 1, pp. 86–94, Jun. 2001.
- [7] I. Nikolaou *et al.*, “Electro-mechanical properties of inkjet-printed graphene oxide nanosheets,” *Phys. Status Solidi A*, vol. 214, no. 3, p. 1600492, 2017.
- [8] I. Nikolaou, H. Hallil, V. Conédéra, J.-L. Lachaud, C. Dejous, and D. Rebière, “Enhanced properties of Love wave microsensors with Inkjet-Printed graphene oxide layers,” in *E-MRS 2016 Spring Meeting*, Lille, France, 2016, p. 1p.
- [9] L. Liu, J. Zhang, J. Zhao, and F. Liu, “Mechanical properties of graphene oxides,” *Nanoscale*, vol. 4, no. 19, pp. 5910–5916, Sep. 2012.
- [10] J. T. Paci, T. Belytschko, and G. C. Schatz, “Computational studies of the structure, behavior upon heating and mechanical properties of graphite oxide,” *J. Phys. Chem. C*, vol. 111, no. 49, pp. 18099–18111, Dec. 2007.
- [11] C. Multiphysics, *Structural Mechanics Module*. Reference Guide, Vers, 2008.
- [12] Q. Peng and S. De, “Mechanical properties and instabilities of ordered graphene oxide C6O monolayers,” *RSC Adv.*, vol. 3, no. 46, pp. 24337–24344, Nov. 2013.
- [13] W. Gao, L. B. Alemany, L. Ci, and P. M. Ajayan, “New insights into the structure and reduction of graphite oxide,” *Nat. Chem.*, vol. 1, no. 5, pp. 403–408, Aug. 2009.
- [14] W. Cai *et al.*, “Synthesis and Solid-State NMR Structural Characterization of <sup>13</sup>C-Labeled Graphite Oxide,” *Science*, vol. 321, no. 5897, pp. 1815–1817, Sep. 2008.
- [15] R. F. Landel and L. E. Nielsen, *Mechanical Properties of Polymers and Composites, Second Edition*. CRC Press, 1993.
- [16] I. Nikolaou *et al.*, “Drop-casted Graphene Oxide Love wave sensor for detection of humidity and VOCs,” *J. Integr. Circuits Syst.*, vol. 11, no. 1, pp. 49–56, 2016.
- [17] S. Naficy *et al.*, “Graphene oxide dispersions: Tuning rheology to enable fabrication,” *Mater. Horiz.*, vol. 1, no. 3, pp. 326–331, 2014.



## Chapter 4

### Vapor detection tests

## IV. Characterization of the GO - Love wave devices under different vapor

### IV.1 Introduction

The aim of this research was mainly focused into development of highly sensitive GO combined with the Love wave platform for environmental applications. Based on the literature review, the IMS-Bordeaux team, as well as the laboratories under collaboration (as mentioned in the Chapter I), made an informed decision to develop several novel graphene oxide nanostructured sensing layers that report higher performances according to the literature. Several alternative materials were compared with our devices such as polyaniline nanofiber based sensors, which reported NO<sub>2</sub> detection of 510 ppb at room temperature [1], or nano-porous SnO<sub>2</sub> and PANI layers showed a detection at 37 ppm of NO<sub>2</sub> at 140°C [2]. However, selecting highly specialized Love wave devices who work with universal microelectronic technologies ensures lower energy consumption [2] towards rapid detection applications [1].

Subsequently, for the NH<sub>3</sub> detections, there are plenty of cases that the developed Inkjet-Printed GO based Love wave devices in this thesis showed significantly higher performances than the reported literature, especially due to the original sensing layer synthesis composition and its good compatibility with the acoustic transducer. Analytically, the aforementioned devices were able to provide significantly lower detection limits towards NH<sub>3</sub>, such as Au/CNT-PANI (25 ppm) [3], SnO<sub>2</sub>/PANI (500 ppm) [4], functionalized SWNTs (400 ppm) [5] and Graphene/PANI (20 ppm) [6]. Regarding the humid detection limits, an interesting work shows that polyaniline/diamond coated devices were able to provide efficient sensing abilities, however the limit of detection was set at 11.3 % of RH [7].

It is worth noting that the IMS-Bordeaux team developed sensors were tested to a broad variety of gases and RH% to provide a wide range of environmental applications. By the necessity to detect limits in accordance with the emphasis on international target-setting of National Institute for Occupational Safety and Health (NIOSH – Table 4.1 in section IV.3.2) at sub-ppm level exposures, several vapor concentrations were prepared to contemplate detections of humidity (LoD: ~2 % RH - H<sub>2</sub>O), nitrogen dioxide (LoD: 0.025 ppm - NO<sub>2</sub>), carbon dioxide (LoD: 300 ppm - CO<sub>2</sub>), ammonia (LoD: 0.030 ppm - NH<sub>3</sub>), ethanol (LoD: ~80 ppm - C<sub>2</sub>H<sub>6</sub>O) and toluene (LoD: 100 ppm - C<sub>7</sub>H<sub>8</sub>), respectively.

Physical and chemical adsorptions were recognized successfully, especially for the humidity detection mechanisms, since a particular model was fitted on the experimental results. At this step, it was essential to fully understand the non-monotonically variations regarding the cross-sensitivities of the multi-coated Love wave devices. Thus, investigating the specific high performances of the RH detections led us to a peculiar identification of the vapor detection mechanism of the target analytes. Notably, according to the obtained sensing performances, the gas and humid sensing mechanisms will be discussed analytically on this chapter. This part of

the research has provided many novel outcomes and contributions to the body-knowledge in the field of nanostructured materials towards humid and environmental sensing applications.

## IV.2 Gas line experimental setup

Regarding the gas line characteristics, low, medium and high concentration sequencing vapors were flown over the GO-Love wave devices. The vaporizer equipment is composed of a part based on saturator providing the generation of a vapor in a given concentration and a given flow rate. A dilution stage is taking place in order to adjust the concentration of the vapor in a carrier gas (Nitrogen) and also the control of the “speed” (pressure) of the dilution. Following the principles according to the Figure 4-1, the influence of the critical temperature on the vaporizer through the equilibrium thermodynamics law is that the system requires enough energy to be able to activate the liquid to gas phase transition. The saturator is providing the generation of a steam heated cylinder filled with the desired initial solution (RH or VOCs) in the liquid phase, which is circulated through nitrogen at a fixed flow rate. Thus, the fixed gas flow rate is related to the concentration that is generated from the saturator and it depends on the critical temperature. The generated concentration is certified by the manufacturer at a temperature and calibration data, and therefore corresponds to the desirable concentration that is planned. In order to have a variable concentration, a portion of  $N_2$  is driven from an alternative side of the vaporizer and it has been used for the dilution of the original solution, after the phase transition. Finally, by adjusting the amount of the nitrogen with a Mass Flow Controller (MFC), the resulting concentration is controlled.

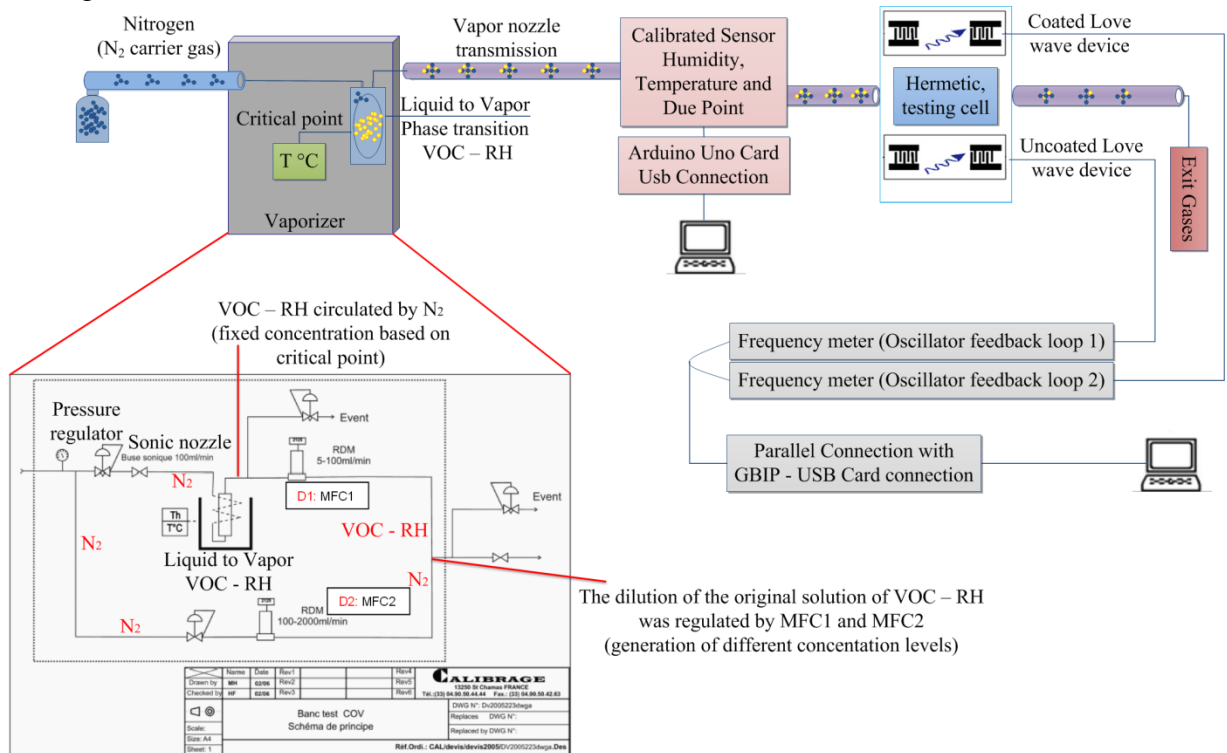


Figure 4-1 Experimental setup of the gas line measurements.



## IV.3 Drop – Casted GO sensor performances

### IV.3.1 Detection of humidity

The data gathered in the pilot study of GO based devices (Drop-Casted) suggested that the valorization of GO as a sensitive layer was essential, since GO has attained a great deal of research interest in the literature due to its potential for chemical sensors dedicated for environmental applications [8]. This study was focused on the application related to the detection of low humidity levels [7]. Similarly, Fisair company fabricates battery products which include lithium and its compounds while maintaining very low dew points. The main goal on low dew point dehumidification is to prevent the lithium from absorbing the humidity from air, since water vapor acts as a catalyst, so any lithium exposed to humidity levels in excess of 1% results in poorer battery quality, reduced performance and shorter shelf life.

After the first trials to detect higher amounts of RH (50% or more), the detection limit of the Drop-Casted GO coated Love wave sensor was set to lower concentrations due to the capabilities of the device. As it shown in the Fig. 4-2, several humidity levels were applied to Drop-Casted GO device in order to examine the adsorption-desorption characteristics at a variety of RH levels.

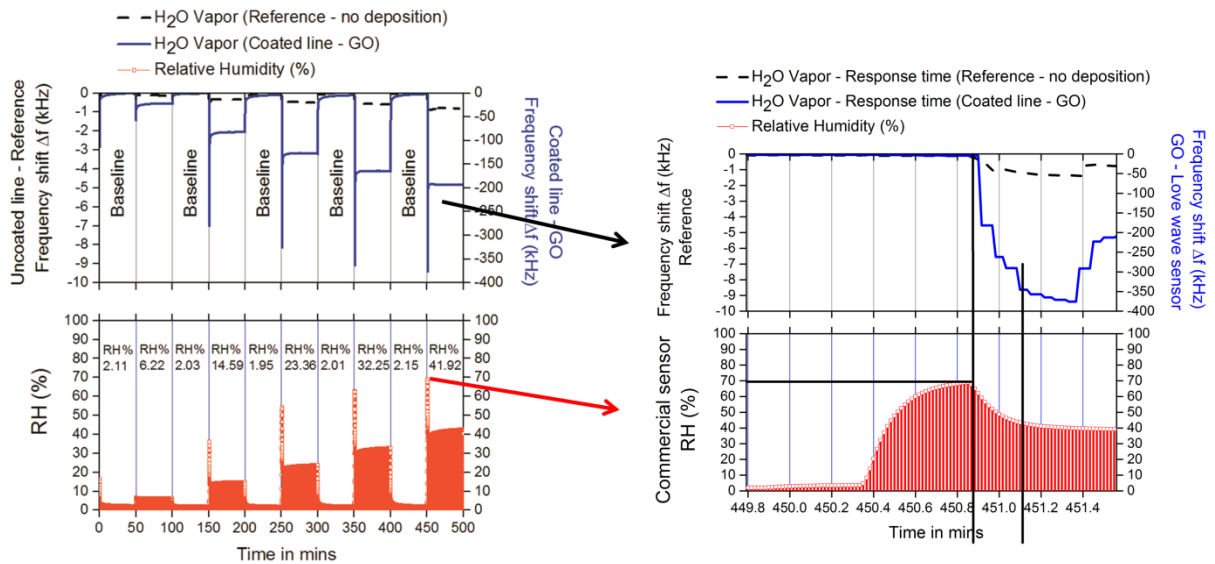


Figure 4-2 (a) Dynamic responses towards RH of the Drop-Casted GO based Love wave sensor (adsorption-desorption) and (b) its extended magnification at 41.92% of RH.

Analytically, the GO-Love wave devices are linked through the physical parameters of sensitivity and the frequency shift, which can be described as [9]:

$$Smf = \frac{1}{\Delta\rho_b b} \frac{\Delta f}{f_0} \quad (4.1)$$

where  $\Delta\rho_b$  corresponds to the density of the sensitive layer following the deviation of  $\rho_b + \Delta\rho_b$ , (higher density levels due to the adsorption of the analytes in the vapor state) and  $b$  is the

thickness of the sensing layer. Notably,  $\Delta f$  is the frequency shift based on the mass loading effect and  $f_0$  is the resonant frequency without mass loading effect. Our first approximation is based on the interpretation that the mass loading effect is considered by the sorption of chemical compounds and modifies only the density of the sensing layer (Equation 4). Based on the real-time detections of the GO-Love wave sensor, the sensitivities are extrapolated experimentally by:

$$S = \frac{\Delta f}{\Delta C} \quad (4.2)$$

where  $\Delta f$  is frequency shift and  $\Delta C$  represents the difference between the initial and the targeted concentration of the analytes. The influence of two different and subsequent exposures ( $\Delta C$ ) is directly correlated with the frequency shift  $\Delta f$ , which is mainly based on the deviation from the baseline. In addition, a baseline was selected near the detection limit of target analyte corresponding to the initial concentration of 2% for the humid based experiments. Standard deviation from the baseline provides useful information about the certainty of the compounds' detection and the estimated detection limit. The detection limit of an individual analytical procedure can be described as the lowest amount of analyte in a sample which can be detected but not necessarily quantitated as an exact value. Several approaches can be used for determining the detection limit of each analyte, however in this case the detection limit is determined by the analysis of samples with known concentrations of the target analyte and by establishing the minimum level at which the analyte can be reliably detected. Notably, calibration certificates of vapor generators PUL110 and PUL010 provided the amount of necessary information to prepare and calculate the desired ppm and sub-ppm concentration levels, respectively (Appendix Chapter IV - Theoretical and experimental calibration levels according to nitrogen dilutions; descending from ppm to sub-ppm concentration levels).

Furthermore, the sensitivity of Drop-Casted GO - Love wave device maintained within a useful range of RH, starting from 2.11 % up to 41.92 % (Figure 4-2 left side graph), with corresponding values of 32 kHz / 5 % RH. Likewise, Figure 4-2 represents good performances than alternative devices previously reported in literature [10], and in particular, higher amounts of RH detections can be observed in its extended magnification – 70 % of RH (Figure 4-2 right side graph). In addition, to establish reproducibility and reliability of the experimental conditions, a calibrated commercial humidity sensor was introduced during the vapor transmissions of RH (Fig. 4-1), thus reporting the RH, Temperature and Dew point values of the sensor devices. The aforementioned inception concept led to several clarifications regarding the RH measurements, since water vapors have the distinction of being the only component of air that regularly change between gas, liquid, and solid phases. Afterwards, considering that the air does not get saturated or partly saturated with water vapor, as well as the volume of space (GO sensing layer) can be saturated or partly saturated with water vapor, means that the degree of saturation depends on how many water molecules are in a volume of air and the temperature of the air. For these reasons, the values of the commercial sensor have been recorded in parallel at every subsequent cycle of humid vapor exposures. Moreover, higher amounts of RH, nearly at

70 % were measured due to the limitations of the vaporizer PUL110. Notwithstanding the limitations of the calibrated vapor generator, it can be clearly observed that both sensors, the commercial and the GO-fabricated ones, are in accordance at every single exposure of humid environments.

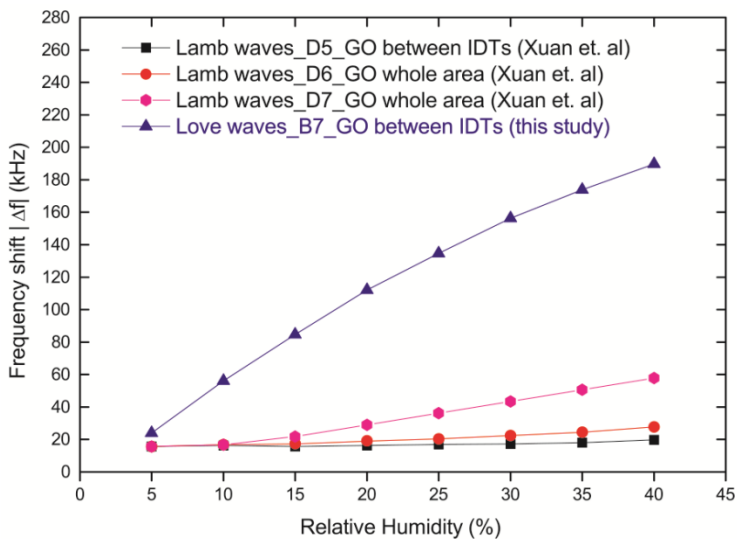


Figure 4-3 Humidity comparison responses of different acoustic wave devices (Lamb and Love wave sensors) based on GO; Lamb wave sensors are adapted from literature (Ref. [10]) and Love wave sensor from this study.

Interestingly, the frequency shift of Love Wave device B7 (Drop-Casted GO – R37B07 see Chapter II – IMS roadmap of Love wave devices) shown in Figure 4-3 demonstrates a saturation behavior which might be caused by the hysteresis of the sensor device, since RH approaches higher values in every subsequent cycle of the humidity vapor exposures (Fig. 4-2 - extended magnification). This interesting event, a hysteresis of the sensor device, it can be observed that the presence of the moisture in any given space is independent of the presence or absence of air in the same space of the GO sensing area, which is partly saturated with moisture. The scientific justification for the saturation of humid environments on the GO sensing area will be supported later on this chapter and proof of concept shall be provided. At the current state, a general description will be described that of the air that it may slightly retard the diffusion of the water vapor molecules, since it is essential to provide more experimental data and fitted modeling responses of the GO-Love wave sensors for more evidence.

In light of the evidence from this study, there is a better understanding of the amalgamation towards Love wave platform and graphene oxide sensitive material. Literary evaluations showed that higher sensory responses are premised on what is the ‘gilt-edged’: that is, a Love wave sensitivity privilege over the Lamb wave device, as well as towards alternative fabricated materials (CNTs, MIPs, TiO<sub>2</sub>, SiO<sub>2</sub>), respectively. The Drop-Casted coated devices, certain, showed high potential regarding the relative humidity detections, especially at very low concentration level compared to the literature [10]. Interestingly, this work clarifies the sensitivities between the Lamb and Love wave sensors and opens discussion towards GO sensitivities. For instance, the most sensitive device D11 of [10] Table 1, indicates that higher

GO thicknesses (200-300 nm) provide significant higher sensitivities than device D6 (GO thickness 70-90 nm), respectively. We have reported higher sensitivities under similar conditions that of (a) Deposition technique – Drop-Casting, (b) GO thickness and (c) Area of the GO depositions. Analytically, the device R37B07 of this work (GO thickness – 338 nm) is compared with the device D5 [10] (GO thickness – 200-300 nm), especially for area depositions between the IDTs. In order to justify better performances on the RH detections, except for the choice of the Love wave excitation, the Drop-Casted GO (R37B07) composition of this work indicates that in comparison with Raman spectra (Figure 2a) [10], the line shape of D and G lines are inhomogeneously broadened, as represented in the Figure 2-5 (a). Similarly, sharp peaks of the D and G lines indicate that the Inkjet-Printed GO composition of this work -i.e., Figure 2-19 (d) provided better homogeneity than the Drop-Casted GO. The main premises of inhomogeneous broadening peaks are usually related in solids, particularly in amorphous, in which the chemical composition, crystal size, molecular chain length and morphology can vary significantly. Thus, depicting such compositions may introduce defects that are able to provide higher sensitivities towards inkjet-printing and drop-casting deposition aspects [10].

Geometrically, the thickness of the sensitive layer and its covered surface by amorphous SiO<sub>2</sub> or TiO<sub>2</sub> and polymers (MIPs) should be controlled and limited due to the negative / lossy impacts on the devices. However, carbon-based materials (graphene oxide, CNTs, etc.) can be printed or dropped in large surface areas with high thicknesses, while not affecting the functionality of the device dramatically. This work uses experimental evidence to support this argument, provided that the author bears in mind the limitations of the previous methods used to obtain these results. It has been recently reported that there is a correlation between the possible number of adsorbed layers (water molecules) and the fraction coverage of GO [11]. In particular, the ability to adsorb moisture on the sensing layer is associated with the oxidation method of graphene solution [10]-[11]-[12], the length [10] and the thickness [11]-[12] of the coated layer.

That means that the presence of the GO sensing material is not delimited between the IDTs, thus there is a further investigation on the sensitivity enhancement parameters. This provides lots of functionalities and shows great potential for many useful usage scenarios, especially by prolonging the GO sensing area. As mentioned previously, the structural prolongation of carbon-based materials is allowed on Love wave devices, as it will be shown later for this platform. The geometrical amendment of the sensing layer provides exceptional capabilities on the GO surface area to further ameliorate the total adsorption phenomena of the water vapor molecules (high surface to volume ratio), which gravimetrically affect the sensitivities of the Love wave devices. Last but not least, in a manner of repeatability, the RH criteria evolution shared humid detections with reproducible measurements at wide range of concentrations, as illustrated in Fig. 4-4.

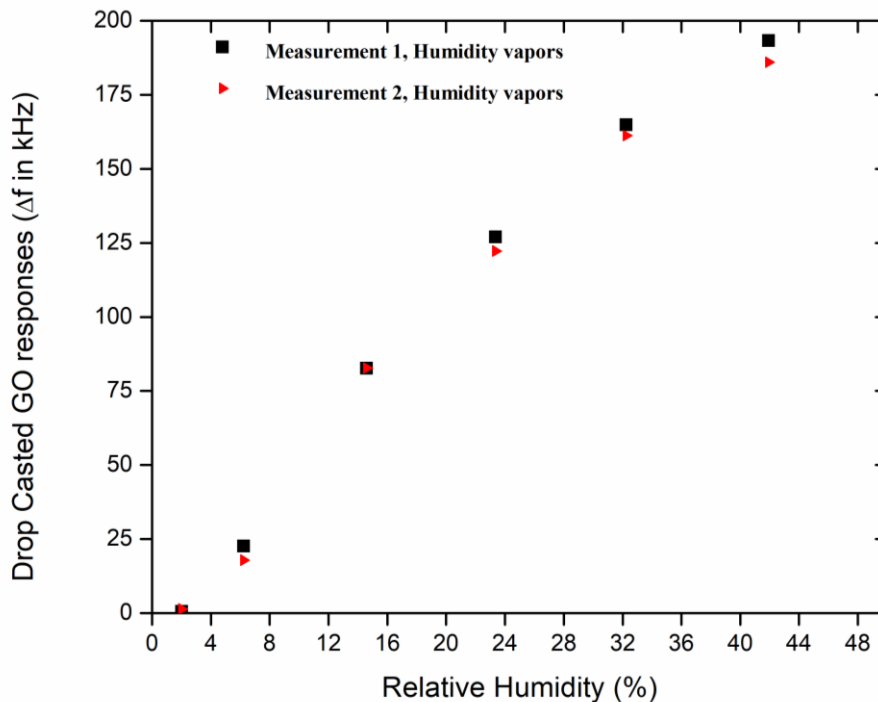


Figure 4-4 Reproducibility of the Drop-Casted GO Love wave device (R37B07) regarding the humidity exposures.

### IV.3.2 Detection of chemical compounds in a gaseous state

Regarding the Drop-Casted GO based Love wave devices under volatile exposures; the aim of this study was related to the exploration of the cross-sensitivities that GO coated devices reported at wide range of VOCs and toxic gases.

Particular ethanol exposures were introduced to GO coated devices through step sequencing concentrations followed by the NIOSH ceiling limits, which have been recently reported [13]. The Short-Term Exposure Limit (STEL) of  $C_2H_6O$  levels render device's detection limits below 1000 ppm (NIOSH Table 4.1 represents - standard ceiling limits < 1000 ppm for  $C_2H_6O$ ), as well as aiming at lower detection limits to further explore the Permissible Exposure Limit (PEL) below 750 ppm. A PEL is usually given as a time-weighted average (TWA), although some are short-term exposure limits (STEL) or ceiling limits. Since the TWA provides the average exposure over a specified period, usually a nominal eight hours, it was essential to investigate different time slots of volatile compounds based on a short-term exposure (50 mins). This necessity led the gas characterization measurements to commence at the lowest possible concentration level near 30 ppm with a step sequence of multiple concentrations of the target analyte ( $C_2H_6O$ ). The ethanol concentration levels have been started from 30 ppm (mixture with Nitrogen) up to 750 ppm.

Permeation rate (ng/min)	Molecular weight of C <sub>2</sub> H <sub>6</sub> O	K factor	Flow rate (ml/min)	Cinitial (ppm)	Cmin (ppm)	Cmax (ppm)	Substance	Exposure limits TWA (8 hours)	Exposure limits STEL / Ceiling (short - term)	Notations	CAS No
1446970	46.07	0.5309312	30.4	25271.1022	1.8719335	1579.44389	C <sub>2</sub> H <sub>6</sub> O	-	1000 ppm	-	64-17-5
at T = 61.3 °C											
Permeation rate (ng/min)	Molecular weight of C <sub>7</sub> H <sub>8</sub>	K factor	Flow rate (ml/min)	Cinitial (ppm)	Cmin (ppm)	Cmax (ppm)	C <sub>7</sub> H <sub>8</sub>	20 ppm	-	R	108-88-3
1645867	92.14	0.2654656	30.4	14372.4034	1.06462248	898.275213	Toluene	-	-	-	-
at T = 82.3 °C											
Permeation rate (ng/min)	Molecular weight of H <sub>2</sub> O	K factor	Flow rate (ml/min)	Cinitial (ppm)	Cmin (ppm)	Cmax (ppm)	H <sub>2</sub> O	-	-	-	-
1203256	18.01	1.3581344	30.4	53756.0306	3.98192819	3359.75191	Water	-	-	-	-
at T = 82.4 °C											
Permeation rate (ng/min)	Molecular weight of H <sub>2</sub> S	K factor	Flow rate (ml/min)	Cinitial (ppm)	Cmin (ppm)	Cmax (ppm)	H <sub>2</sub> S	-	Ceiling limit 10 ppm	-	7783-06-4
6800	34.0809	0.7177041	30.4	160.539064	0.01189178	10.0336915	Hydrogen Sulfide	-	-	-	-
at T = 30.0 °C											
Permeation rate (ng/min)	Molecular weight of NO	K factor	Flow rate (ml/min)	Cinitial (ppm)	Cmin (ppm)	Cmax (ppm)	NO	25 ppm	-	-	10102-43-9
14950	30.01	0.8150616	30.4	400.828013	0.02969096	25.0517508	Nitric oxide	-	-	-	-
at T = 30.0 °C											
Permeation rate (ng/min)	Molecular weight of NO <sub>2</sub>	K factor	Flow rate (ml/min)	Cinitial (ppm)	Cmin (ppm)	Cmax (ppm)	NO <sub>2</sub>	-	Ceiling limit 1 ppm	-	10102-44-0
1012	46.0055	0.5316756	30.4	17.6991996	0.00131105	1.10619997	Nitrogen dioxide	-	-	-	-
at T = 30.0 °C											
Permeation rate (ng/min)	Molecular weight of NH <sub>3</sub>	K factor	Flow rate (ml/min)	Cinitial (ppm)	Cmin (ppm)	Cmax (ppm)	NH <sub>3</sub>	25 ppm	35 ppm	-	7664-41-7
8542	17.031	1.4362046	30.4	403.554586	0.02989293	25.2221616	Ammonia	-	-	-	-
at T = 30.0 °C											
Permeation rate (ng/min)	Molecular weight of C <sub>6</sub> H <sub>6</sub>	K factor	Flow rate (ml/min)	Cinitial (ppm)	Cmin (ppm)	Cmax (ppm)	C <sub>6</sub> H <sub>6</sub>	0.5 ppm	2.5 ppm	Skin;A1,1	71-43-2
780	78.11	0.3131481	30.4	8.03472161	0.00059516	0.5021701	Benzene	-	-	-	-
at T = 25.0 °C											
Permeation rate (ng/min)	Molecular weight of CO	K factor	Flow rate (ml/min)	Cinitial (ppm)	Cmin (ppm)	Cmax (ppm)	CO	25 ppm	100 ppm	R	630-08-0
13950	28.01	0.8732596	30.4	400.722721	0.02968316	25.0451701	Carbon monoxide	-	-	-	-
at T = 30.0 °C											
Permeation rate (ng/min)	Molecular weight of SO <sub>2</sub>	K factor	Flow rate (ml/min)	Cinitial (ppm)	Cmin (ppm)	Cmax (ppm)	SO <sub>2</sub>	2 ppm	5 ppm	-	7446-09-5
2611	64.066	0.3817938	30.4	32.791564	0.002429	2.04947275	Sulfur dioxide	-	-	-	-

Table 4.1 NIOSH permissible limits for different Volatile Organic Compounds and toxic gases. The provided colors indicate degree for human risk assessment with regard to each and every hazard's toxicity upon certain conditions (high/low risk role categorization: red, yellow, blue) and substance conditions (orange), as reported in [13].

As reported in Figure 4-5, straight detections of C<sub>2</sub>H<sub>6</sub>O were demonstrated during the first trials. Indeed, the capabilities of the Drop-Casted GO coated Love wave sensor examined sensitivities near 112 Hz/ppm during multiple exposures, at a variety of C<sub>2</sub>H<sub>6</sub>O levels. The adsorption-desorption characteristics of the Drop-Casted GO device reported great results according to the NIOSH permissible limits (< 1000 ppm for C<sub>2</sub>H<sub>6</sub>O).

A further comparison of the Drop-Casted GO device showed that the GO sensing material stands decently among alternative sensing materials under similar vapor exposures. As shown in the Figure 4-6, GO exhibits higher sensitivities, even responses with two orders of magnitude superior to TiO<sub>2</sub>, mesoporous SiO<sub>2</sub> or Molecular Imprinted Polymers (MIPs) [14]-[15].

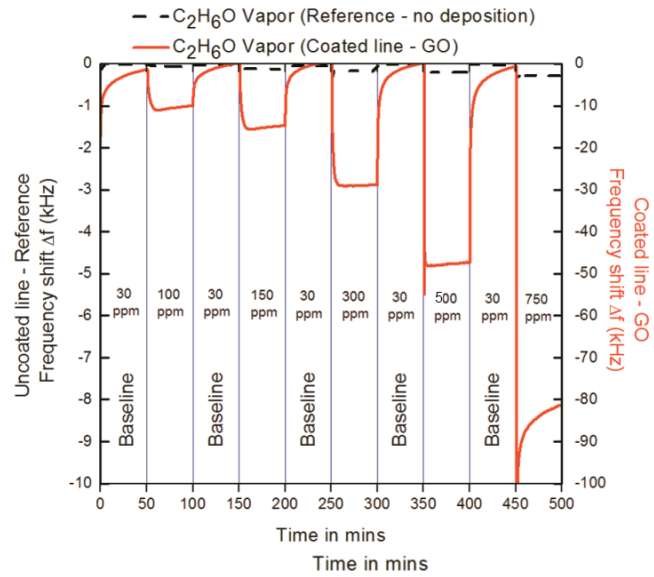


Figure 4-5 Dynamic responses of GO - coated and uncoated delay lines towards  $C_2H_6O$  vapors (adsorption - desorption).

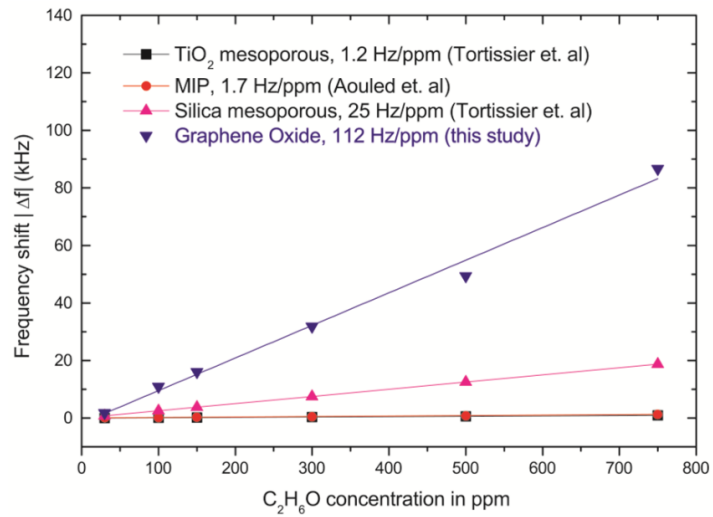


Figure 4-6 Comparison of Ethanol ( $C_2H_6O$ ) responses between different sensitive layers coated on Love wave devices. Silica mesoporous, MIP and  $TiO_2$  are adapted from literature (Ref. [14]-[15]) and GO from this study.

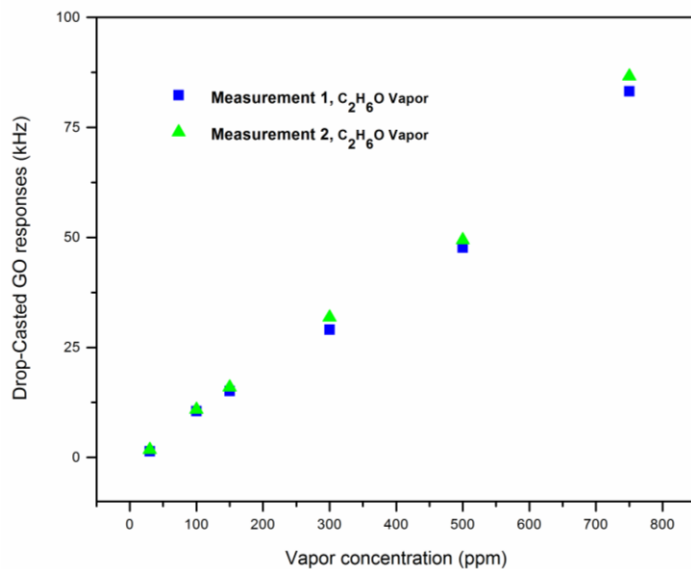


Figure 4-7 Reproducibility of the Drop-Casted GO Love wave device (R37B07) regarding the **ethanol** exposures.

Moreover, the Drop-Casted GO coated Love wave sensor was reported in a reproducible manner regarding the C<sub>2</sub>H<sub>6</sub>O exposures (Figure 4-7), however the Drop-Casted deposition method does not cover the demands of industrialization processability (degradation/fragmentation of the GO sensing material), since the prepared compounds were based on chemical laboratory procedures. Thus, compromising between the cost of the fabrication techniques and the cross-sensitivity levels of an alternative preparation and deposition method, low cost devices can be fabricated by utilizing inkjet-printing GO compounds, which can provide certainly applications in industrial processes and commercialization.

Nonetheless, whereas the aim is to foster the admission of the Inkjet-Printed GO method, mainly due to the necessity of transforming the current scientific research into the industry in a safe, reproducible, low-cost and uncomplicated manner. In addition, it was essential that stable jetting procedures will be established for the sake of functionality and tenability of the sensor devices. As it will be discussed later, the Inkjet-Printed GO devices reported a lower sensitivity than the Drop-Casted (pilot study of Inkjet-Printed GO method) [16], however evidently, later work showed that there is a significant improving on the performance of the industrial ‘friendly’ Inkjet-Printed GO solution, thus leading to higher achievements of cross-sensitivity levels with low-cost fabrication techniques.

## IV.4 Inkjet – Printed GO sensor performances

### IV.4.1 Detection of Ethanol and Toluene Vapors in real time

As mentioned in a previous section (IV.3.2), NIOSH permissible limits for different Volatile Organic Compounds (NIOSH Table 4.1) were introduced into the gas line experimental setup according to permeation of the vapor generators. Similar experimental conditions have been



maintained for the  $C_2H_6O$  and  $C_7H_8$  vapor detections regarding the inkjet-printed GO sensor performances. At this state, acquiring initial results regarding the VOC detections, an additional substance was calibrated on the PUL – 010 vapor generator based on an analogous calibration technique at STP conditions, thus introducing a constant laminar flow rate (30ml/min) of nitrogen with a conventional stepping sequence of  $C_7H_8$  concentrations. The equivalent concentrations were circulated directly on both delay lines of the acoustic path, which were placed in a specific hermetic cell. Accordingly, the cycling process was initiated from 30 ppm of each target analyte, ethanol or toluene, and further used as a base-line for the bare and coated devices, respectively.

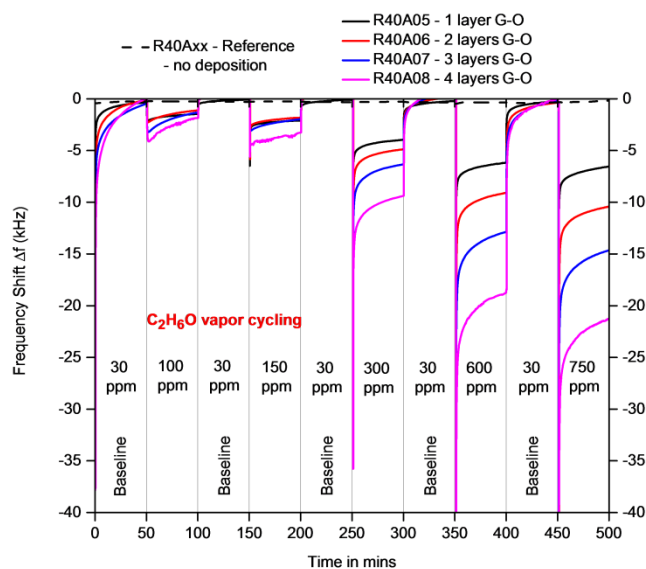


Figure 4-8 Dynamic response of Inkjet – Printed GO based Love wave sensors towards  $C_2H_6O$  (ethanol) vapor.

The maximum of the concentration exposures was selected up to 750 ppm for both substances as shown in the adsorption-desorption responses in Fig. 4-8 and 4-9, respectively. Change in response time was followed by several cycling VOC exposures and the sensor responses showed similar performances in terms of frequency shift ( $\Delta f$ ) in a wide range of  $C_2H_6O$  and  $C_7H_8$  exposures. As illustrated in Fig. 4-10 and 4-11, the steady-state variations of frequency shifts showed a linear evolution ( $R^2_{eth} = 0.996$  for ethanol and  $R^2_{tol} = 0.994$  for toluene) towards vapor exposures, which were inextricably correlated with the number of GO printed passages (1-4).

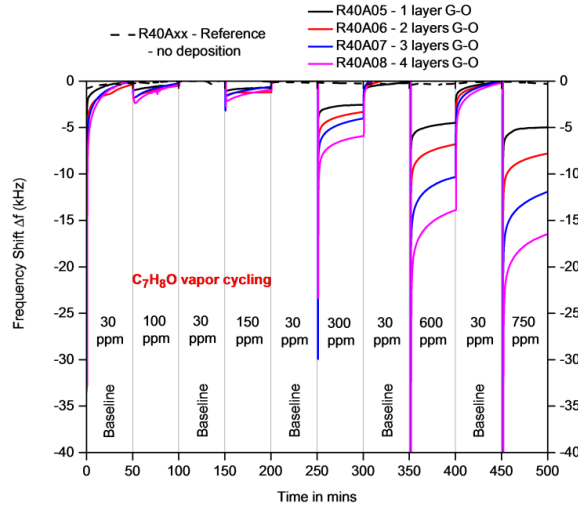


Figure 4-9 Dynamic response of Inkjet – Printed GO based Love wave sensors towards C<sub>7</sub>H<sub>8</sub> (toluene) vapor.

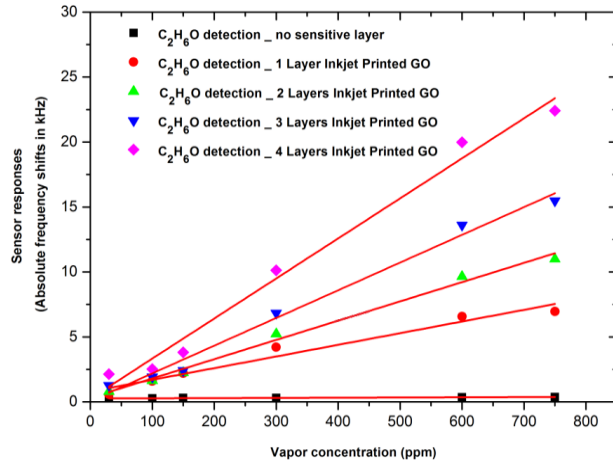


Figure 4-10 Linear responses of GO coated devices under C<sub>2</sub>H<sub>6</sub>O vapors.

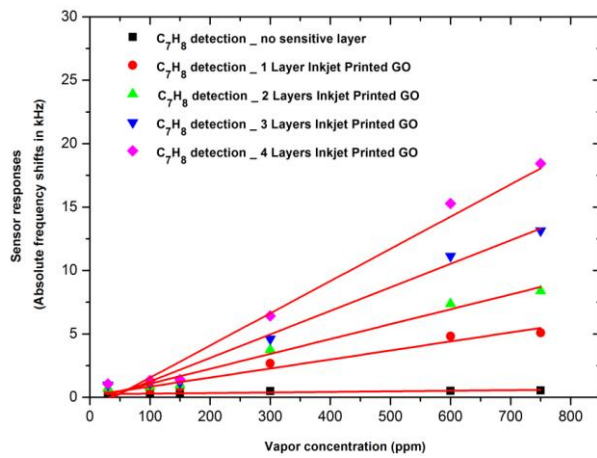


Figure 4-11 Linear responses of GO coated devices under C<sub>7</sub>H<sub>8</sub> vapors.

The highest sensitivities were reported in the device with the four inkjet-printed GO layers, for  $C_2H_6O$  ( $30 \text{ Hz.ppm}^{-1}$ ) and  $C_7H_8$  ( $24 \text{ Hz.ppm}^{-1}$ ) vapors, respectively. Furthermore, by comparing the VOC sensitivities of the Inkjet-Printed GO Love wave devices versus the number of GO passages, it was observed that printed GO sensitive films were slightly more reactive when they exposed to ethanol vapors rather than to toluene, as it is graphically depicted in Figure 4-12.

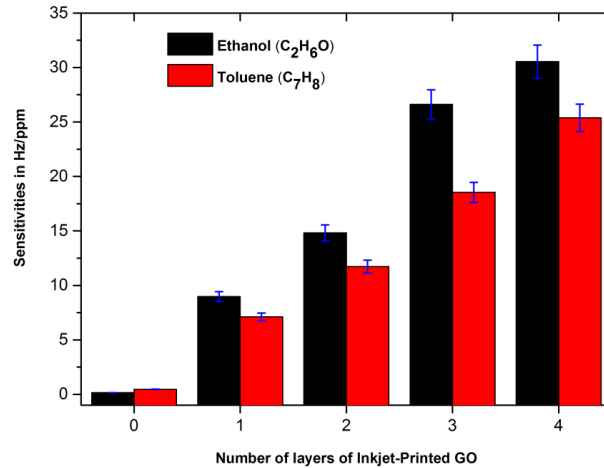


Figure 4-12 Cross-sensitivity responses of bare and coated Inkjet-Printed GO Love wave devices towards ethanol and toluene exposures, respectively; Sensitivity evolution ( $\text{Hz/ppm}$ ) versus the number of GO printed passages.

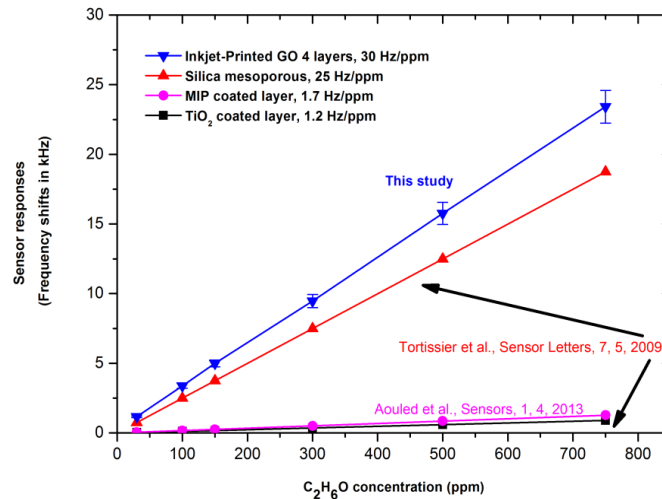


Figure 4-13 Ethanol ( $C_2H_6O$ ) comparison responses of different sensing layers such as GO (this study), Silica mesoporous [17], MIP [18] and  $TiO_2$  [17] coated on Love wave devices.

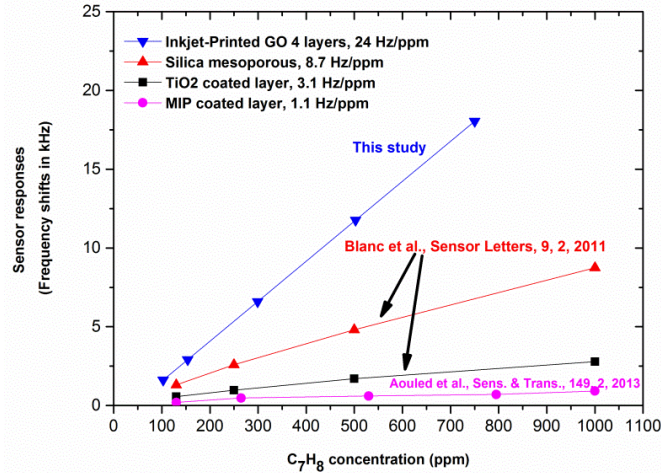


Figure 4-14 Toluene ( $C_7H_8$ ) comparison responses of different sensing layers such as GO (this study), Silica mesostructured [19], MIP [20] and  $TiO_2$  [19] coated on Love wave devices.

The data gathered of this study were based on several inkjet-printed GO depositions and further suggested that the valorization of the inkjet-printed technique was crucial, since the adsorption of vapors on GO sheets provided sensitivities of  $30 \text{ Hz.ppm}^{-1}$ ,  $24 \text{ Hz.ppm}^{-1}$  for  $C_2H_6O$  and  $C_7H_8$  exposures, respectively. Indeed, the experimental results of this work, especially for  $C_2H_6O$  detection responses, were advantageously compared with relative works in the literature (Fig. 4-13), which include different sensitive coatings such as  $TiO_2$  [17], Molecularly Imprinted Polymer (MIP) [18] and Silica mesoporous [17], respectively. Moreover, the inkjet-printed GO sensing layers reported higher sensitivity than Silica mesoporous and rate up to one order of magnitude in terms of sensitivity compared to  $TiO_2$  and MIP. For  $C_7H_8$  comparisons, the very similar sensing layers were selected to compare the sensitivities of the GO sheets. Similarly, in this case, as represented in Fig. 4-14, Inkjet-Printed GO based devices reported higher sensitivity values than Silica mesoporous [19],  $TiO_2$  [20] and MIP [19], respectively.

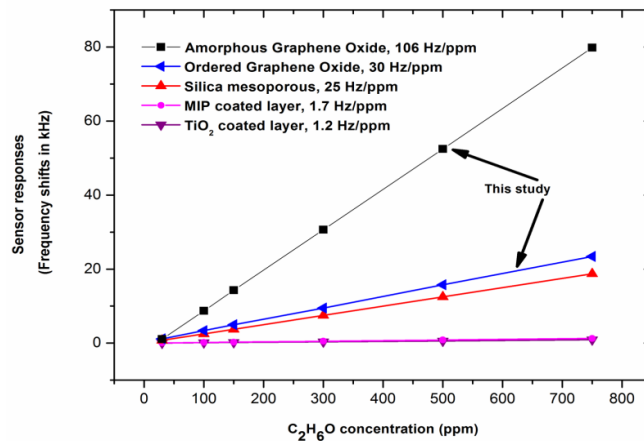


Figure 4-15 Comparison studies of Ethanol ( $C_2H_6O$ ) responses based on different sensing layers such as amorphous (Drop-Casted GO [21]) and ordered GO (Inkjet-Printed GO[16]), Silica mesoporous [17], MIP [18] and  $TiO_2$  [17] coated on Love wave devices.

An analytical comparison has shown that different GO compositions are suitable for multi-gas detection applications. For instance, Drop-Casted GO provides better performances towards ethanol and toluene; however, to provide multidisciplinary studies towards  $\text{NH}_3$  and  $\text{NO}_2$  different geometrical and volumetric types (Inkjet-Printed GO) were fabricated, respectively. As depicted in Figure 4-15, our studies show that the Drop - Casted GO thin film reports three times higher sensitivity than the Inkjet - Printed GO (4 passages) regarding the ethanol vapor detections. However, the Drop – Casted GO sample deteriorated very quickly due to the used deposit method. The printed GO layers are more stable and reproducible and no deterioration was observed. This is due to the additive ink-jet printing technology used which offers an appropriate way for mass productive gas sensors.

#### IV.4.2 Specificity to $\text{NH}_3$ and $\text{NO}_2$ detections

As presented on the context of this thesis, the increased public awareness of unhealthy environment and health risks caused by environmental pollution has provoked a high demand for sensitive and analytical techniques [22]. For example, on an average the Threshold Limit Value (TLV) of ammonia gas is 25 ppm, well below any danger or damage. This work part aims at overcoming the limitations of existing sensors through an integrated electronic acoustic platform based on GO, dedicated to the detection of  $\text{NO}_2$  and  $\text{NH}_3$  gases, which is able to identify and thus prevent critical concentration levels.

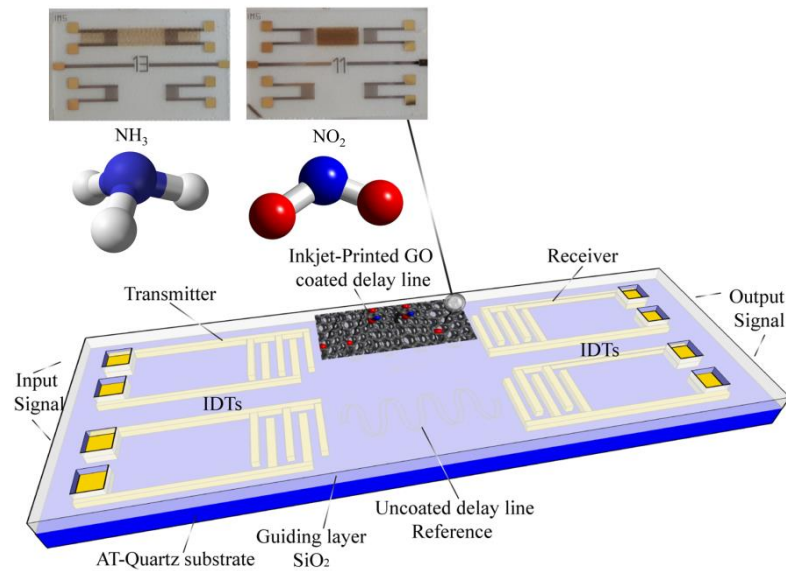


Figure 4-16 Illustration of the GO coatings on LW devices. Different aspect ratio of the GO coatings target alternative gases such as  $\text{NH}_3$  and  $\text{NO}_2$ , respectively.

For the reasons described above, the mechanisms of  $\text{NH}_3$  and  $\text{NO}_2$  detection by GO ink-based devices are investigated by different experimental methodologies adjusted to each analyte. As represented in the Fig. 4-16, while both  $\text{NH}_3$  and  $\text{NO}_2$  can physisorb to graphene, the following work shows that their adsorption only results in particular conditions of the GO inks through the devices. When the GO ink covers the full-length of the sensor device leads to the most sensitive

detection sites of  $\text{NH}_3$ , where the higher amounts of GO passages (between the IDTs) lead to  $\text{NO}_2$  detection mechanism, which chemisorption may occurs. That is due to the fact that effective and reproducible  $\text{NO}_2$  detections occurred, especially in ambient temperature conditions of the resulting sensor. In general, different concentrations of  $\text{NH}_3$  and  $\text{NO}_2$  can also chemisorb at the GO inks thus, the phenomenon which occurs is probably a very peculiar GO sensing mechanism, that of physisorption and chemisorption, respectively. In order to enhance the detection sensitivity, it was thus essential to find the optimum, efficient and reproducible results of the vapor detections, as well as the shape and the thickness of the GO inks, respectively. Thus, different configurations of the Inkjet-Printed GO coatings were established on the commonly used Love wave platform.

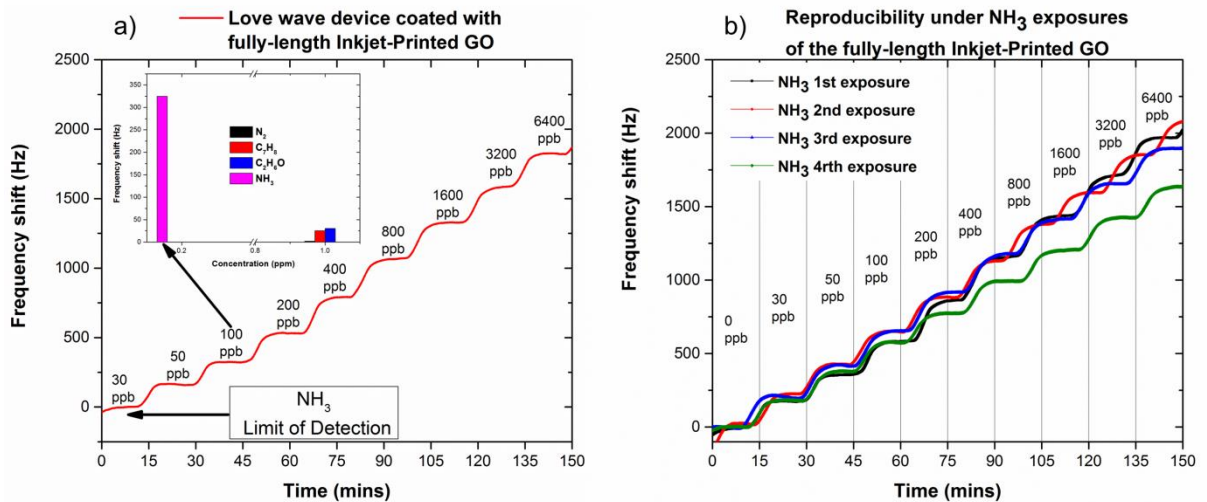


Figure 4-17 (a) Real time ammonia detections and specificity of the fully-length Inkjet-Printed GO coated sensor; insert steady-state frequency shift reported detections towards  $\text{N}_2$  [16],  $\text{C}_7\text{H}_8$  [16] and  $\text{C}_2\text{H}_6\text{O}$  [16] and  $\text{NH}_3$  vapor exposures; (b) Reproducibility under  $\text{NH}_3$  exposures of the fully-length Inkjet-Printed GO sheets.

Fig. 4-17 (a) illustrates the transient responses of the Inkjet-Printed GO device to  $\text{NH}_3$  concentrations in the range from 30 ppb to 6.4 ppm. The experimental detection threshold was found at 30 ppb and the detection of 100 ppb of ammonia gas corresponds to a frequency shift of 332 Hz, then the sensitivity was estimated at 4.7 Hz / ppb. On the insert of the Figure 4-17 (a), the  $\text{NH}_3$  frequency shifts were compared with previous sensitivity detections towards  $\text{N}_2$ ,  $\text{C}_7\text{H}_8$  and  $\text{C}_2\text{H}_6\text{O}$  responses, respectively. As a sign of repeatability, the  $\text{NH}_3$  criteria behavior shared similar detections with reproducible measurements at wide range of concentrations, as illustrated in Figure 4-17 (b); nevertheless, the subsequent 4<sup>th</sup> exposure under  $\text{NH}_3$  vapors showed that the sensor device seems to have entered into a saturation regime. As indicated from the following  $\text{NH}_3$  exposures, the developing sensor drift is slightly detected at the 2<sup>nd</sup> and 3<sup>rd</sup>, however the frequency response drawback is reliably diagnosed at 4<sup>th</sup>.

Furthermore, a similar investigation has been realized on the fully-length coated Love wave sensor (sample no.13) towards  $\text{NO}_2$  concentration levels. In order to reach the LoD towards  $\text{NO}_2$  concentrations, it was necessary to increase the amount of  $\text{NO}_2$  significantly through plenty of

experimental steps. Finally, the detection limit was acquired at the minimum NO<sub>2</sub> concentration level of 17 ppm. Then, a repeatability procedure was established with a time slot of 58 hours experiment, in which has been maintained according to the calibrated NO<sub>2</sub> manufacturer conditions. As depicted in Fig. 4-18 (a), the sensor responses were found to be a little noisy; however, there is certainty regarding the NO<sub>2</sub> detections (102 Hz/ppm), since the device showed great repeatability under a plethora of cycles with similar responses. Gathering all the sensor responses together, whereas each response is represented by the detection of 17 ppm NO<sub>2</sub> exposure (frequency shift), it has been observed that in a long run experiment, the device is expected to reach a saturation limit of NO<sub>2</sub> detections nearby at 800 Hz (Figure 4-18 (b)). Basically, the prediction of the saturation limit has been calculated in the basis of the experimental exponential decay of the sensor responses. Moreover, according to the Figure 4-18 (b), the frequency shifts were fitted on the total time scale of the experiment exposures, thus showing a typical sensor-drift behavior. Ideally, a further adjustment of the saturation limit (drift compensation) may be necessary, since the sensor has been contaminated for a long time, as plenty of commercial NO<sub>2</sub> applications include a specific network of NO<sub>2</sub> sensors to countermeasure similar performances.

Thanks to this study, the responses showed significant results in real time detection with sensitivity of 4.7 Hz/ppb and 102 Hz/ppm at very low concentrations of ammonia (NH<sub>3</sub>) and nitrogen dioxide (NO<sub>2</sub>) gases, respectively. The experimental limit of detection (LoD) was found at 30 ppb for NH<sub>3</sub> gas in ambient conditions and at 25 ppb for the NO<sub>2</sub>, with specificity compared to interfering gases of N<sub>2</sub>, C<sub>7</sub>H<sub>8</sub> and C<sub>2</sub>H<sub>6</sub>O. Since the inkjet-printing method offers low-cost fabrication devices and also an easy way of functionalization by chemically tailoring the properties of GO ink, its customization of different aspect ratio of the sensing material was able to target alternative gases such as NH<sub>3</sub> and NO<sub>2</sub> conveniently, thus leading to a generic multi-sensor device for specificity purposes. Furthermore, the length of the GO ink segment does consequently affect the relative sensitivity of one analyte but does not affect the sensitivity of the other one. These results suggest that there is not a cross-linking between the sensitivities of the device and thus each tuning could be further used to recognize different specificities of the target analytes.

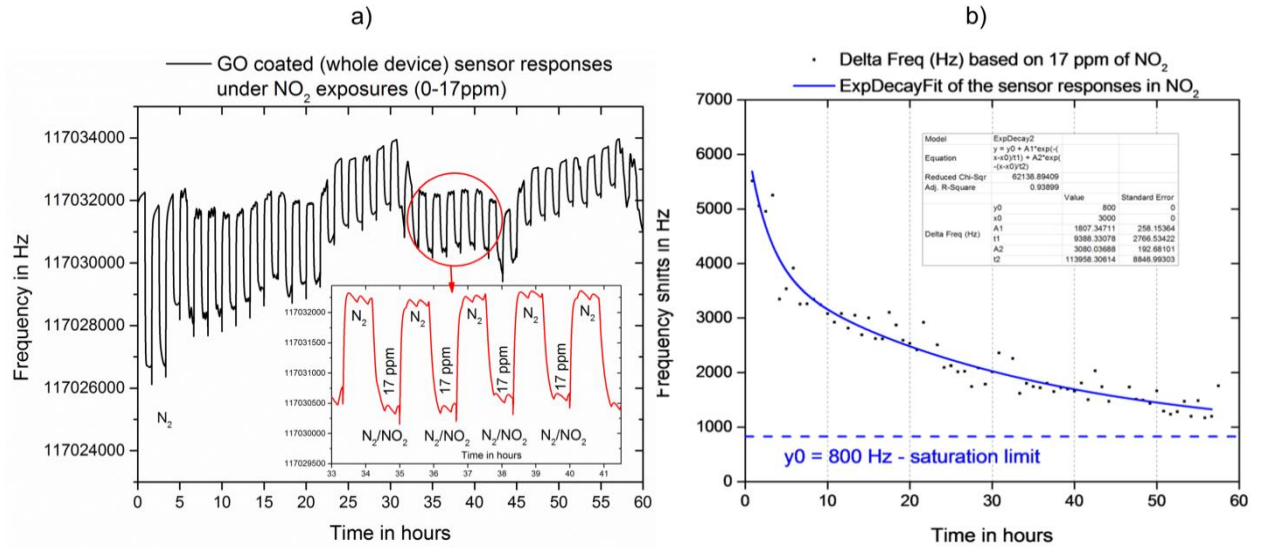


Figure 4-18 (a) NO<sub>2</sub> detections based on high concentrations at room temperature sample no.13 (full length – 4 GO passages). (b) Frequency shifts in a long run exposure of NO<sub>2</sub>. Each point corresponds to a frequency shift of 17ppm - NO<sub>2</sub> exposure under a 58 hours experiment.

#### IV.4.3 Detection of humidity

For the real-time RH detections, a wide range of concentrations was introduced on the highest performance sensor device (4 GO printed passages – sensitivity of  $2.4 \text{ kHz} \cdot 1\%^{-1}$ ), based on a particular cycling step sequence of 30 minutes (Figure 4-19). During these measurements, the RH was increased in the chamber from 10% to the target concentration, up to 76 %, and then returned back to 10 %. As represented in Figure 4-20, a measurement of the steady-state frequency shift showed that the RH hysteresis of the sensor device was nearly 5% based on the adsorption–desorption cycling characteristics. As illustrated in Figure 4-21, a further experimental investigation of the RH adsorption – desorption cycling process showed that the GO coated Love wave sensor demonstrates good responding characteristics when the relative humidity is changed between nitrogen and 10 % RH. In this work, particular analyses of the RH phenomena are provided, especially on how GO printed.



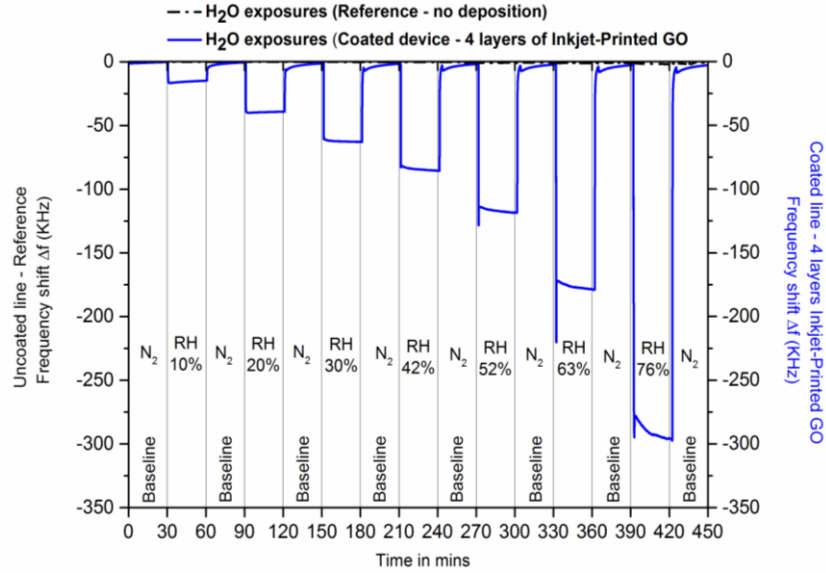


Figure 4-19 Dynamic response of the 4 layers Inkjet – Printed GO based Love wave sensor towards H<sub>2</sub>O vapor.

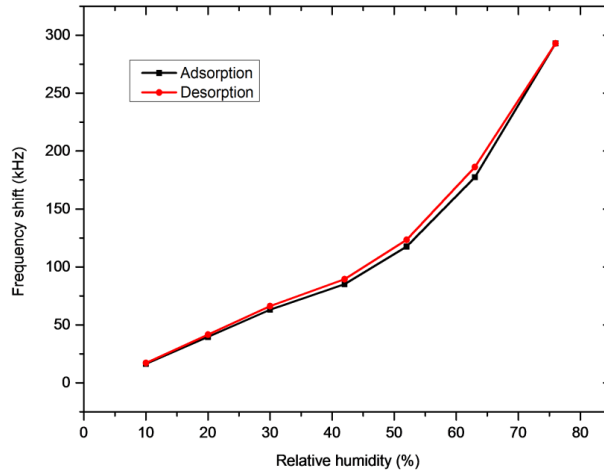


Figure 4-20 Hysteresis of the 4 layers Inkjet – Printed GO humidity sensor. The frequency shift was measured during the adsorption – desorption characteristics towards H<sub>2</sub>O vapor.

layers facilitate water adsorption and desorption in a surface level. A well-known model [23] was selected and fitted with our experimental moisture responses. The steady-state frequency shifts versus the RH were analyzed (Figure 4-22) based on the modified Anderson’s and Brunauer’s equation [23], [24]:

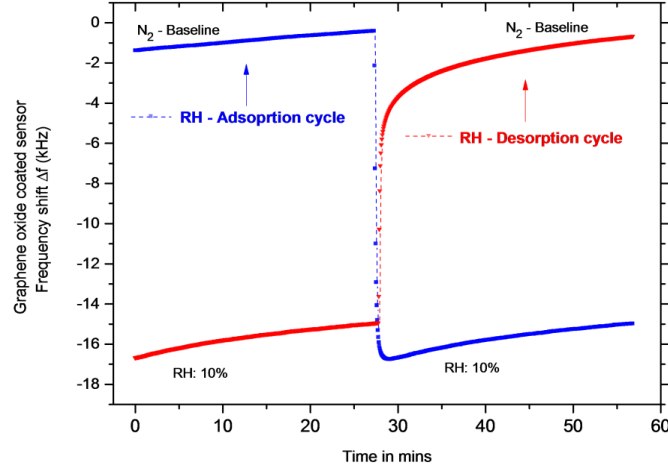


Figure 4-21 Adsorption-desorption cycles of the GO coated sensor under humid (10%) and nitrogen conditions, respectively.

$$\frac{V}{V_m} = \frac{ck'(P/P_0)}{[1 - k'(P/P_0)][1 + (c-1)k'(P/P_0)]} \quad (4.3)$$

where  $V$  is the volume occupied by the adsorbed vapor molecules,  $V_m$  is the volume occupied by the gas molecules corresponding to a saturated monomolecular layer adsorption,  $P$  is the gas pressure,  $P_0$  is the saturated vapor pressure at the adsorption temperature,  $c$  is a parameter related to adsorption characteristics and  $k'$  is a coefficient, which represents the excess of the heat of liquefaction that the second and subsequent layers release and it is mainly related on the adsorption system mechanism of the GO printed layers. The frequency shifts of the GO coated Love wave device represent the output of the sensor, which is equal to the amount of the adsorbed vapor, since it occurs that  $V/V_m = \Delta f / \Delta f_{monolayer}$ , where,  $\Delta f$  represents the frequency shift of the adsorbed vapor concentrations and  $\Delta f_{monolayer}$  is corresponding to the frequency shift of one monolayer of RH. Further, the real-time detection responses of the four layers GO based Love wave device can be related with the BET adsorption characteristics of the RH, especially at a surface level approximation, by substituting the modified BET parameters described above in the equation (4.4):

$$\frac{\Delta f}{\Delta f_{monolayer}} = \frac{ck'x}{(1 - k'x)[1 + (c-1)k'x]} \quad (4.4)$$

where  $x$  represents the relative pressure  $P/P_0$ . Since the equation (4.4) is in a good agreement with the experimental results, as represented in Fig. 4-22, the monolayer of RH induces a variation of 173.168 kHz ( $\Delta f_{monolayer}$ ) to the resonance frequency of the GO coated Love wave device. Furthermore, this work provides a brief observation of the recent literature on SAW devices associated with RH responses, followed by an analysis and estimation of the moisture detections [25], [26]. Fig. 4-23 illustrates relatively high performance responses of the Inkjet-Printed GO under different exposures of RH compared to alternative sensing materials such as, Polyvinylpyrrolidone (PVP) [25] and a mixture of ZnO (film) with ZnO nanorods [26].

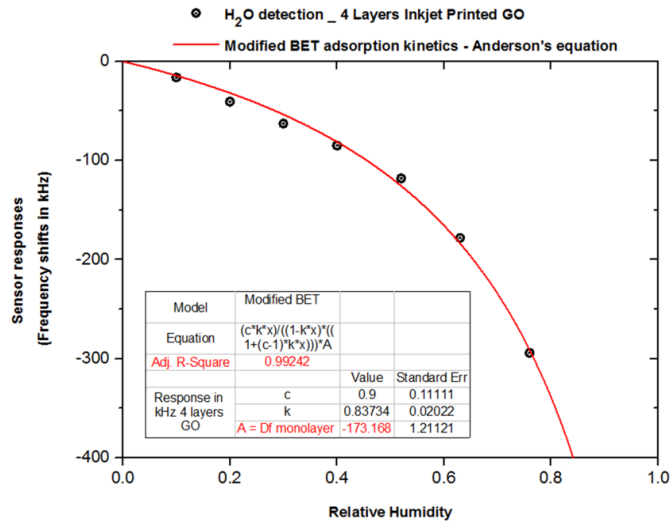


Figure 4-22 Measured (circles) and calculated (solid line) frequency shifts vs RH for the GO - coated Love wave device.

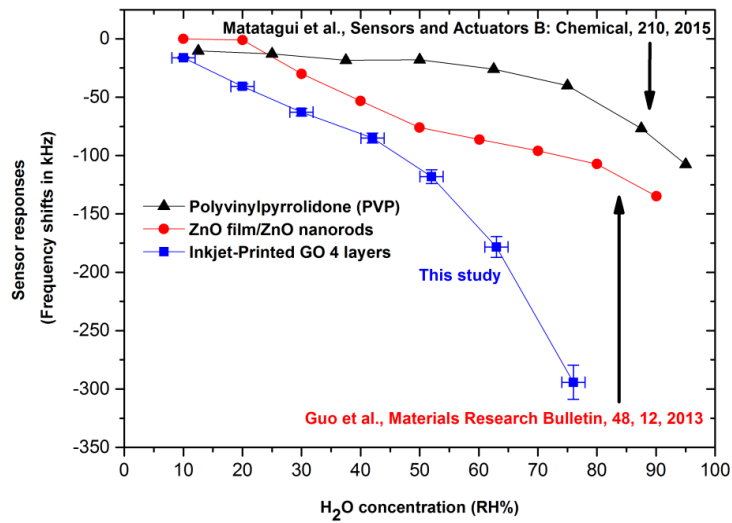


Figure 4-23 Comparison of H<sub>2</sub>O responses of different sensing layers, such as GO (this study), ZnO film/ZnO nanorods [25] and PVP [26].

However, it could also be inferred that the comparison responses showed in Figure 4-23 are based on the efficiency of the optimum coated sensor devices, that is, a Love wave platform with four GO-ink passages. It is worth noting that further data analyses provided useful information regarding the reproducibility of the detection responses based on humid concentrations. As illustrated in the comparison Figure 4-23, the layer-by-layer GO coated Love wave devices were exposed several times on particular cycling vapor conditions, and a relative standard deviation of 5% was observed, especially at higher concentration levels.

## References or Bibliography (if any)

- [1] A. Z. Sadek, W. Wlodarski, K. Shin, R. B. Kaner, and K. Kalantar-zadeh, "A layered surface acoustic wave gas sensor based on a polyaniline/In<sub>2</sub>O<sub>3</sub> nanofibre composite," *Nanotechnology*, vol. 17, no. 17, p. 4488, 2006.
- [2] H. Xu, D. Ju, W. Li, H. Gong, J. Zhang, J. Wang, and B. Cao, "Low-working-temperature, fast-response-speed NO<sub>2</sub> sensor with nanoporous-SnO<sub>2</sub>/polyaniline double-layered film," *Sens. Actuators B Chem.*, vol. 224, pp. 654–660, Mar. 2016.
- [3] Q. Chang, K. Zhao, X. Chen, M. Li, and J. Liu, "Preparation of gold/polyaniline/multiwall carbon nanotube nanocomposites and application in ammonia gas detection," *J. Mater. Sci.*, vol. 43, no. 17, pp. 5861–5866, Sep. 2008.
- [4] N. G. Deshpande, Y. G. Gudage, R. Sharma, J. C. Vyas, J. B. Kim, and Y. P. Lee, "Studies on tin oxide-intercalated polyaniline nanocomposite for ammonia gas sensing applications," *Sens. Actuators B Chem.*, vol. 138, no. 1, pp. 76–84, Apr. 2009.
- [5] T. Zhang, S. Mubeen, B. Yoo, N. V. Myung, and M. A. Deshusses, "A gas nanosensor unaffected by humidity," *Nanotechnology*, vol. 20, no. 25, p. 255501, 2009.
- [6] Z. Wu, X. Chen, S. Zhu, Z. Zhou, Y. Yao, W. Quan, and B. Liu, "Enhanced sensitivity of ammonia sensor using graphene/polyaniline nanocomposite," *Sens. Actuators B Chem.*, vol. 178, pp. 485–493, Mar. 2013.
- [7] F.-W. Zeng, X.-X. Liu, D. Diamond, and K. T. Lau, "Humidity sensors based on polyaniline nanofibres," *Sens. Actuators B Chem.*, vol. 143, no. 2, pp. 530–534, Jan. 2010.
- [8] A. K. Geim and K. S. Novoselov, "The rise of graphene," *Nat. Mater.*, vol. 6, no. 3, pp. 183–191, Mar. 2007.
- [9] C. Zimmermann, D. Rebière, C. Déjous, J. Pistré, E. Chastaing, and R. Planade, "A love-wave gas sensor coated with functionalized polysiloxane for sensing organophosphorus compounds," *Sens. Actuators B Chem.*, vol. 76, no. 1, pp. 86–94, Jun. 2001.
- [10] W. Xuan, M. He, N. Meng, X. He, W. Wang, J. Chen, T. Shi, *et al.*, "Fast Response and High Sensitivity ZnO/glass Surface Acoustic Wave Humidity Sensors Using Graphene Oxide Sensing Layer," *Sci. Rep.*, vol. 4, p. 7206, Nov. 2014.
- [11] H. Bi, K. Yin, X. Xie, J. Ji, S. Wan, L. Sun, M. Terrones, *et al.*, "Ultrahigh humidity sensitivity of graphene oxide," *Sci. Rep.*, vol. 3, p. 2714, Sep. 2013.
- [12] S. Borini, R. White, D. Wei, M. Astley, S. Haque, E. Spigone, N. Harris, *et al.*, "Ultrafast Graphene Oxide Humidity Sensors," 12-Nov-2013. [Online]. Available: <http://pubs.acs.org/doi/abs/10.1021/nn404889b>. [Accessed: 14-Feb-2018].
- [13] "CDC - NIOSH Publications and Products - NIOSH Manual of Analytical Methods (2003-154) - CAS List All." [Online]. Available: <https://www.cdc.gov/niosh/docs/2003-154/method-casall.html>.
- [14] C. Dejous, H. Hallil, V. Raimbault, J.-L. Lachaud, B. Plano, R. Delépée, P. Favetta, *et al.*, "Love Acoustic Wave-Based Devices and Molecularly-Imprinted Polymers as Versatile Sensors for Electronic Nose or Tongue for Cancer Monitoring," *Sensors*, vol. 16, no. 6, p. 915, Jun. 2016.
- [15] G. Tortissier, L. Blanc, A. Tetelin, C. Zimmermann, J.-L. Lachaud, C. Boissière, C. Sanchez, *et al.*, "Mesoporous Coated Films on Love Wave Acoustic Devices for Gas Detection," *Sens. Lett.*, vol. 7, no. 5, pp. 984–988, Oct. 2009.
- [16] I. Nikolaou, H. Hallil, V. Conédéra, G. Deligeorgis, C. Dejous, and D. Rebière, "Inkjet-Printed Graphene Oxide Thin Layers on Love Wave Devices for Humidity and Vapor Detection," *IEEE Sens. J.*, vol. 16, no. 21, pp. 7620–7627, Nov. 2016.

- [17] G. Tortissier, L. Blanc, A. Tetelin, C. Zimmermann, J.-L. Lachaud, C. Boissière, C. Sanchez, *et al.*, “Mesoporous Coated Films on Love Wave Acoustic Devices for Gas Detection,” *Sens. Lett.*, vol. 7, no. 5, pp. 984–988, Oct. 2009.
- [18] H. Hallil, N. Omar-Aouled, B. Plano, R. Delépée, L. A. Agrofoglio, C. Dejous, and D. Rebière, “Love Wave Sensor Based on Thin Film Molecularly Imprinted Polymer: Study of VOCs Adsorption,” *J. Integr. Circuits Syst.*, vol. 9, no. 2, pp. 118–122, Jan. 2014.
- [19] L. Blanc, A. Tetelin, C. Boissière, G. Tortissier, J.-L. Lachaud, C. Déjous, and D. Rebière, “Mesostuctured TiO<sub>2</sub> and SiO<sub>2</sub> as high specific surface area coatings for vapour Love wave sensors,” *Sens. Lett.*, vol. 9, pp. 1–4, 2011.
- [20] N. Omar-Aouled, N. Lebal, H. Hallil, R. Delepee, L. A. Agrofoglio, D. Rebière, and C. Dejous, “Study of gaseous compounds adsorption with a Love wave sensor based on molecularly imprinted polymer thin film,” *Sens. Transducers J.*, vol. 149, no. 2, pp. 37–42, Feb. 2013.
- [21] I. Nikolaou, H. Hallil, G. Deligeorgis, V. Conédéra, H. Garcia, C. Dejous, and D. Rebière, “Drop-casted Graphene Oxide Love Wave sensor for detection of humidity and VOCs,” *J. Integr. Circuits Syst.*, vol. 11, no. 1, pp. 49–56, Apr. 2016.
- [22] X. Morelli, C. Rieux, J. Cyrus, B. Forsberg, and R. Slama, “Air pollution, health and social deprivation: A fine-scale risk assessment,” *Environ. Res.*, vol. 147, pp. 59–70, May 2016.
- [23] R. B. Anderson and W. K. Hall, “Modifications of the Brunauer, Emmett and Teller equation,” *J. Am. Chem. Soc.*, vol. 70, no. 5, pp. 1727–1734, May 1948.
- [24] L. Wang, J. Liu, and S. He, “The Development of Love Wave-Based Humidity Sensors Incorporating Multiple Layers,” *Sensors*, vol. 15, no. 4, pp. 8615–8623, Apr. 2015.
- [25] D. Matatagui, O. V. Kolokoltsev, N. Qureshi, E. V. Mejía-Uriarte, and J. M. Saniger, “A novel ultra-high frequency humidity sensor based on a magnetostatic spin wave oscillator,” *Sens. Actuators B Chem.*, vol. 210, pp. 297–301, Apr. 2015.
- [26] Y. J. Guo, J. Zhang, C. Zhao, J. Y. Ma, H. F. Pang, P. A. Hu, F. Placido, *et al.*, “Characterization and humidity sensing of ZnO/42° YX LiTaO<sub>3</sub> Love wave devices with ZnO nanorods,” *Mater. Res. Bull.*, vol. 48, no. 12, pp. 5058–5063, Dec. 2013.



## Chapter 5

### Conclusions and Prospects

## V. The Good, the Bad and the Missing

### V.1 Introduction

The conclusion of this research thesis reaffirms plenty of the thesis statements, discusses the issues, and opens new horizons without providing a judgmental summary; it is a belief based on the author's reasoning and on the evidences that have been previously accumulated. The following chapter represents a place to share with readers the conclusions and prospects that have reached towards innovation in material planning, and an ongoing research process in micro-sensors research.

In summary, the outcome of the following Ph.D. studies presents the usefulness of GO as a sensitive layer in the acoustic wave devices and highlights the broad range of applications based on the amalgamation of GO and Love wave devices. An analytical comparison has shown that the Drop-Casted GO coatings were able to provide higher performances than the Inkjet-Printed GO Love wave devices towards selected compounds, however to provide Inkjet-Printed GO devices offered great advantages at a wide range of chemical detections.

To date, multidisciplinary studies towards  $\text{NH}_3$  and  $\text{NO}_2$  led to different geometrical and volumetric GO types and showed that the Drop - Casted GO thin films could be easily replaced by novel fabrication techniques, such as Inkjet-Printing GO due to its diversity to detect several high-risk targeted analytes and its extremely low detection limit potential. Moreover, the printed GO layers provided more stable, reversible and reproducible guidelines, thus being diversified with current industrial demands, especially due to their facile deposition method and the solution-based ways for mass productive gas sensor applications.

In an unprejudiced manner, both deposition techniques were offered a great amount of scientific research, since carbon-based materials, such as graphene, are still remaining a hot topic in the scientific literature and community, who create innovation fronts', especially when it comes to group together great majority of the scientific, research and development sectors. On a similar manner, graphene-based materials offer plenty of interests and often generate questions due to their complexity and industrial demands. For these reasons, carbon derivatives are always remaining under the 'eye' of scientific research because to overcome scientific challenges of this nature, necessitates constant success and innovation in major technological steps. Working with promising materials, that of graphene, there are no sidelined research topics, thus production of scientific research outcomes can only participate as an importer where material innovation is diffused.

### V.2 The Good

Regarding the performance of the Drop-Casted GO devices, GO based acoustic wave sensor provided high sensitivity, especially in guide lined NIOSH concentrations. The real time



detections of the GO coated sensor provided promising results and opened the horizon to further investigate more complex GO coatings, since it has reported sensitivities of 32 kHz/5% and 112 Hz/ppm, for RH and ethanol, respectively. Moreover, at this state, it was highlighted that future work must focus on realizing graphene based acoustic wave devices in a more reproducible and facile manner, but in the same time facing challenges that of enhancing performance of sensitivity and selectivity to a specific target gas, thus paving the way towards hypersensitive and selective gas - moisture applications.

On the other hand, focusing on Inkjet-Printed GO technique, the reported GO coated Love wave devices were shown great potential in terms of performance. Similarly, by using simple methods, electrical, gaseous and moisture characterization results showed that this method of GO processability offers low insertion loss and high sensing abilities to the resulting devices, at different geometrical features of GO (higher thickness levels / fully length coated devices). Moreover, the adsorption of vapors on GO sheets provided sensitivities of 30 Hz.ppm<sup>-1</sup>, 24 Hz.ppm<sup>-1</sup> and 2.4 kHz.1%<sup>-1</sup> for C<sub>2</sub>H<sub>6</sub>O, C<sub>7</sub>H<sub>8</sub> and RH, respectively. These results provided confirmatory evidences that GO facilitates water adsorption in a surface level, which is based on a plethora of hydrophilic functional groups of GO material, and further to its large surface to volume ratio. At this state, future guidelines add the necessities to further understand the fabricated GO structures theoretically, thus realizing even more efficient GO coated Love wave devices with detections based only on a moderate specificity for pulmonary toxic substances. Furthermore, the appearance of the Inkjet-Printed method in depth as perceived by efficient initial trial results showed that this study was crucial to further investigate plenty of potential applications related with GO films.

From a materials point of view, it was essential to study the mechanical properties of GO composites regarding the Inkjet-Printed deposition method towards future functionalization aspects. Theoretical and experimental results were in agreement and mainly based on the analytical modeling and the fitted electrical characterization results of the GO Love wave devices. FEM analysis showed useful information in order to explain the physical mechanical properties of the GO sheets deposited on fused silica (SiO<sub>2</sub>). Young's modulus, Shear modulus and Poisson's ratio of the devices were found near 470 GPa, 196 GPa and 0.197, respectively, and subsequently, were validated through their good agreement between the theoretical and experimental results. Furthermore, the analytical investigation approach showed that the unique viscoelastic properties of the GO composites are inextricably linked with the GO thickness and a biphasic behavior was observed. Moreover, this uniform GO deposition method might be applied as an appealing technique to unambiguously discern between different GO viscosities of high-tunable multi-functional inks. Finally, colocalized AFM/Raman measurements allowed the significant roughness of GO films, as well as its good chemical homogeneity to be determined.

After further understanding of the current Inkjet-Printed GO nature, it was essential to test these devices under a wide range of vapors to fabricate and to date challenges based on a multi-sensory device. Confirmatory results put the evidence of specificity towards NH<sub>3</sub> or NO<sub>2</sub>, and it has been shown that the fully-length modified GO allowed customization and specificity towards

NH<sub>3</sub> and the multi-coated GO passages (between the IDTs) towards NO<sub>2</sub> analytes, thus providing a bright future of optimized multi-sensor arrays devices for environmental application purposes.

Perspectives and challenges of this work have been placed under the microscope multiple times during journal reviews, conference communications or plenty of discussion group meetings. Thus, it essential for one more time, to take a distance and evaluate the objectives of this work according to the literature perspectives in order to observe the stand-point of this research conduct.

Today, the exclusive structures and properties of recent carbon-based nanomaterials, namely called CNTs, graphenes and graphene oxides, are threatening the dominance of alternative well-established nanomaterials such as TiO<sub>2</sub>, PVP, ZnO nanorods in potential gas or humid sensing applications. However, the commercial production of carbon-based sensors is still some way off, and there are still great challenges that require our attention. Fabrication process is still remaining one of the main challenges and research breakthroughs are needed to find cost-effective, scalable production methods that retain the essential properties of such materials. If the use of high-purity graphenes as gas-sensitive materials isn't narrowed down, then alternative methods as Inkjet-Printed technique seems the growth method of choice.

### V.3 The Bad and the Missing

While some of our results have shown the possibility of growing and transferring ultrapure, suspended graphene oxides (Drop-Casted laboratory suspensions), thus suppressing unwanted hysteresis caused by humidity interactions in Inkjet-Printed GO devices, a higher needed breakthrough would be the growth of graphene oxides with predictable adsorption/desorption properties. This would avoid using the costly and, most of the times not scalable methods, used nowadays to fabricate devices with optimal sensitivity performances.

Since research and innovation offer solutions to overcome these kinds of challenges, nevertheless, if alternative lower quality carbon nanomaterials such as reduced graphene oxides continue to build on its promise for gas and humid sensing environments, then chemical exfoliation of graphite followed by Drop-Casting would be scaled-up. With the current research efforts of this Ph.D. thesis, directed to solve these issues, it seems that reaching large-scale fabrication was just a matter of time. Although it has been shown that a single-layer adsorption/desorption of gas or humid compounds are detectable when using our graphene oxide devices, so far, the electrical device detections of gas or humid adsorption on CNTs and graphenes have similarly reported detection limits at ppb levels successfully, in laboratory conditions.

Thus, functionalization of the carbon-based nanomaterials could be realized by renovating selected surface areas with metal or metal oxide nanoparticles or by grafting functional groups. Functionalization is needed more than ever, since it provides a practical way to increase sensitivity, minimize unwanted effects (cross-sensitivities) and enhance selectivity. Selectivity still remains a great challenge as many studies show the difficulty of making carbon

nanomaterials absolutely selective to a particular substance. A standard typical solution is mainly based on using multi-sensor arrays with partially overlapping sensitivities and seems to remain the optimum choice in the current literature. In order to effectively impact on research conduct, a long-term comprehensive approach has to be developed that consists of the specific functionalization components. By translating the current research results to the industrial demands, this long-term approach has to be diversified with recent industrial practices of multi-sensor arrays, since they represent the most efficient way to take advantage of the cross-sensitivity responses towards different target analytes. However, research perspectives like the aforementioned one, highlights a common drawback among the gas trace sensing applications.

For example, traces of different gases may commonly interference with each other and also lead to problems, as even superior analytical methods are not free of cross-sensitivity, therefore, are not selective enough.

An important challenge, closely related to the previously mentioned ones, is avoiding the presence of unwanted contaminants at the sensor surface. These contaminants may result high adsorption phenomena during the normal function of the sensor detections because they produce typical drift behaviors of the sensor devices (drift-compensation). Moreover, counterintuitive methods can be applied such as periodical temperature cycling processes, since they proved to be useful to regenerate the sensor performances (NO<sub>2</sub> detections). Possibly the best approach would be to implement an appropriate functionalized surface, therefore, the tailored and over-layer functionalized GO could be used to protect the device's high surface to volume ratio and the detection area from the excess liquefaction that the second and subsequent adsorbed layers release. Well-designed functionalization should be targeted at balancing the strength of adsorption of analytes (needed for high sensitivity) against the reversibility of the detection processes, which is a fundamental necessity for gas or humid detection sensors during long-term vapor measurements.

## V.4 Finally...

The current work of studies has provided an insight into the nature of the scientific challenges that some were overcome and others still remain under ongoing investigations; however, there is confidence that this approach will help and guide future perspectives and actions in a more advanced manner.

## VI. Appendices (if any)

### VI.1 Author's contributions

The Ph.D. thesis contributions diversified towards the completion of an accurate and stable monitoring detection system of the target analyte under consideration and, therefore providing evidence tailored to health policy-makers (WHO) and industrialization techniques (high-yield fabrication), as well as highlighting the specificity awareness of graphene-based acoustic wave devices.

Thus, the following papers have been published in refereed journals as well as international conference proceedings by the MDA group; therefore are link to the work undertaken by several studies of graphene-based acoustic wave devices. Most of the material presented in these papers has been incorporated into this Ph.D. thesis.

Full publication list at (Citations: 42, h-index: 3):

<https://scholar.google.fr/citations?user=UrVoLDMAAAAJ&hl=en>

[https://www.researchgate.net/profile/Ioannis\\_Nikolaou6](https://www.researchgate.net/profile/Ioannis_Nikolaou6)

#### **Journals:**

I Nikolaou, H Hallil, V Conédéra, B Plano, O Tamarin, JL Lachaud, D Talaga, S Bonhommeau, C Dejous, D Rebière “Electro-Mechanical properties of Inkjet-Printed graphene oxide nanosheets”, *Physica status solidi A: Applications and Materials Science*, 2017 214 (3), 1600492.

I Nikolaou, H Hallil, V Conédéra, G Deligeorgis, C Dejous, D Rebiere “Inkjet-printed graphene oxide thin layers on love wave devices for humidity and vapor detection”, *IEEE Sensors Journal* 2016 (21), 7620-7627.

I Nikolaou, H Hallil, B Plano, G Deligeorgis, V Conedera, H Garcia, C Dejous, D Rebière “Drop-casted Graphene Oxide Love wave sensor for detection of humidity and VOCs”, *Journal of Integrated Circuits and Systems*, 2016 (11), 49-56.

#### **International Conferences and proceedings:**

C Dejous, L Bechou, H Hallil, S Hemour, S Joly, JL Lachaud, L Oyhenart, V Raimbault, D Rebière, O Tamarin, P Bahoumina, M Diez, F Meziane, I Nikolaou, “Resonant wave-based microsensors for environmental and health related applications”, 8ème Franco-Spanish Workshop IBERNAM-CMC2, 2016.

I Nikolaou, H Hallil, O Tamarin, C Dejous, D Rebière “A three dimensional model for a graphene guided SH-SAW sensor using Finite Element Method”, IEEE 31st Symposium on Microelectronics Technology and Devices (SBMicro), 2016, 1-4.

I Nikolaou, H Hallil, V Conédéra, JL Lachaud, C Dejous, D Rebière, “Properties of Love wave sensors based on graphene oxides”, 16th International Meeting on Chemical Sensors (IMCS 2016).

I Nikolaou, H Hallil, V Conédéra, JL Lachaud, C Dejous, D Rebière, “Enhanced properties of Love wave microsensors with Inkjet-Printed graphene oxide layers”, E-MRS (2016) Spring Symposium Y, 1.

I Nikolaou, H Hallil, C Dejous, D Rebière, G Deligeorgis, V Conedera, “Inkjet – Printed graphene layer by layer on SAW devices for gas detection applications”, Sensors (2015), 1305, 1-4.

I Nikolaou, H Hallil, G Deligeorgis, V Conedera, H Garcia, C Dejous, D Rebière, “Novel SAW gas sensor based on Graphene”, IEEE 30th Symposium on Microelectronics Technology and Devices (SBMicro), 2015, 1-4.

I Nikolaou, H Hallil, G Deligeorgis, V Conedera, H Garcia, C Dejous, D Rebière, “Gas sensor platform based on Graphene”, 18èmes Journées Nationales du Réseau Doctoral en Micro-nanoélectronique JNRDM (2015), 5-9.

I Nikolaou, H Hallil, G Deligeorgis, V Conédéra, H Garcia, C Dejous, D Rebière, “Real time VOCs and humidity monitoring based on ultrasensitive Graphene-SAW devices”, Journée CMC2 «Intégration du Matériau au Système de détection chimique résonant» (2015).

I Nikolaou, H Hallil, G Deligeorgis, V Conedera, H Garcia, C Dejous, D Rebière, “Novel SH-SAW gas sensor based on Graphene”, SPIE Microtechnologies, 2015, (9517), 1-7.

## VI.2 Appendix A - Chapter I: Classification of acoustic wave devices and gas sensing mechanisms

### VI.2.1 A.1 – Classification of acoustic wave devices

During the last decades, the acoustic wave devices have been widely investigated in piezoelectric resonators for Radio-Frequency (RF) telecommunication applications, in radars, cellular phones and plenty of technological advances, targeting and thereby leading to significant multi-variational sensor activities [1]. Regarding the polarization of the acoustic waves, three types can be distinguished such as longitudinal, transverse vertical and transverse horizontal. The

particle direction of the longitudinal waves or compressional waves should be regarded as parallel to wave propagation direction, whilst the particle displacement of the transverse waves or shear waves is perpendicular to the propagation direction. Furthermore, the acoustic wave devices can be separated into three different categories, such as Bulk Acoustic Wave (BAW), Surface Acoustic Wave (SAW) and Acoustic Plate Mode (APM) devices [1]. This classification can be divided into various sub-categories that already exist in the literature, depending on the generation of the acoustic waves and their propagation mode. In particular, the BAW devices are divided in Quartz Crystal Microbalance (QCM) [2] and Film Bulk Acoustic Resonators (FBARs) [3], the SAW family is represented by Rayleigh, Shear-Horizontal Surface Acoustic Wave (SH-SAW) [4], Surface Transverse Wave (STW) [5] and Love wave devices [6], while the APM family includes the Shear-Horizontal Acoustic Plate Mode (SH-APM) [7] and the Flexural Plate Wave (FPW) [8] devices. Precisely, in the first group (BAW devices), the polarization can be longitudinal or transverse, thus it is the volume of the material (substrate) that deforms, allowing the acoustic wave to propagate unguided. The SAW devices can be represented by a Rayleigh wave [9] (longitudinal and transverse), or by the waveform of Bleustein-Gulyaev [10], which is polarized in the transverse horizontal plane. Generally, in SAW devices, the acoustic wave propagates guided or unguided, along the surface of the substrate. When the SAW is unguided and shear polarized, the generated acoustic waves can be represented by the SH-SAW device, whilst the guided and shear polarized acoustic waves correspond to the guided SH-SAW or Love wave mode devices. In the third group (APM devices), the wave propagates in the volume of the substrate material, either in the form of two Rayleigh waves (one per side), such as a Lamb wave or in the form of a transverse horizontal wave undergoing reflections at the surface of the material (SH-APM). The scope of this work is focused on the finite element analysis of the guided SH-SAW sensors. The main theoretical premise behind the Love wave devices is that by using a piezoelectric substrate and an over-layer with a lower shear wave velocity, a Love wave can be generated [11]. The advantage of this mode is that it operates a thin trapping layer to guide the propagating wave to the surface of the substrate instead of alternative invasive detection methods.

In order to provide a clear perspective of the gas sensing principles, sensing technologies are classified into two groups [12] a) based on electrical variation and material aspects and b) based on different kind of variation properties, as shown in Figure A-1.

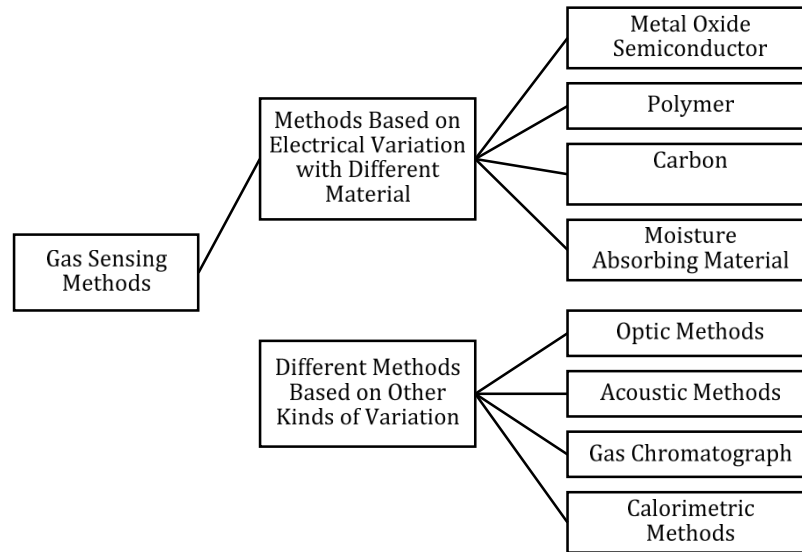


Figure A-1 Classification of gas sensing method technologies [12].

In general, a gas sensor is a device incorporating a gas sensitive element (i.e.: thin film) either intimately connected to or integrated within a transducer. The usual aim is to produce an electronic output signal which is proportional to the gas concentration. In recent years, the development of gas sensors has become increasingly important [12]. Sensors are used in applications ranging from medical diagnostic and health care, defense and security, automotive and industrial manufacturing, as well as environmental monitoring [13]. Regardless of the associated applications, all sensors have the same objectives which are to provide stable and accurate monitoring of the target gas [13].

## VI.3 Appendix B - Chapter II:

### VI.3.1 B.1 Post-fabrication procedures

Following fabrication procedures of the Love wave devices, it was essential to minimize the defects during the transportation (from LAAS-CNRS to IMS laboratories), thus the devices were coated on the top surface with a common photolithographic resist material and filed according to their fabrication and identification RUN numbers, respectively. When the acoustic wave devices received at IMS laboratories, a general cleaning protocol has been followed to prepare the sensors towards electrical & gas sensing performances. Thus, resist stripping involves removal of all the photoresist applied on the wafer tape-out. To realize this, a standard cleaning process was adapted to meet the electrical characterization challenges ahead, as illustrated in the Table B.1.


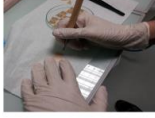

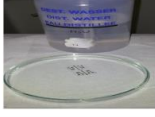
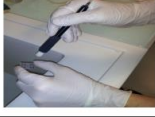

Steps	Procedure name	Description	Images
1	Dispatch of the acoustic wave devices	Remove the sensors from the blue protective film (after etching process).	
2	Identifier	Engrave the serial number on each sensor (Diamond Pen – Back side of the sensor).	
3	Photoresist stripping	Immerse the sensor in acetone for 1 minute (very thin photoresist layer).	
4	Rinse	Immerse the sensor in distilled water for 1 minute.	
5	Dry and verification	Nitrogen and dry air mixture until complete drying. Observe the sensor for a complete cleanliness.	
6	Sort and listing of the devices	Placing the acoustic wave devices on the plastic covers. Measure and record the device performances in the IMS database for the current wafer RUN.	

Table B-1 Standard Cleaning steps of the acoustic wave devices, as received from CNRS-LAAS to IMS laboratories, including all stripping and cleaning procedures.

Then, the devices were validated according to the electrical performances and characterized by a Vector Network Analyzer (VNA).

### VI.3.2 B.2 – Electrical measurement procedures & Calculations

**Electrical characterization (S - parameters) and the acoustic wave platform:** to understand the responses of a Surface Acoustic Wave device to an external perturbation for chemical sensing, it is necessary to obtain the device frequency response in advance. Measurement of the frequency responses are also important, if the most stable and accurate measurement system is to be designed for a particular device. The acoustic devices have been characterized electrically by using the Anritsu-MS2026B Vector Network Analyzer (VNA).

Plenty of useful information can be monitored during the electrical characterization measurements, such as the acoustic wave velocity and attenuation, respectively. Since the acoustic wave sensor technologies rely on the measurement of velocity perturbations [14], this approach is adequate, if it is known in advance that all perturbations will affect wave velocity, perturbations that include mass loading effects and changes in the viscoelastic properties.

Analytically, at RF and microwave frequencies, electrical measurements of voltage and current become complex and a VNA is commonly used to measure incident and reflected waves. In many



ways, the VNA marries the principles of the basic impedance measurement with hardware appropriate for microwave frequencies. These parameters are usually named scattering parameters and they normally used to characterize high frequency networks, where simple models valid at lower frequencies cannot be applied.

The complete characterization of an acoustic wave device is always obtained from a complete frequency response spectrum including all the scattering parameters. Scattering parameters (S-parameters) are describing the scattering and reflection of the propagating waves when a network is inserted into a transmission line, as illustrated in Figure B-1 below:

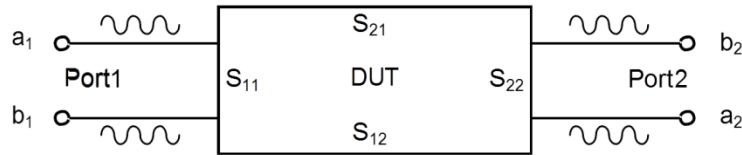


Figure B-1 Two-port S-parameter Model

It is important to realize from the equations B.1 and B.2, that a wave leaving the Device under Test (DUT)  $b_1$  or  $b_2$  is a linear combination of the waves entering the DUT ( $a_1$  or  $a_2$ ).

$$b_1 = S_{11}a_1 + S_{12}a_2 \quad (\text{B.1}) \quad b_2 = S_{21}a_1 + S_{22}a_2 \quad (\text{B.2})$$

As a result, terminating the DUT in the characteristic impedance ( $Z_0$ ) allows the extraction of the individual S-parameters. S-parameters can be considered as the gain of the network, and the subscripts denote the port numbers. For each port, the incident (applied) and reflected wave properties are measured. When the incident wave propagates through the network, its value is multiplied (i.e. its gain and phase are changed) by scattering, thus giving the resulting output value. The ratio of the output of port 2 to the incident wave on port 1 is designated  $S_{21}$ . Likewise, for reflected waves, the signal comes in and out of the same port, hence the scattering parameters for the input reflection are designated  $S_{11}$ . For a two-port network, (assuming the use of matched loads and characteristic impedance at 50ohms),  $S_{11}$  is the reflection coefficient of the input,  $S_{22}$  is the reflection coefficient of the output,  $S_{21}$  is the forward transmission gain, and  $S_{12}$  is the reverse transmission gain, as represented below:

$$S_{11} = \frac{\text{Reflected signal port 1}}{\text{Incident signal port 1}} = \frac{b_1}{a_1} \Big|_{a_2=0}, \quad S_{11}: \text{Input complex reflection coefficient} \quad (\text{B.3})$$

$$S_{21} = \frac{\text{Transmitted signal port 2}}{\text{Incident signal port 1}} = \frac{b_2}{a_1} \Big|_{a_2=0}, \quad S_{21}: \text{Forward complex transmission coefficient} \quad (\text{B.4})$$

$$S_{22} = \frac{\text{Reflected signal port 2}}{\text{Incident signal port 2}} = \frac{b_2}{a_2} \Big|_{a_1 = 0}, \quad S_{22}: \text{Output complex reflection coefficient} \quad (\text{B.5})$$

$$S_{12} = \frac{\text{Transmitted signal port 1}}{\text{Incident signal port 2}} = \frac{b_1}{a_2} \Big|_{a_1 = 0}, \quad S_{12}: \text{Reverse complex transmission coefficient} \quad (\text{B.6})$$

For example, when the characteristic impedance ( $Z_0$ ) is equal to 50 Ohms, and if a 50 Ohm termination is present at port 2,  $a_2$  is reduced to zero, resulting in equations for  $S_{11}$  and  $S_{21}$ . This principle can be applied in the reverse direction as well, by setting  $a_1$  to zero, the equations for  $S_{22}$  and  $S_{12}$  can be obtained, respectively. To determine the scattering parameters of any two-port network, the measurement technique must be capable of measuring incident, reflected and transmitted waves in amplitude and phase and establishing the relative values.

As it has been analyzed above, from the output to input perspective, the S-parameters are used to characterize a DUT within the network. They have a specific importance for high frequency applications, and in their practical usage, S-parameters are expressed in dB. The S-parameters are expressed in complex values, with magnitude and phase, respectively, and they cannot be measured by simply using an oscilloscope or signal analyzer (otherwise only the amplitude information can be extracted). Analytically, due to the VNA capabilities, the magnitude and the phase of a signal can be measured, simultaneously.

One of the key characteristics of a directional device (multi-directional regarding the current fabricated Love wave devices) is the insertion loss (coupling factor, isolation, and directivity will be discussed later). Insertion loss is a metric of the loss of signal power when it is traveling through the directional device (through path). A high-quality directional coupler can present insertion loss as low as 1 dB up to microwave frequencies. The calculation of the insertion loss can be realized by using the equations below:

$$\text{Insertion loss (dB)} = -10 \log_{10} \frac{(\text{output power})}{(\text{input power})} \quad (\text{B.7})$$

$$\text{Insertion loss (dB)} = -10 \log_{10} \left( \frac{P_{out}}{P_{in}} \right) \quad (\text{B.8})$$

$$\text{Insertion loss (dB)} = -20 \log_{10} \left( \frac{V_{out}}{V_{in}} \right) \quad (\text{B.9})$$

By convention, insertion loss is defined as the ratio of input signal to the output signal, and is given in decibels (dB). When the attenuation of a signal is represented by its output magnitude, which is less than input magnitude, the negative values represent attenuation, and positive values gain.

Such facilities are provided on the network analyzer which allows signals to be routed to the input or output ports which are typically coaxial type. These ports are used as the reference planes for the device under test (which may require mounting in standard or specially designed test fixture to provide the interfacing to the measurement ports). System accuracy is enhanced by the use of error correction techniques to remove systematic errors such as source and load mismatches, directivity, coupling variations with frequency etc. The error terms are derived by utilizing known standards such as fixed open and short circuits, fixed loads, sliding loads and through calibration. To determine the S-parameters of the device mounted in the test fixture, the measurement reference planes must be referred through the test fixture to the device reference terminals. The most popular coaxial calibration method and probably the first manual calibration performed by a new VNA user is referred to as either SOLT (Short-Open-Load-Through) or TOSM (Through-Open-Short-Match). This calibration method involves the process of connecting well-known calibration standards to each port. Next, both ports are physically connected to each other. In a simple case, when preparing to measure an insertable coaxial device, which has mating connectors, both calibration ports can be directly connected to each other resulting in a zero-length through or flush through.

In this work, a particular high precision VNA (ANRITSU-MS2026B) was used, as illustrated in Figure B-2:



Figure B-2 Vector Network Analyzer ANRITSU-MS2026B and the calibration-verification kit.

For the calibration of the ANRITSU-MS2026B a calibration-verification kit was inserted to verify the accuracy of the calibration process, but also to verify that the VNA is still operating within its specifications. A calibration kit typically contains precision air lines, mismatched air lines, and precision fixed attenuators. These elements are measured after carefully performing a calibration and compared to their known characteristic to determine if the VNA is still within specification.

Since the acoustic wave devices are sensitive to any environmental changes and several parameters such as temperature, pressure, stress, viscoelastic parameters and electrical conductivity, a particular test cell was used in order to characterize the Love wave devices. In general, all the possible responses were recorded and analyzed systematically, to ensure that any undesirable effects were not included. Hence, it was essential to provide a particular environment for the sensor measurements. As mentioned below, the test characterization cell of the acoustic wave devices encapsulates three different parts for the electrical characterization:

Test cell parts:

- The top part: Cover contains the test medium with a custom rubber square ring.
- Intermediate part: Contains the electrical contacts.
- Lower part: Contains the base support for the acoustic wave devices.

Radio-frequency network analyzer test performances were realized by selecting a wide high-accuracy spectrum to determine the insertion loss of the bared and coated acoustic wave devices. But firstly, the attenuation difference between the insertion of the device and no device setup had to be studied. Since myriad problems can arise during high frequency measurements to degrade

the accuracy, tracking a parameter whose general properties are known a priori is a valuable aid when measurement precision is critical.

The loss factor is classified into three types: constant loss, minimal insertion loss, and maximal insertion loss. Constant loss is the value of insertion loss at the nominal frequency, and minimal and maximal insertion losses are the minimal and maximal values of the insertion loss band. Loss factor calculations using measured S-parameters are simple to perform, and provide useful insight into data quality for passive, reciprocal components, such as acoustic wave devices. As depicted in the Figure B-5, the loss factor is further analyzed by the port-matched transmission and reflection coefficients together, and it is usually symmetric for a physically symmetric component. The forward and reverse loss factors are calculated from passive component S-parameters as:

$$\text{Forward Loss Factor (FLF)} = 1 - |S_{11}|^2 - |S_{21}|^2 \quad (\text{B.10})$$

$$\text{Reverse Loss Factor (RLF)} = 1 - |S_{22}|^2 - |S_{12}|^2 \quad (\text{B.11})$$

By the definition of equations B.10 and B.11, the loss factors are seen to equal the difference between a normalized input power and the power that is reflected and transmitted to the input and output ports, respectively. For reciprocal acoustic wave devices  $S_{21} = S_{12}$ , the differences between the forward and reverse loss factor occur due to differences in  $|S_{11}|$  and  $|S_{22}|$ . For ideal lossless acoustic wave components, the magnitudes of  $S_{11}$  and  $S_{22}$  are equal, but they can deviate from one another whenever loss is present.

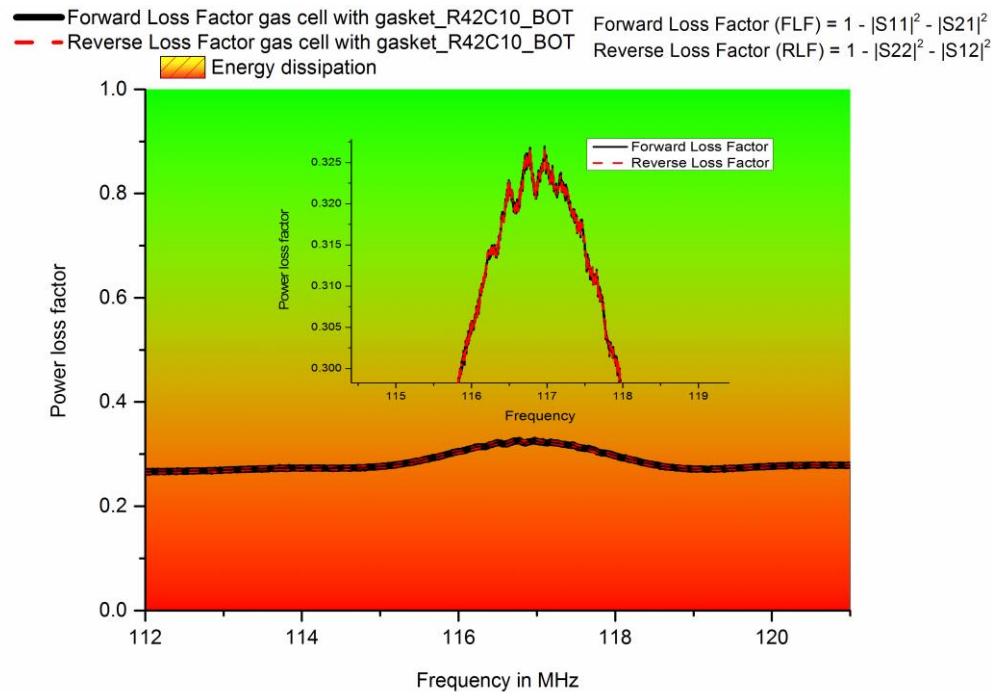


Figure B-3 The Forward and Reverse Loss Factors (FLF and RLF) of a bared acoustic wave device and its energy dissipation.

## VI.4 Appendix C - Chapter III:

### VI.4.1 C.1 Maple analytical equations & calculations:

$$eqdisp \succ k \cdot ki_h \cdot h - \arctan\left(\frac{c_{44} \cdot ki_s}{\mu_{hs} ki_h}\right) + \arctan\left(\frac{G_b \cdot ki_b \cdot \tan(k \cdot ki_b \cdot b)}{\mu_{hs} ki_h}\right) = 0; \quad (C.1)$$

$$f \succ k \cdot ki_h \cdot h - \arctan\left(\frac{c_{44} \cdot ki_s}{\mu_{hs} ki_h}\right) + \arctan\left(\frac{G_b \cdot ki_b \cdot \tan(k \cdot ki_b \cdot b)}{\mu_{hs} ki_h}\right); \quad (C.1)$$

By applying the following substitutions:

$$ki_s := C_a \sqrt{1 - \frac{V_c^2}{V_s^2}}; ki_{hs} := \sqrt{\frac{V_c^2}{V_{hs}^2} - 1}; ki_b := \sqrt{\frac{V_c^2}{V_b^2} - 1};$$

$$C_a := \sqrt{\frac{C_{66}}{C_{44}} - \frac{C_{46}^2}{C_{44}^2}}; V_c := \frac{w}{k}; V_{hs} := \sqrt{\frac{\mu_{hs}}{\rho_{hs}}}; V_b := \sqrt{\frac{G_b}{\rho_b}}; V_s := C_a \sqrt{\frac{C_{44}}{\rho_s}}$$

### Notations explained as:

**Eqdisp:** Represents the dispersion relation as noted in the equation 3.11 in the 3<sup>rd</sup> Chapter.  
**Function F** is the associated equation 3.12 (3<sup>rd</sup> Chapter) - left side of the relation 3.11.  
**EqdispV** is the dispersion relation according to the real part of relation 3.13 which provides the velocity V.

$$eqdispV := subs(G_b = \mu_b, subs(k = k0, f)) = 0; \quad (C.5)$$

$$eqdispV := k0 ki_h h - \arctan\left(\frac{c_{44} C_a \sqrt{1 - \frac{w^2 \rho_s}{k0^2 C_a^2 C_{44}}}}{\mu_{hs} ki_h}\right) + \arctan\left(\frac{\mu_b \sqrt{\frac{w^2 \rho_b}{k0^2 \mu_b} - 1} \tan\left(k0 \sqrt{\frac{w^2 \rho_b}{k0^2 \mu_b} - 1} b\right)}{\mu_{hs} ki_h}\right) = 0$$

**f1** is the derivative of function **f** according to **k**.  
**f2** is the derivative of function **f** according to **G<sup>\*</sup><sub>b</sub>**  
**AlphaC** is the attenuation coefficient **alpha** in equation 3.15.

$$f1 := \text{diff}(f, k); \quad (\text{C.2})$$

$$f1 := ki_h h - \frac{c_{44} w^2 \rho_s}{C_a \sqrt{1 - \frac{w^2 \rho_s}{k^2 C_a^2 C_{44}}} \mu_{hs} ki_h k^3 C_{44} \left( \frac{c_{44}^2 C_a^2 \left( 1 - \frac{w^2 \rho_s}{k^2 C_a^2 C_{44}} \right)}{\mu_{hs}^2 ki_h^2} + 1 \right)}$$

$$+ \frac{1}{G_b^2 \left( \frac{w^2 \rho_b}{k^2 G_b} - 1 \right) \tan \left( k \sqrt{\frac{w^2 \rho_b}{k^2 G_b} - 1} b \right)^2 + 1} \left( \frac{\tan \left( k \sqrt{\frac{w^2 \rho_b}{k^2 G_b} - 1} b \right) w^2 \rho_b}{\sqrt{\frac{w^2 \rho_b}{k^2 G_b} - 1} \mu_{hs} ki_h k^3} \right.$$

$$+ \frac{1}{\mu_{hs} ki_h} \left( G_b \sqrt{\frac{w^2 \rho_b}{k^2 G_b} - 1} \left( \sqrt{\frac{w^2 \rho_b}{k^2 G_b} - 1} b - \frac{b w^2 \rho_b}{k^2 \sqrt{\frac{w^2 \rho_b}{k^2 G_b} - 1} G_b} \right) \left( 1 + \tan \left( k \sqrt{\frac{w^2 \rho_b}{k^2 G_b} - 1} b \right) \right)^2 \right) \right)$$

$$f2 := \text{diff}(f, G_b); \quad (\text{C.3})$$

$$f2 := \frac{1}{G_b^2 \left( \frac{w^2 \rho_b}{k^2 G_b} - 1 \right) \tan \left( k \sqrt{\frac{w^2 \rho_b}{k^2 G_b} - 1} b \right)^2 + 1} \left( \frac{\sqrt{\frac{w^2 \rho_b}{k^2 G_b} - 1} \tan \left( k \sqrt{\frac{w^2 \rho_b}{k^2 G_b} - 1} b \right)}{\mu_{hs} ki_h} \right.$$

$$\left. - \frac{1}{2} \frac{\tan \left( k \sqrt{\frac{w^2 \rho_b}{k^2 G_b} - 1} b \right) w^2 \rho_b}{G_b \sqrt{\frac{w^2 \rho_b}{k^2 G_b} - 1} \mu_{hs} ki_h k^2} - \frac{1}{2} \frac{b w^2 \rho_b \left( 1 + \tan \left( k \sqrt{\frac{w^2 \rho_b}{k^2 G_b} - 1} b \right) \right)^2}{G_b \mu_{hs} ki_h k} \right)$$

$$\begin{aligned}
\text{alphac} &:= \text{subs}\left(G_b = \mu_b, \text{subs}\left(k = k0, -\frac{w \cdot \text{eta} \cdot f2}{fl}\right)\right); \\
\text{alphac} &:= - \left( w \eta \left( \frac{\sqrt{\frac{w^2 \rho_b}{k0^2 \mu_b} - 1} \tan\left(k0 \sqrt{\frac{w^2 \rho_b}{k0^2 \mu_b} - 1} b\right)}{\mu_{hs} k_{ih}} - \frac{1}{2} \frac{\tan\left(k0 \sqrt{\frac{w^2 \rho_b}{k0^2 \mu_b} - 1} b\right) w^2 \rho_b}{\mu_b \sqrt{\frac{w^2 \rho_b}{k0^2 \mu_b} - 1} \mu_{hs} k_{ih} k0^2} \right. \right. \\
&\quad \left. \left. - \frac{1}{2} \frac{b w^2 \rho_b \left(1 + \tan\left(k0 \sqrt{\frac{w^2 \rho_b}{k0^2 \mu_b} - 1} b\right)\right)^2}{\mu_b \mu_{hs} k_{ih} k0} \right) \right) \\
&\quad \left( \frac{\mu_b^2 \left(\frac{w^2 \rho_b}{k0^2 \mu_b} - 1\right) \tan\left(k0 \sqrt{\frac{w^2 \rho_b}{k0^2 \mu_b} - 1} b\right)}{\mu_{hs}^2 k_{ih}^2} \right)^2 \\
&+ 1 \left( k_{ih} h - \frac{c_{44} w^2 \rho_s}{C_a \sqrt{1 - \frac{w^2 \rho_s}{k0^2 C_a^2 C_{44}}} \mu_{hs} k_{ih} k0^3 C_{44} \left( \frac{c_{44}^2 C_a^2 \left(1 - \frac{w^2 \rho_s}{k0^2 C_a^2 C_{44}}\right)}{\mu_{hs}^2 k_{ih}^2} + 1 \right)} \right) \\
&+ \frac{1}{\mu_b^2 \left(\frac{w^2 \rho_b}{k0^2 \mu_b} - 1\right) \tan\left(k0 \sqrt{\frac{w^2 \rho_b}{k0^2 \mu_b} - 1} b\right)^2 + 1} \left( \frac{\tan\left(k0 \sqrt{\frac{w^2 \rho_b}{k0^2 \mu_b} - 1} b\right) w^2 \rho_b}{\sqrt{\frac{w^2 \rho_b}{k0^2 \mu_b} - 1} \mu_{hs} k_{ih} k0^3} \right) \\
&+ \frac{\mu_b \sqrt{\frac{w^2 \rho_b}{k0^2 \mu_b} - 1} \left( \sqrt{\frac{w^2 \rho_b}{k0^2 \mu_b} - 1} b - \frac{b w^2 \rho_b}{k0^2 \sqrt{\frac{w^2 \rho_b}{k0^2 \mu_b} - 1} \mu_b} \right) \left(1 + \tan\left(k0 \sqrt{\frac{w^2 \rho_b}{k0^2 \mu_b} - 1} b\right)\right)^2}{\mu_{hs} k_{ih}} \right)
\end{aligned} \tag{C.7}$$



## VI.4.2 C.2 Numerical calculations – Comsol formulas:

The GO stress relaxation,  $\sigma_{GO}$ , defines the time-dependent deviation as a function of the applied gravimetric loadings (equation C.8). In general:

$$\sigma = \int_0^t C(t-t'_n) \cdot \frac{d\varepsilon(t'_n)}{d(t'_n)} \cdot d(t'_n) \quad (C.8)$$

where  $\sigma$  is the stress,  $C$  represents the compliance function, and  $\varepsilon$  is the strain. Since the condition states that GO structure is loaded, the addition of an extra load will provide the same additional creep as the first applied load to the unloaded GO structure. Then the shear stress is considered by the governing equation (C.9) [15]:

$$\sigma_{ij}(t) = \int_0^t 2 \cdot \Gamma(t-t'_n) \cdot \frac{d\varepsilon_{ij}(t'_n)}{d(t'_n)} \cdot d(t'_n) \quad (C.9)$$

where  $\Gamma(t)$  represents the relaxation shear modulus function, which is often approximated in a Prony series [16]:

$$\Gamma(t) = G + \sum_{m=1}^N G_m \cdot \exp(-t_0 / \tau_m) \quad (12) \quad (C.10)$$

where  $\tau_m$  are the relaxation time constants of the spring-dashpot pairs in the same branch, and  $G_m$  represents the stiffness of the spring in branch  $m$ . Physical interpretation of this approach, which is often called the generalized Maxwell model [15], is shown in Figure C-1 below:

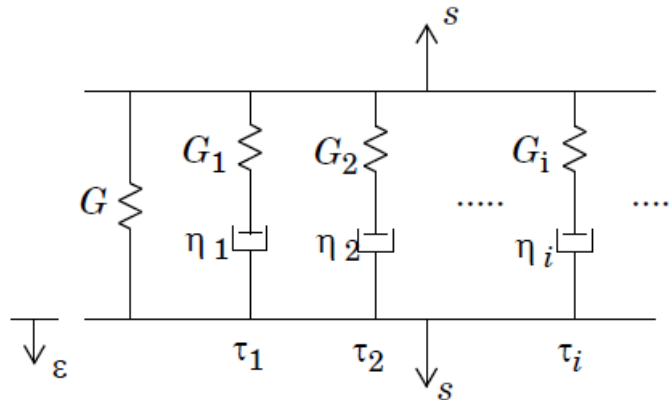


Figure C-1 Relaxation shear modulus approach, namely called generalized Maxwell model [15].

## VI.5 Appendix D - Chapter IV: Gas line experimental conditions and further investigation of the graphene based sensitive material

### VI.5.1 D.1 Vaporizer PUL110 (ppm) and PUL010 (ppb) conditions

The assembly is controlled by a Programmable Logic Controller (PLC), which allows different concentration levels to be translated on certain sequences by programming a user interface control panel (OP3 Operator Panel - Siemens [17]). The desired concentration values are extracted from the Equation (D.1) below:

$$C = \frac{P(T)}{F} \quad (\text{D.1})$$

where C is the initial concentration ( $\text{mg}/\text{Nm}^3$ ) with N from table  $\Delta.1$ , P(T) is the permeation rate of the desired substance ( $\text{ng} \times \text{min}^{-1}$ ), that is known at the critical temperature and F is the dilution flow rate of nitrogen ( $\text{ml} \times \text{min}^{-1}$ ). Generally, certain abbreviations have been used, as is shown:

Abbreviations	Conditions
N: Normal conditions	Temperature of 0 °C and Pressure of 1.013 bar
STP: Standard Temperature and Pressure conditions	Temperature of 20 °C and Pressure of 1.013 bar
Calibration conditions	Critical Temperature of the substance and Pressure of 1.013 bar

Table  $\Delta.1$  Provided definitions upon certain conditions.

To convert the concentration from  $\text{mg}/\text{Nm}^3$  (N corresponds to the Normal conditions; Table  $\Delta.1$ ) in PPM/V, the initial concentration is multiplied by the following factor K:

$$K = \frac{V}{M_w} = \frac{V_0 T}{273.15 M_w} \quad (\text{D.2})$$

where V is the molar volume at a certain Temperature in °K,  $M_w$  is the molecular weight of the substance and  $V_0$  is the volume of one mole of an ideal gas at STP conditions, which occupies 22.41 liters. That means:

$$C(\text{ppm}) = \frac{KP(T)}{F} \xrightarrow{(2)} C(\text{ppm}) = \frac{24.45P(T)}{M_w F} \quad (\text{D.3})$$

where C is the initial concentration (ppm), P(T) is the permeation rate ( $\text{ng} \times \text{min}^{-1}$ ) of the desired substance (RH or VOCs), that is known at the critical temperature (calibration conditions) and F is the diluted flow rate of nitrogen ( $\text{ml} \times \text{min}^{-1}$ ).

To provide any of useful information regarding the RH experiments, that is to describe the related process flow. The main aspects of converting the vapor concentrations to RH% were analyzed by calibrating (Tables Δ.2 and Δ.3) and measuring the quantities through a standard process at fixed flow rates. The RH values were recorded during these calibration procedures, by importing a very limited concentration at each of the mass flow controllers, separately. Then, the RH was measured near 10%, 20%, 30%, 40%, 50%, 60%, 70%, 80%, 90%, 100% desired values. It's worth noting that all the initial values of RH concentrations were validated for both vapor generators PUL110 and PUL010 (Tables Δ.2 and Δ.3), after extensive and long hour experiments. Furthermore, the commercial humidity sensor data are trustworthy, since they have been previously compared with an external humidity sensor as well, reporting very similar values repeatedly. Thus, the injection of particular amounts of RH ( $\text{N}_2/\text{RH}$ ) in the experimental sequence was mainly based on the regulation of the two different mass flow controllers ( $D_1$ ,  $D_2$ ) **manually** and the real-time RH measurements, as perceived by the commercial Arduino humidity sensor (Tables Δ.4 - Full RH% range and Δ.5 - Low RH% ranges). Through the regulated mass flow controllers, it was possible to transfer the desired RH percentages towards the device under test.

PUL010	Concentration: 39581 ( $\text{mg}/\text{m}^3$ )	Dilution Flow of $\text{N}_2$ : 30.4 ( $\text{ml}/\text{min}$ )
$\text{H}_2\text{O}$	Permeation rates at 82.4 °C	Permeation rates at 71.6 °C
2days P1=	1187890 ( $\text{ng}/\text{min}$ )	642077 ( $\text{ng}/\text{min}$ )
2days P2=	1207216 ( $\text{ng}/\text{min}$ )	657066 ( $\text{ng}/\text{min}$ )
2days P3=	1207930 ( $\text{ng}/\text{min}$ )	657068 ( $\text{ng}/\text{min}$ )
2days P4=	1180556 ( $\text{ng}/\text{min}$ )	657064 ( $\text{ng}/\text{min}$ )
2days P5=	1232687 ( $\text{ng}/\text{min}$ )	661524 ( $\text{ng}/\text{min}$ )
Average	1203256 ( $\text{ng}/\text{min}$ )	654960 ( $\text{ng}/\text{min}$ )

Table Δ.2 Calibration conditions for humidity measurements of the vaporizer PUL010.

PUL110	Concentration: 11419 ( $\text{mg}/\text{m}^3$ )	Dilution Flow of $\text{N}_2$ : 110 ( $\text{ml}/\text{min}$ )
$\text{H}_2\text{O}$	Permeation rates at 82.4 °C	Permeation rates at 102.8 °C
2days P1=	1270718 ( $\text{ng}/\text{min}$ )	9075284 ( $\text{ng}/\text{min}$ )
2days P2=	1242971 ( $\text{ng}/\text{min}$ )	10164995 ( $\text{ng}/\text{min}$ )
2days P3=	1212879 ( $\text{ng}/\text{min}$ )	11946685 ( $\text{ng}/\text{min}$ )
2days P4=	1235544 ( $\text{ng}/\text{min}$ )	10840480 ( $\text{ng}/\text{min}$ )
2days P5=	1256072 ( $\text{ng}/\text{min}$ )	10181430 ( $\text{ng}/\text{min}$ )
Average	1243637 ( $\text{ng}/\text{min}$ )	10441775 ( $\text{ng}/\text{min}$ )

Table Δ.3 Calibration conditions for humidity measurements of the vaporizer PUL110.

Flow rate MFC1-D1	Flow rate MFC2-D2	Concentrations $x(\%) =$ $x(\text{ppm}) / 10000$	Output flow rate mixture	Adjustment to the demanding values D1, D2	
(ccm = ml/min)	(ccm = ml/min)	PPM (N <sub>2</sub> /H <sub>2</sub> O)	(ccm = ml/min)	(ccm = ml/min)	
5 - 100	100 - 2000	H <sub>2</sub> O at 82.4 °C	<b>CONSTANT=100</b>		
			Arduino Relative Humidity	D1	D2
0	100	min	<b>1.44%</b>	<b>0</b>	<b>104</b>
1	99	101	<b>2.38%</b>	<b>1</b>	<b>104</b>
2	98	200	<b>3.17%</b>	<b>2</b>	<b>103</b>
3	97	300	<b>3.96%</b>	<b>3</b>	<b>102</b>
4	96	400	<b>4.82%</b>	<b>4</b>	<b>101</b>
5	95	500	<b>5.69%</b>	<b>5</b>	<b>100</b>
6	94	600	<b>6.40%</b>	<b>6</b>	<b>99</b>
7	93	700	<b>7.12%</b>	<b>7</b>	<b>98</b>
8	92	800	<b>7.69%</b>	<b>8</b>	<b>97</b>
9	91	900	<b>8.40%</b>	<b>9</b>	<b>96</b>
10	90	1000	<b>9.04%</b>	<b>10</b>	<b>95</b>
20	80	2500	<b>15.68%</b>	<b>20</b>	<b>84</b>
30	70	4285	<b>22.27%</b>	<b>30</b>	<b>74</b>
40	60	6665	<b>30.00%</b>	<b>40</b>	<b>64</b>
50	50	10000	<b>37.01%</b>	<b>50</b>	<b>55</b>
60	40	15000	<b>44.33%</b>	<b>60</b>	<b>44</b>
70	30	23330	<b>52.90%</b>	<b>70</b>	<b>34</b>
80	20	40000	<b>63.00%</b>	<b>80</b>	<b>24</b>
90	10	90000	<b>75.15%</b>	<b>90</b>	<b>15</b>
100	0	max	<b>76.90%</b>	<b>100</b>	<b>0</b>

Table Δ.4 Vapor generator conditions (PUL110) and the conversion of ppm (N<sub>2</sub>/H<sub>2</sub>O) towards relative humidity percentages, as recorded by the commercial humidity sensor.

Flow rate MFC1-D1	Flow rate MFC2-D2	Concentrations $x(\%) =$ $x(\text{ppm}) / 10000$	Output flow rate mixture	Adjustment to the demanding values D1, D2	
(ccm = ml/min)	(ccm = ml/min)	PPM (N <sub>2</sub> /H <sub>2</sub> O)	(ccm = ml/min)	(ccm = ml/min)	
5 - 100	100 - 2000	H <sub>2</sub> O at 82.4 °C	<b>CONSTANT=1000</b>		
			Arduino Relative Humidity	D1	D2
0	1000	min	<b>2.01%</b>	<b>0</b>	<b>1004</b>
10	990	100	<b>2.95%</b>	<b>10</b>	<b>992</b>
20	980	200	<b>4.00%</b>	<b>20</b>	<b>982</b>
29	971	300	<b>5.08%</b>	<b>29</b>	<b>972</b>
38	962	400	<b>5.91%</b>	<b>38</b>	<b>963</b>
48	952	500	<b>6.95%</b>	<b>48</b>	<b>955</b>
57	943	600	<b>7.84%</b>	<b>57</b>	<b>946</b>
65	935	700	<b>8.69%</b>	<b>65</b>	<b>938</b>
74	926	800	<b>9.62%</b>	<b>74</b>	<b>928</b>
83	917	900	<b>10.76%</b>	<b>83</b>	<b>919</b>
91	909	1000	<b>12.10%</b>	<b>91</b>	<b>911</b>

100	900	max	13.94%	100	902
-----	-----	-----	--------	-----	-----

Table Δ.5 Vapor generator conditions (Mass Flow Controllers regulated for PUL110) and the conversion of ppm (N<sub>2</sub>/H<sub>2</sub>O) towards very low relative humidity percentages, as perceived by the commercial humidity sensor.

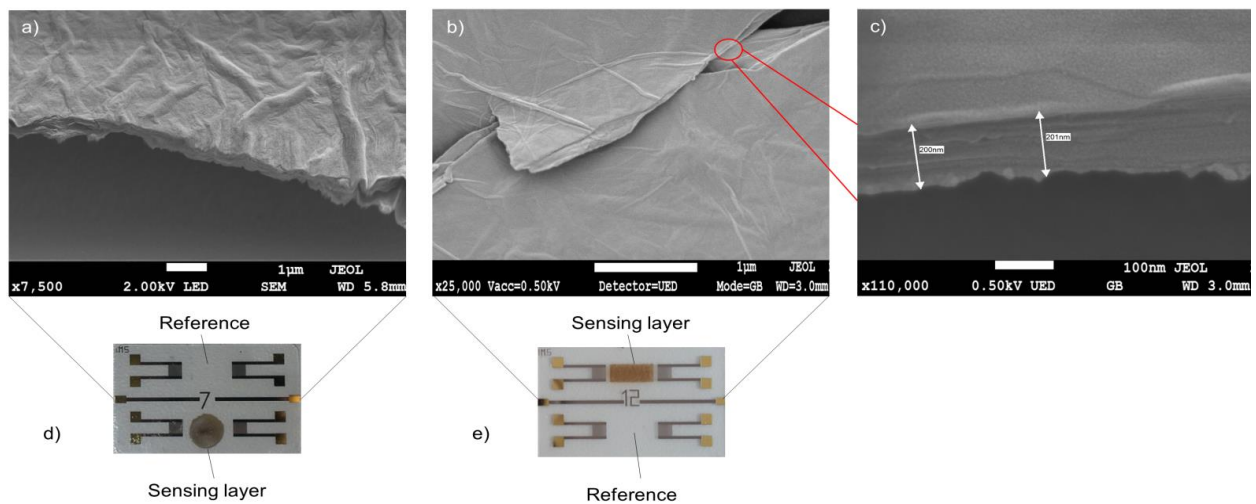
Permeation rate (ng/min)	Molecular weight of C <sub>2</sub> H <sub>6</sub> O	K factor	Flow rate (ml/min)	Cinitial (ppm)	Cmin (ppm)	Cmax (ppm)	Substance	Exposure limits TWA (8 hours)	Exposure limits STEL / Ceiling (short - term)	Notations	CAS No
1446970	46.07	0.5309312	30.4	25271.1022	1.8719335	1579.44389	C <sub>2</sub> H <sub>6</sub> O	-	1000 ppm	-	64-17-5
at T = 61.3 °C											
Permeation rate (ng/min)	Molecular weight of C <sub>7</sub> H <sub>8</sub>	K factor	Flow rate (ml/m)	Cinitial (ppm)	Cmin (ppm)	Cmax (ppm)	C <sub>7</sub> H <sub>8</sub>	20 ppm	-	R	108-88-3
1645867	92.14	0.2654656	30.4	14372.4034	1.06462248	898.275213	Toluene	-	-	-	-
at T = 82.3 °C											
Permeation rate (ng/min)	Molecular weight of H <sub>2</sub> O	K factor	Flow rate (ml/m)	Cinitial (ppm)	Cmin (ppm)	Cmax (ppm)	H <sub>2</sub> O	-	-	-	-
1203256	18.01	1.3581344	30.4	53756.0306	3.98192819	3359.75191	Water	-	-	-	-
at T = 82.4 °C											
Permeation rate (ng/min)	Molecular weight of H <sub>2</sub> S	K factor	Flow rate (ml/m)	Cinitial (ppm)	Cmin (ppm)	Cmax (ppm)	H <sub>2</sub> S	-	Ceiling limit 10 ppm	-	7783-06-4
6800	34.0809	0.7177041	30.4	160.539064	0.01189178	10.0336915	Hydrogen Sulfide	-	-	-	-
at T = 30.0 °C											
Permeation rate (ng/min)	Molecular weight of NO	K factor	Flow rate (ml/m)	Cinitial (ppm)	Cmin (ppm)	Cmax (ppm)	NO	25 ppm	-	-	10102-43-9
14950	30.01	0.8150616	30.4	400.828013	0.02969096	25.0517508	Nitric oxide	-	-	-	-
at T = 30.0 °C											
Permeation rate (ng/min)	Molecular weight of NO <sub>2</sub>	K factor	Flow rate (ml/m)	Cinitial (ppm)	Cmin (ppm)	Cmax (ppm)	NO <sub>2</sub>	-	Ceiling limit 1 ppm	-	10102-44-0
1012	46.0055	0.5316756	30.4	17.6991996	0.00131105	1.10619997	Nitrogen dioxide	-	-	-	-
at T = 30.0 °C											
Permeation rate (ng/min)	Molecular weight of NH <sub>3</sub>	K factor	Flow rate (ml/m)	Cinitial (ppm)	Cmin (ppm)	Cmax (ppm)	NH <sub>3</sub>	25 ppm	35 ppm	-	7664-41-7
8542	17.031	1.4362046	30.4	403.554586	0.02989293	25.2221616	Ammonia	-	-	-	-
at T = 30.0 °C											
Permeation rate (ng/min)	Molecular weight of C <sub>6</sub> H <sub>6</sub>	K factor	Flow rate (ml/m)	Cinitial (ppm)	Cmin (ppm)	Cmax (ppm)	C <sub>6</sub> H <sub>6</sub>	0.5 ppm	2.5 ppm	Skin;A1,1	71-43-2
780	78.11	0.3131481	30.4	8.03472161	0.00059516	0.5021701	Benzene	-	-	-	-
at T = 25.0 °C											
Permeation rate (ng/min)	Molecular weight of CO	K factor	Flow rate (ml/m)	Cinitial (ppm)	Cmin (ppm)	Cmax (ppm)	CO	25 ppm	100 ppm	R	630-08-0
13950	28.01	0.8732596	30.4	400.722721	0.02968316	25.0451701	Carbon monoxide	-	-	-	-
at T = 30.0 °C											
Permeation rate (ng/min)	Molecular weight of SO <sub>2</sub>	K factor	Flow rate (ml/m)	Cinitial (ppm)	Cmin (ppm)	Cmax (ppm)	SO <sub>2</sub>	2 ppm	5 ppm	-	7446-09-5
2611	64.066	0.3817938	30.4	32.791564	0.002429	2.04947275	Sulfur dioxide	-	-	-	-

Table Δ.6 Concentrations (minimum / maximum) for different substances, especially calculated and generated towards NIOSH standards.

## VI.5.2 D.2 Further investigation of the graphene based sensitive material

### VI.5.2.1 D.2.1 Morphological investigation of the graphene oxide based sensitive material

As represented in Figures D-1(a) and D-1(b), two different GO based Love wave (LW) sensors were selected for SEM characterizations, such the Drop-Casted and Inkjet-Printed coated layers (amorphous and ordered), respectively. SEM analysis further confirmed that the Inkjet-Printed GO had clearly a higher organization, as discerned in Figure D-1(c). The LW platform is based on a dual delay line setup, as clearly demonstrated in Figures D-1(d) and D-1(e). Moreover, two different acoustic wave propagation paths were used by corresponding to the coated (GO) and bared (reference) part of the sensor, respectively (differential measurements).

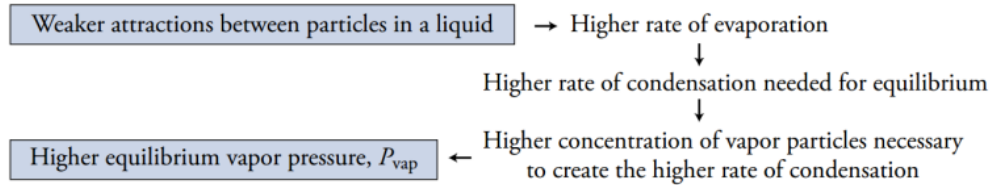


D-1 SEM images of Graphene Oxide coated Love wave devices; tilt-sectional amplification of the (a) Drop - Casted GO, (b) Inkjet - Printed GO and (c) its extended amplification. Top view of the dual delay-lines, each one with a reference and a sensitive channel, functionalized with (d) amorphous GO, (e) ordered GO.

### VI.5.2.2 D.2.2 Reproducibility measurements of graphene oxide based LW devices

In summary, 22 different exposures were realized with 9 hours of each exposure towards high and low concentration environments. A further verification of the GO sample can be observed in the Figure D-2, where the material surface has changed enormously and deterioration of the Drop-Casted GO sensitive layer can be observed. Different exposures to analytes were selected in order to investigate detection capabilities and the solution stability of the Drop-Casted GO sensing layers. Substances such as carbon dioxide, ethanol, acetone, toluene and RH are probably linked with the deterioration of the GO samples. By controlling temperature and humidity variations, no condensation or any other significant differences were observed. For example, the ethanol condensation point starts at 0°C - 10 °C, however there were no signs to indicate the aforementioned conditions in our experimental setup (STP conditions). Ethanol condensation depends also with the flux rates [18], and higher ethanol concentrations lead to a

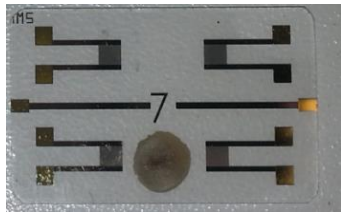
higher equilibrium vapor pressure. The weaker the attractions between particles of a substance, the higher the equilibrium vapor pressure for that substance at a given temperature (Figure D-2) [19]. Comparing to our experiments, low ethanol concentrations were used in GO coated LW devices, thus we can probably safely assume that environmental or experimental conditions do not cause deterioration in the quality of GO. Serious cases of polluting substances that deteriorate GO quality must be further investigated as to root cause.



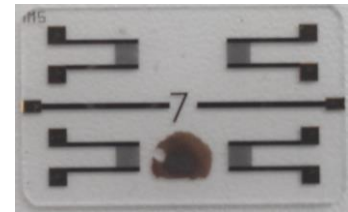
D-2 Link between the weak particle attractions in a liquid and the high equilibrium vapor pressure [20].

Similar concentrations were applied to the Drop-Casted GO devices, especially two months later, as represented in the Figure D-4.

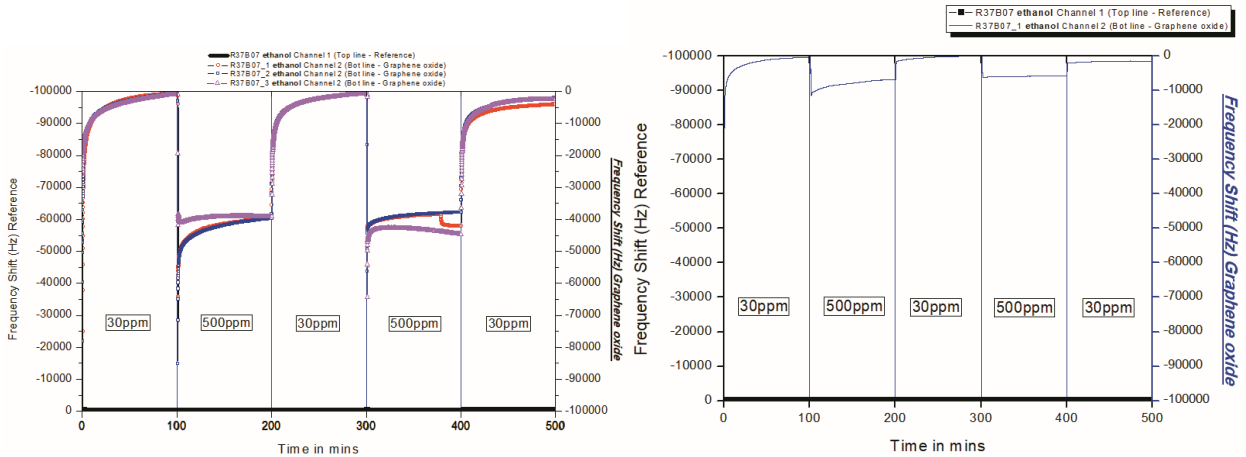
04/04/2014:



11/06/2014:



D-3 Drop-Casted Graphene Oxide deterioration is observed under different dates.



D-4 Drop-Casted Graphene Oxide deterioration is observed under similar ethanol conditions at different dates.

### VI.5.2.3 D.2.3 Drop-Casted GO investigation under CO<sub>2</sub> concentrations

Experimental conditions of the Gas line network at IMS laboratories:

CO<sub>2</sub> (0.03% to 0.1%) / N<sub>2</sub> sequences

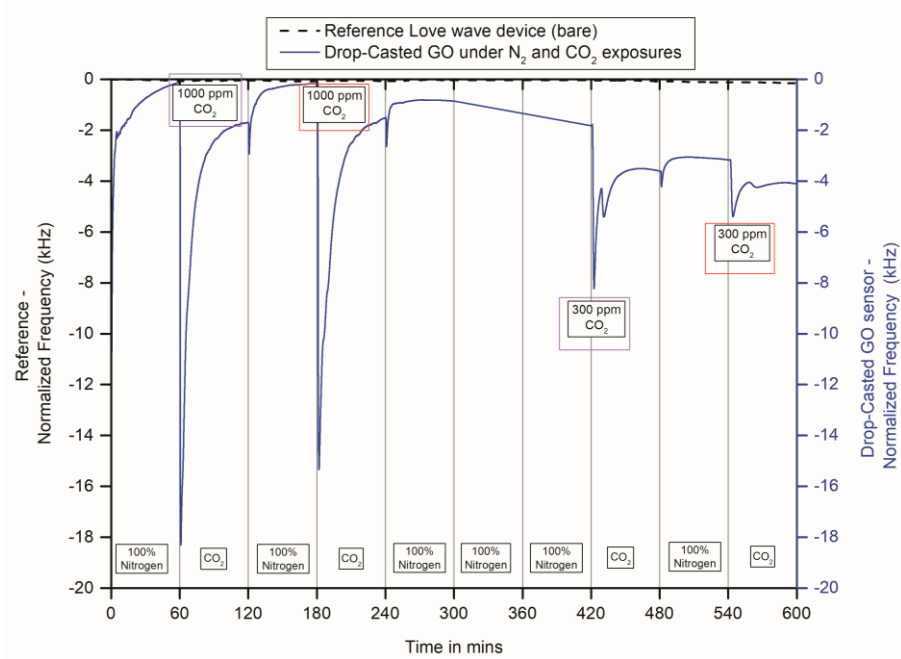
$$\text{Output dilution (ppm)} = C_{\text{initial}} \times D1 / (D1 + D2) \quad (\text{D.4})$$

where D1 and D2 correspond to the CO<sub>2</sub> and N<sub>2</sub> flow rates, respectively. The output flow rate depends on fixed concentrations (i.e., in this case 200ml/min), and therefore it was possible to generate minimum concentrations of CO<sub>2</sub> at 300 ppm or even below. Occupational Safety and Health Administration (OSHA) has established a Permissible Exposure Limit (PEL) for CO<sub>2</sub> of 5,000 ppm (0.5% CO<sub>2</sub> in air) averaged over an 8-hour work day (time-weighted average or TWA). Along similar lines, CO<sub>2</sub> levels in outdoor air typically range from 300 to 400 ppm (0.03% to 0.04%) but can be as high as 600-900 ppm in metropolitan areas. Importantly, low CO<sub>2</sub> concentrations generated, which in this case are less than 350 ppm (average) at normal outdoor levels.

(CO <sub>2</sub> / N <sub>2</sub> ) steps	CO <sub>2</sub> Concentration (ppm)	Flow rate (ml/min)
C1	0 / N <sub>2</sub> (100%)	0
C2	1000 (0.1%)	1880
C3	0 / N <sub>2</sub> (100%)	0
C4	1000	1880
C5	0 / N <sub>2</sub> (100%)	0
C6	0 / N <sub>2</sub> (100%)	0
C7	0 / N <sub>2</sub> (100%)	0
C8	300 (0.03%)	564
C9	0	564
C10	300 (0.03%)	564

Table Δ.7 Representative configuration of different CO<sub>2</sub> concentrations for Drop-Casted GO LW devices.





D-5 Drop-Casted GO responses under different CO<sub>2</sub> concentrations.

## References or Bibliography (if any)

- [1] K. Länge, B. E. Rapp, and M. Rapp, "Surface acoustic wave biosensors: a review," *Anal. Bioanal. Chem.*, vol. 391, no. 5, pp. 1509–1519, Jul. 2008.
- [2] T.-Y. Lin, C.-H. Hu, and T.-C. Chou, "Determination of albumin concentration by MIP-QCM sensor," *Biosens. Bioelectron.*, vol. 20, no. 1, pp. 75–81, Jul. 2004.
- [3] R. Gabl *et al.*, "Novel integrated FBAR sensors: a universal technology platform for bio- and gas-detection," in *2003 IEEE SENSORS*, 2003, vol. 2, pp. 1184–1188 Vol.2.
- [4] G. Sehra, M. Cole, and J. W. Gardner, "Miniature taste sensing system based on dual SH-SAW sensor device: an electronic tongue," *Sens. Actuators B Chem.*, vol. 103, no. 1, pp. 233–239, Sep. 2004.
- [5] R. L. Baer, C. A. Flory, M. Tom-Moy, and D. Solomon, "STW chemical sensors," in *IEEE 1992 Ultrasonics Symposium Proceedings*, 1992, pp. 293–298 vol.1.
- [6] G. Kovacs, M. J. Vellekoop, R. Haueis, G. W. Lubking, and A. Venema, "A love wave sensor for (bio)chemical sensing in liquids," *Sens. Actuators Phys.*, vol. 43, no. 1, pp. 38–43, May 1994.
- [7] S. J. Martin, A. J. Ricco, T. M. Niemczyk, and G. C. Frye, "Characterization of SH acoustic plate mode liquid sensors," *Sens. Actuators*, vol. 20, no. 3, pp. 253–268, Dec. 1989.
- [8] W. Chang, P. Sung, C. Chu, C. Shih, and Y. Lin, "Phase Detection of the Two-Port FPW Sensor for Biosensing," *IEEE Sens. J.*, vol. 8, no. 5, pp. 501–507, May 2008.
- [9] "Surface acoustic wave devices as chemical sensors in liquids. Evidence disputing the importance of Rayleigh wave propagation | Analytical Chemistry." [Online]. Available: <https://pubs.acs.org/doi/pdf/10.1021/ac00133a010>. [Accessed: 13-Jun-2019].
- [10] C. Zhang, J. J. Caron, and J. F. Vetelino, "The Bleustein–Gulyaev wave for liquid sensing applications," *Sens. Actuators B Chem.*, vol. 76, no. 1, pp. 64–68, Jun. 2001.
- [11] A. E. H. Love, *A Treatise on the Mathematical Theory of Elasticity*. Cambridge University Press, 2013.
- [12] X. Liu, S. Cheng, H. Liu, S. Hu, D. Zhang, and H. Ning, "A Survey on Gas Sensing Technology," *Sensors*, vol. 12, no. 7, pp. 9635–9665, Jul. 2012.
- [13] G. Eranna, B. C. Joshi, D. P. Runthala, and R. P. Gupta, "Oxide Materials for Development of Integrated Gas Sensors—A Comprehensive Review," *Crit. Rev. Solid State Mater. Sci.*, vol. 29, no. 3–4, pp. 111–188, Jul. 2004.
- [14] B. Drafts, "Acoustic wave technology sensors," *IEEE Trans. Microw. Theory Tech.*, vol. 49, no. 4, pp. 795–802, Apr. 2001.
- [15] C. Multiphysics, *Structural Mechanics Module*. Reference Guide, Vers, 2008.
- [16] S. W. Park and R. A. Schapery, "Methods of interconversion between linear viscoelastic material functions. Part I—a numerical method based on Prony series," *Int. J. Solids Struct.*, vol. 36, no. 11, pp. 1653–1675, Apr. 1999.
- [17] "Industry Support Siemens."
- [18] Y. Li, J. Yan, L. Qiao, and S. Hu, "Experimental study on the condensation of ethanol–water mixtures on vertical tube," *Heat Mass Transf.*, vol. 44, no. 5, pp. 607–616, Mar. 2008.
- [19] S. S. Zumdahl and S. A. Zumdahl, *Chemistry: An Atoms First Approach*. Cengage Learning, 2011.
- [20] M. Bishop, *An Introduction to Chemistry: Second Edition*. Chiral Publishing Company, 2009.